Member of the Helmholtz Association

High-rate growth of hydrogenated amorphous and microcrystalline silicon for thin-film silicon solar cells using dynamic very-high frequency plasma-enhanced chemical vapor deposition

Thomas Zimmermann

JÜLICH
FORSCHUNGSZENTRUM

Technische Universität Dresden

High-rate growth of hydrogenated amorphous and microcrystalline silicon for thin-film silicon solar cells using dynamic very-high frequency plasma-enhanced chemical vapor deposition

Thomas Zimmermann

von der Fakultät Elektrotechnik und Informationstechnik
der Technischen Universität Dresden
zur Erlangung des akademischen Grades eines

Doktoringenieurs
(Dr.-Ing.)

genehmigte Dissertation

Vorsitzender:	Prof. Dr.-Ing. habil. Gerald Gerlach
Gutachter:	Prof. Dr. rer. nat. Johann Wolfgang Bartha Prof. Dr. rer. nat. Uwe Rau

Tag der Einreichung:	27.04.2012
Tag der Verteidigung:	29.01.2013

Forschungszentrum Jülich GmbH
Institute of Energy- and Climate Research (IEK)
Photovoltaics (IEK-5)

High-rate growth of hydrogenated amorphous and microcrystalline silicon for thin-film silicon solar cells using dynamic very-high frequency plasma-enhanced chemical vapor deposition

Thomas Zimmermann

Schriften des Forschungszentrums Jülich
Reihe Energie & Umwelt / Energy & Environment Band / Volume 183

ISSN 1866-1793 ISBN 978-3-89336-892-1

Bibliographic information published by the Deutsche Nationalbibliothek.
The Deutsche Nationalbibliothek lists this publication in the Deutsche Nationalbibliografie; detailed bibliographic data are available in the Internet at http://dnb.d-nb.de.

Publisher and Distributor: Forschungszentrum Jülich GmbH
Zentralbibliothek
52425 Jülich
Tel: +49 2461 61-5368
Fax: +49 2461 61-6103
Email: zb-publikation@fz-juelich.de
www.fz-juelich.de/zb

Cover Design: Grafische Medien, Forschungszentrum Jülich GmbH

Printer: Grafische Medien, Forschungszentrum Jülich GmbH

Schriften des Forschungszentrums Jülich
Reihe Energie & Umwelt / Energy & Environment, Band / Volume 183

D 14 (Diss., Dresden, Univ., 2013)

ISSN 1866-1793
ISBN 978-3-89336-892-1

Abstract

Thin-film silicon tandem solar cells based on a hydrogenated amorphous silicon (a-Si:H) top-cell and a hydrogenated microcrystalline silicon (μc-Si:H) bottom-cell are a promising photovoltaic technology as they use a combination of absorber materials that is ideally suited for the solar spectrum. Additionally, the involved materials are abundant and non-toxic which is important for the manufacturing and application on a large scale.

One of the most important factors for the application of photovoltaic technologies is the cost per watt. There are several ways to reduce this figure: increasing the efficiency of the solar cells, reducing the material consumption and increasing the throughput of the manufacturing equipment.

The use of very-high frequencies has been proven to be beneficial for the material quality at high deposition rates thus enabling a high throughput and high solar cell efficiencies. In the present work a scalable very-high frequency plasma-enhanced chemical vapor deposition (VHF-PECVD) technique for state-of-the-art solar cells is developed. Linear plasma sources are applied which facilitate the use of very-high frequencies on large areas without compromising on the homogeneity of the deposition process.

The linear plasma sources require a dynamic deposition process with the substrate passing by the electrodes in order to achieve a homogeneous deposition on large areas. State-of-the-art static radio-frequency (RF) PECVD processes are used as a reference in order to assess the potential of a dynamic VHF-PECVD technique for the growth of high-quality a-Si:H and μc-Si:H absorber layers at high rates.

In chapter 4 the influence of the deposition process of the μc-Si:H i-layer on the solar cell performance is studied for static deposition processes. It is shown that the correlation between the i-layer growth rate, its crystallinity and the solar cell performance is similar for VHF- and RF-PECVD processes despite the different electrode configurations, excitation frequencies and process regimes. It is found that solar cells incorporating i-layers grown statically using VHF-PECVD processes obtain a state-of-the-art efficiency close to 8 % for growth rates up to 1.4 nm/s compared to 0.53 nm/s for RF-PECVD processes.

The influence of dynamic deposition processes on the performance of μc-Si:H solar cells is studied. It is found that μc-Si:H solar cells incorporating dynamically grown i-layers obtain an efficiency of 7.3 % at a deposition rate of 0.95 nm/s. There is a small negative influence of the dynamic deposition process on the solar cell efficiency compared to static deposition processes which is related to the changing growth conditions the substrate encounters during a dynamic i-layer deposition process.

The changes in gas composition during a dynamic i-layer deposition process using the linear plasma sources are studied systematically using a static RF-PECVD regime and applying a time-dependent gas composition. The results show that the changes in the gas composition affect the solar cell performance if they exceed a critical level.

In chapter 5 dynamic VHF-PECVD processes for a-Si:H are developed in order to investigate the influence of the i-layer growth rate, process parameters and deposition technique on the solar performance and light-induced degradation. The results in this work indicate that a-Si:H solar cells incorporating i-layers grown dynamically by VHF-PECVD using linear plasma sources perform as good and better as solar cells with i-layers grown statically by RF-PECVD at the same deposition rate. State-of-the-art stabilized a-Si:H solar cell efficiencies of 7.6 % are obtained at a growth rate of 0.35 nm/s using dynamic VHF-PECVD processes.

It is found that the stabilized efficiency of the a-Si:H solar cells strongly decreases with the i-layer deposition rate. A simplified model is presented that is used to obtain an estimate for the deposition rate dependent efficiency of an a-Si:H/μc-Si:H tandem solar cell based on the photovoltaic parameters of the single-junction solar cells. The aim is to investigate the individual influences of the a-Si:H and μc-Si:H absorber layer deposition rates on the performance of the tandem solar cell.

The results show that a high deposition rate of the μc-Si:H absorber layer has a much higher potential for reducing the total deposition time of the absorber layers compared to high deposition rates for the a-Si:H absorber layer. Additionally, it is found that high deposition rates for a-Si:H have a strong negative impact on the tandem solar cell performance while the tandem solar cell efficiency remains almost constant for higher μc-Si:H deposition rates.

It is concluded that the deposition rate of the μc-Si:H absorber layer is key to reduce the total deposition time without compromising on the tandem solar cell performance. The developed VHF-PECVD technique using linear plasma sources is capable of meeting this criterion while promoting a path to scale the processes to large substrate areas.

Contents

List of abbreviations and symbols

Abbreviations

CdTe	cadmium telluride
CIGS	copper indium gallium diselenide
a-Si:H	hydrogenated amorphous silicon
μc-Si:H	hydrogenated microcrystalline silicon
PECVD	plasma-enhanced chemical vapor deposition
RF	radio-frequency
VHF	very-high frequency
HWCVD	hot-wire chemical vapor deposition
p–i–n	p-doped – intrinsic – n-doped
TCO	transparent conductive oxide
ZnO:Al	aluminum doped zinc oxide
$SnO:F_2$	fluorine doped tin oxide
MFC	mass flow controller
H_2	hydrogen
SiH_4	silane
TMB	trimethylboron
PH_3	phosphine
CO_2	carbon dioxide
CH_3	methane
PC1	process chamber 1
PC2	process chamber 2
PDS	photothermal deflection spectroscopy
DSR	differential spectral response
AM1.5	air mass 1.5 (refers to the standard solar spectrum)
MPP	maximum power point

Symbols

P	power
$\overline{P}$	power density
p	pressure
d_{el}	electrode distance

SC	silane concentration
SC_{in}	silane concentration at gas feed
SC_{out}	silane concentration at exhaust
q_{total}	total gas flow
t_{res}	residence time of gas molecules
η_{gas}	gas utilization
f	excitation frequency
T_{s}	substrate temperature
r	deposition rate
$\overline{r}$	average deposition rate
r_{d}	dynamic deposition rate
v	carrier velocity
d_{i}	i-layer thickness
σ_{ph}	photo-conductivity
σ_{d}	dark-conductivity
$\alpha_{1.2\ \mathrm{eV}}$	absorption coefficient at a photon energy of 1.2 eV
E_{04}	energy at which the absorption coefficient is 10^4 cm^{-1}
$I_{\mathrm{c}}^{\mathrm{RS}}$	Raman crystallinity
c_{H}	atomic hydrogen concentration
R	microstructure factor
$E_{\mathrm{AM1.5}}$	integrated spectral irradiance of AM1.5 spectrum
λ	wavelength
η	solar cell efficiency
FF	fill factor
V_{OC}	open-circuit voltage
J_{SC}	short-circuit current density
EQE	external quantum efficiency
A_{rel}	relative amplitude
T	period
d_{T}	thickness per period

1 Introduction

The first crystalline silicon solar cell was presented in 1954 [1]. As the semiconductor industry evolved so did the understanding and processing of silicon. Since then mono- and polycrystalline silicon solar cells (often referred to as first generation photovoltaics) dominated the photovoltaic market. Though the efficiency of the crystalline silicon solar cells was continuously improved, the high material and manufacturing costs remain a concern as they represent the largest cost factor of crystalline silicon solar modules [2, 3].

Early on researchers started to look for new concepts that would offer significant cost reductions. With amorphous silicon [4], cadmium telluride (CdTe) [5] and copper indium/gallium diselenide (CIGS) [6] three other semiconductors were investigated as possible candidates for the second generation of photovoltaic devices. The idea was to reduce the solar cell thickness from more than 200 μm to only a few micrometers in order to cut the material cost to a minimum. At the same time the use of simple deposition processes on large areas was envisaged to keep the manufacturing costs low. Because of the low thickness of these solar cells they are typically referred to as thin-film solar cells.

In 1976 D. E. Carlson and C. R. Wronski were the first to produce a hydrogenated amorphous silicon (a-Si:H) solar cell [4]. A year later it was shown that the material itself degrades during light exposure [7] leading to a declining solar cell efficiency (so-called Staebler-Wronski effect). As a consequence a lot of research related to a-Si:H has been focusing on understanding and minimizing the degradation loss.

In the mid 1990s research groups started to intensify their efforts on hydrogenated microcrystalline silicon (μc-Si:H) [8, 9]. Contrary to hydrogenated amorphous silicon μc-Si:H is not prone to degradation, which makes it very interesting for an application in solar cells. But there are more advantages for using hydrogenated microcrystalline silicon.

First, the material can be grown with the same equipment as a-Si:H by adjusting the process parameters. Second, the combination of a-Si:H and μc-Si:H in a tandem solar cell enables higher efficiencies compared to single-junction a-Si:H or μc-Si:H solar cells.

Third, because of the particular band gaps of a-Si:H and μc-Si:H the tandem solar cell is ideally suited for the solar spectrum [10].

The most common technique to deposit a-Si:H and μc-Si:H is plasma-enhanced chemical vapor deposition (PECVD). It has been found that the use of very-high frequencies (VHF) is beneficial for the deposition of high quality μc-Si:H material at high deposition rates compared to radio frequency PECVD (RF-PECVD). Figure 1.1 displays the best efficiencies η of μc-Si:H p–i–n solar cells obtained for both deposition techniques.

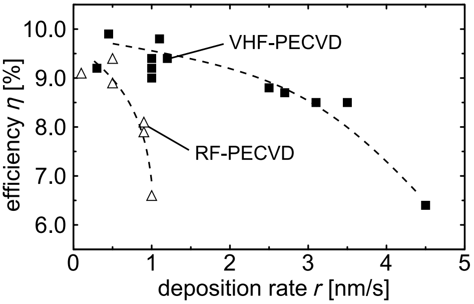

Figure 1.1: Best lab efficiencies η for μc-Si:H p–i–n solar cells as a function of the deposition rate r, lines are guides to the eye. The results are sorted by RF-PECVD [11–15] and VHF-PECVD [16–21].

Higher excitation frequencies of the RF signal that induces the plasma allow high-quality material to be deposited at high deposition rates, but there is a limitation. As the frequency increases the corresponding wavelength of the VHF signal decreases. Depending on the frequency and the size of the electrode, standing waves may occur leading to a non-uniform voltage distribution across the electrode. This inhomogeneity causes a non-uniform plasma density and eventually results in a non-uniform deposition.

Different solutions have been suggested for the inhomogeneity problem related to the use of very-high frequencies on large areas. One design applies a Gaussian-lens shape to the electrode to compensate the inhomogeneous voltage distribution [22].

Two other designs use electrodes that are not planar, but made up of an array of pipes [16, 23]. For these electrodes a good homogeneity is achieved by feeding the power to several points on the electrode. Additionally, for some of the power feeding points the phase of the VHF signal is shifted or a second frequency is applied in order to minimize the standing wave effect (for more details see section 3.1.1).

The deposition system used in this study pursues an alternative approach. Linear plasma sources in combination with a dynamic deposition process are applied, in order to achieve a homogeneous deposition in both substrate dimensions. The linear plasma sources are narrow electrodes which are scaled up in only one dimension. The number of power feeds is adapted to the length of the electrode and the excitation frequency [24]. This concept is believed to be better suited for very-high frequencies than conventional large-area systems. Additionally, the dynamic deposition enables a continuous deposition process and may allow the use of flexible substrates, which are less expensive than glass.

The electrode configuration promotes a homogeneous voltage distribution along the length of the electrode, giving a homogeneous deposition profile perpendicular to the movement direction of the substrate. The substrate itself moves in front of and parallel to the electrodes at a constant speed and stable plasma conditions. This procedure is referred to as dynamic deposition process.

Every point on the substrate passes through the same deposition conditions leading to a homogeneous deposition in both substrate dimensions. The growth conditions for a fixed point on the substrate change during the deposition process, depending on the current position of the substrate. The material properties may change in growth direction but the homogeneity over the substrate area is not affected.

The aim of this work is to assess the potential of the dynamic VHF-PECVD concept for the deposition of high-quality intrinsic a-Si:H and μc-Si:H. The focus is on the homogeneity of the deposition process and the quality of corresponding thin-film solar cells at elevated growth rates.

In chapter 2 the experimental background, models for the layer growth and basic material properties are outlined. Material and solar cell characterization techniques are presented which have been used to assess the material quality. Chapter 3 focuses in detail on large-area VHF-PECVD systems and the concept of the dynamic deposition process. The prerequisites of the dynamic deposition process and the implications on the design of the deposition system are discussed.

For μc-Si:H static and dynamic deposition processes are reviewed in order to assess the influence of changing growth conditions on the quality of μc-Si:H solar cells (chapter 4). In chapter 5 the influence of the deposition rate and the dynamic deposition process on the quality of intrinsic a-Si:H is investigated. Because of the Stabler-Wronski effect the focus is on the solar cell performance before and after degradation. For both materials a comparison to a state-of-the-art RF-PECVD regime is given.

2 Fundamentals

This chapter describes the basics of thin-film silicon solar cells. First the a-Si:H/μc-Si:H tandem solar cell structure is presented, followed by a description of the deposition process, used to produce thin-film silicon. The growth models are reviewed in order to gain insight into the phenomenon of depositing two different phases of material with one deposition process. Subsequently the basic material properties of hydrogenated amorphous silicon (a-Si:H) and hydrogenated microcrystalline silicon (μc-Si:H) are described. Finally the characterization techniques for single layers and solar cells are presented.

2.1 Thin-film silicon tandem solar cell

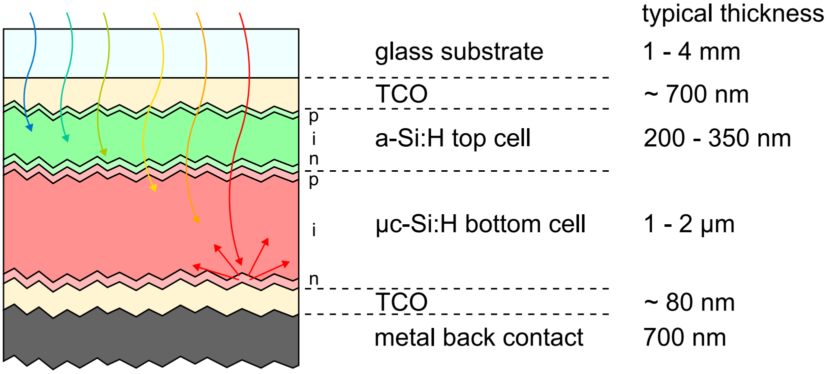

Figure 2.1: Schematic cross section of a tandem solar cell based on a-Si:H and μc-Si:H absorber layers (layer thicknesses are not to scale). The structure consists of a glass coated with a transparent conductive oxide (TCO) as front contact, the a-Si:H and μc-Si:H p–i–n top and bottom cell, a TCO as back reflector and a metal as back contact.

Figure 2.1 depicts a schematic cross section of a tandem solar cell based on an a-Si:H top cell and a μc-Si:H bottom cell. The tandem solar cell is typically deposited on a glass substrate that is coated with a textured transparent conductive oxide (TCO) as front contact. The light enters the structure through the substrate and is absorbed in the solar cell. The textured front contact TCO and the TCO at the back of the solar cell scatter the light in different angles. As a result the optical path length within the absorber layers is increased leading to a higher absorption of photons (so-called light trapping effect).

The top and the bottom solar cell consist of a p-doped layer, an intrinsic layer (i-layer) and a n-doped layer. The deposition sequence for the three silicon films starts with the p-layer. Hence, this structure is referred to as p–i–n or superstrate configuration.

The two doped layers serve as selective contacts for the photo-generated charge carriers. Additionally, the two layers build up an electric field that enhances the collection of photo-generated charge carriers.

The holes that are created pass through the p-layer while the electrons pass through the n-layer. At the n–p interface between the two solar cells the electrons of the top cell and the holes of the bottom cell recombine. The corresponding holes of the top cell and electrons of the bottom cell pass through the front and back contact, respectively. These charge carriers can be used to drive a current through an external load. However, as the two cells are connected in series, the cell with the lower current will limit the current of the tandem cell. Therefore the currents of top and bottom cell need to be matched.

Because of the different band gaps of 1.6–1.9 eV for a-Si:H and 1.1 eV for μc-Si:H the two materials absorb different parts of the solar spectrum (see section 2.5.6). If a photon has a lower energy than the band gap, it transmits and does not contribute to the generation of charge carriers. If the energy is larger than the band gap the photon is absorbed. The excess energy of the photon (photon energy minus band gap) is lost to thermalization.

The transmission of low-energy photons and the thermalization of excess energy are the two basic loss mechanisms limiting the solar cell efficiency. By combining materials with different band gaps the maximum efficiency can be improved due to the reduction of these losses.

2.2 Preparation of a-Si:H and μc-Si:H

2.2.1 Plasma Enhanced Chemical Vapor Deposition

In the late 1960s the first a-Si:H and μc-Si:H layers have been deposited successfully by Chittick et al. [25] and Veprek et al. [26], respectively. The most common technique to grow device quality a-Si:H and μc-Si:H is chemical vapor deposition (CVD) with a mixture of hydrogen (H_2) and silane (SiH_4) as precursor gases. In order to adhere to a surface and contribute to the material growth the SiH_4 molecule has to be dissociated. The required energy for the dissociation process can be provided thermally (hot-wire CVD – HWCVD) or by high-energy electrons in a plasma (plasma-enhanced CVD – PECVD).

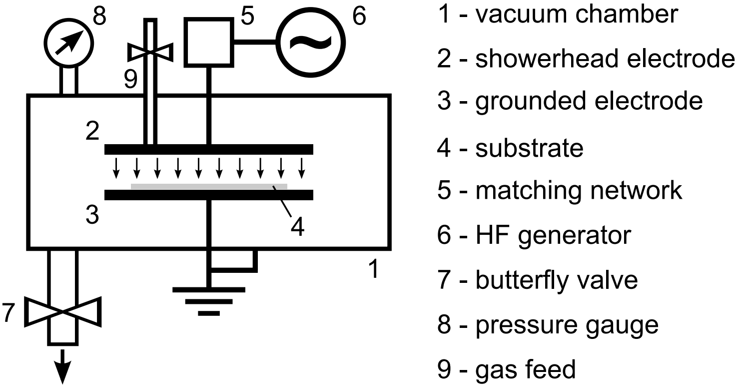

Figure 2.2: Schematic of a typical PECVD deposition chamber.

Figure 2.2 shows the schematic of a state-of-the-art PECVD reactor. The deposition process is carried out in a vacuum chamber which is equipped with two parallel electrodes. The gas mixture is supplied through mass flow controllers (MFCs) to the showerhead electrode while the substrate rests on the grounded counter-electrode (which may also serve as heater). The plasma is ignited between these two electrodes applying a radio frequency (RF) or very-high frequency (VHF) signal. The pressure during the deposition process is monitored by a pressure gauge and adjusted using a butterfly valve. The molecules that do not contribute to the material growth are pumped using rotary or roots pumps.

2.2.2 Process parameters

In this section the deposition parameters and their influence on the deposition process are discussed.

Power P The electron and ion density rises with an increasing power level of the applied RF/VHF signal. The higher power level leads to an increase in the deposition rate until all SiH_4 molecules are dissociated and contribute to the material growth. Additionally, the higher electron energy enables other dissociation reactions, which may change the plasma composition. At the same time the plasma potential increases leading to a stronger ion bombardment of the electrode and substrate.

Pressure p The mean free path of the molecules in the plasma becomes smaller with a rising deposition pressure. The shorter mean free path reduces the energy that ions can obtain, lowering the energy of the ion bombardment. For this reason pressure and power are typically increased at the same time in order to keep the ion bombardment at a moderate level.

Electrode gap d_{el} The electrode gap and electrode area define the volume of the plasma. Hence, at a given power level the power density increases for a smaller electrode gap. According to "Paschen's Law" there is a minimum in power for the product of electrode gap and pressure to ignite and maintain a plasma. Hence, for a high pressure regime a narrow electrode gap is typically chosen.

Silane concentration SC The silane concentration is defined as the ratio of the silane flow $q_{\mathrm{SiH_4}}$ to the total gas flow $q_{\mathrm{total}} = q_{\mathrm{SiH_4}} + q_{\mathrm{H_2}}$.

$$SC = \frac{q_{\mathrm{SiH_4}}}{q_{\mathrm{total}}} \tag{2.1}$$

Typically μc-Si:H is deposited at low silane concentrations while a-Si:H is deposited at high silane concentrations. However, van den Donker et al. [27] as well as Strahm et al. [28] have proven that it is possible to deposit μc-Si:H from a pure silane flow by carefully adjusting the process parameters.

Total gas flow q_{total} and residence time t_{res} The residence time of a gas molecule within the plasma increases for decreasing total gas flows, if the pressure is kept constant. From a manufacturing perspective low total gas flows and high residence times are preferred as they result in a higher gas utilization.

Gas utilization η_{gas} The gas utilization is defined as the ratio of deposited silicon to the amount of silicon supplied as SiH_4. In order to assess this quantity the silane flow

$q_{\mathrm{SiH_4}}$ and deposition rate r have to be known [29]. The gas utilization can be calculated as

$$\eta_{gas} = \frac{rA\rho_{\mathrm{Si}}kT_0}{q_{\mathrm{SiH_4}}p_0m_{\mathrm{Si}}}, \tag{2.2}$$

with A being the deposition area, ρ_{Si} the density of crystalline silicon, k the Boltzmann constant, T_0 the standard temperature, p_0 the standard pressure and m_{Si} the atomic mass silicon.

Excitation frequency f The excitation frequency of the signal has a direct impact on the energy distribution of the electrons in the plasma. The mean energy of the electrons decreases with increasing excitation frequency. Additionally, the sheath thickness is reduced which results in the power to be coupled-in more efficiently [30]. Hence, the electron density rises which results in a higher dissociation rate leading to higher radical and ion densities. The energy of the ions is reduced because of a lower plasma potential at a given power level. Hence, pressure and excitation frequency have a similar effect on the energy of the ion bombardment.

Substrate temperature T_{s} The substrate temperature has a strong influence on the material growth. If the temperature is too low the $\mathrm{SiH_3}$ radicals are not very mobile on the surface, they may not be able to find a preferential site for material growth. Instead, they stick to the surface at, or close to, the first point of contact. On the other hand, if the temperature is too high the surface of the growing layer may not be terminated by hydrogen reducing the mobility of the $\mathrm{SiH_3}$ radicals as well. Both effects typically result in a poor material quality because of a higher defect density [31].

2.2.3 Large-area deposition system (LADA)

Figure 2.3 shows the top view of the vertical in-line PECVD system (called LADA) used in this work. The deposition tool consists of a load lock, two process chambers and an empty chamber, all of which are connected in series and separated by gate valves. The base pressure of the deposition system is typically below 5×10^{-7} mbar, the leak rate is lower than 5×10^{-5} mbar l/min.

The substrates are mounted on a carrier in order to be transported within the deposition system. The carrier can hold one 40×40 cm^2 substrate or up to nine 10×10 cm^2 substrates. In both process chambers the substrate temperature is actively adjusted by monitoring the glass temperature from the backside using a pyrometer and adapting the heater temperature accordingly. The deposition pressure is measured in the exhaust gas pipe before the butterfly valve (not shown in fig. 2.3).

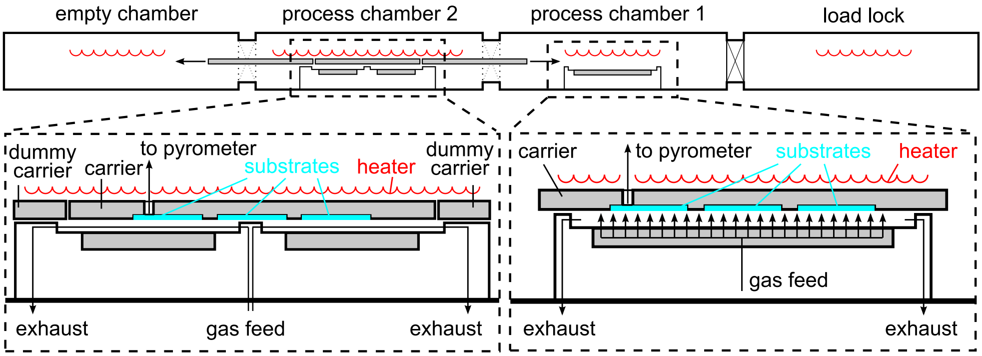

Figure 2.3: Schematic of the in-line PECVD system (LADA) for the deposition on up to 40x40 cm^2 glass substrates (top view).

Process chamber 1 – static RF-PECVD

Process chamber 1 (PC1) is equipped with a 40 × 40 cm^2 planar showerhead electrode (PSE) operating at a frequency of 13.56 MHz. All depositions in PC1 are carried out statically with the carrier being pushed against the grounded electrode shielding in order to connect the carrier to signal ground. Thus, the carrier serves as counter-electrode.

The showerhead electrode promotes a homogeneous gas distribution which is a requirement for a uniform static deposition process. Most industrial PECVD systems use this configuration to feed the gas into the chamber. Hence, the process chamber 1 is considered to be a state-of-the-art deposition chamber and serves as a reference for the deposition processes in process chamber 2.

Process chamber 2 – dynamic VHF-PECVD

To evaluate the dynamic deposition process for intrinsic a-Si:H and μc-Si:H the LADA system is equipped with two 40 × 20 cm^2 linear plasma sources in process chamber 2 (PC2). An excitation frequency of 60 MHz is chosen in order to investigate the differences between static RF-PECVD and dynamic VHF-PECVD processes. Contrary to the planar showerhead electrode in PC1 a cross-flow design is used in PC2. The gas enters the chamber between the two electrodes and is pumped at the outer edges of the electrodes (see figure 2.3). For more details on the dynamic deposition process, the prerequisites and its experimental implementation see chapter 3.

2.3 Growth of a-Si:H and μc-Si:H

In a-Si:H and μc-Si:H material most silicon atoms are bonded to four other silicon atoms. Nevertheless, the structure of a-Si:H and μc-Si:H differs significantly.

Microcrystalline silicon consists of a large number of small grains with different orientations (see figure 2.4a). The structure within a grain is the same as for monocrystalline silicon. The bond angles and bond lengths between the silicon atoms are fixed, leading to a tetragonal configuration.

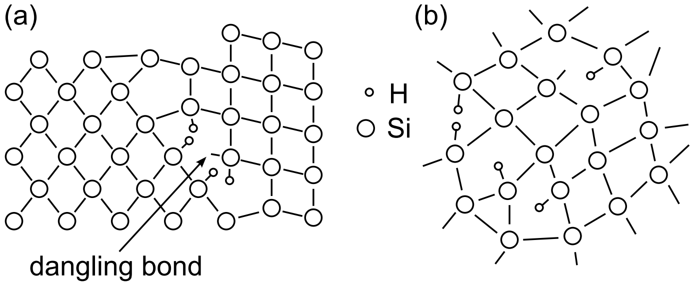

Figure 2.4: 2D-representation of a) μc-Si:H and b) a-Si:H material.

A growing μc-Si:H layer usually starts with an amorphous incubation zone. Once first crystallites occur the transition towards local epitaxial growth begins. The size of these crystallites increases with film thickness. Once the different crystals touch each other, the material starts to grow columnar.

Due to the small size of the grains (typically in the order of a few tens of nanometers), there are a many grain boundaries within a μc-Si:H layer. The lattice is disturbed at these boundaries – not all silicon atoms bond with four other silicon atoms. Some silicon atoms are left with one or more open bonds (dangling bonds). These open bonds may be passivated by hydrogen atoms as indicated in figure 2.4a.

Figure 2.4b shows the structural composition of an a-Si:H layer. Again, the majority of the silicon atoms are bonded to four other silicon atoms. Most of the dangling bonds in a-Si:H are terminated by hydrogen. Figure 2.4b also shows that there is no periodic lattice in a-Si:H – the bond lengths and bond angles vary between the silicon atoms. As a consequence the material properties of a-Si:H and μc-Si:H differ significantly (see section 2.4).

In order to understand the growth of the two different types of materials, it is important to understand the details of the deposition process. For both materials the PECVD technique is commonly used with H_2 and SiH_4 as precursor gases (see section 2.2.1). Within the plasma the silane molecules dissociate to atomic hydrogen, SiH_x (with x between 0 and 3) and the corresponding excited states. From all precursors the SiH_3 radical is believed to be the main precursor for layer growth [31].

The hydrogen atoms created through dissociation of H_2 and SiH_4 terminate the open bonds of the silicon surface. When a SiH_3 radical arrives at the surface it may remove a hydrogen atom, forming SiH_4 and leaving an open bond at the surface. A following SiH_3 can then form a Si–Si bond at this position and contribute to the layer growth.

The next sections are a short summary of the growth models for microcrystalline silicon, based on publications of A. Matsuda [31, 32].

2.3.1 Surface diffusion model

The surface diffusion model focuses on the mobility of the growth precursors at the surface of the growing layer.

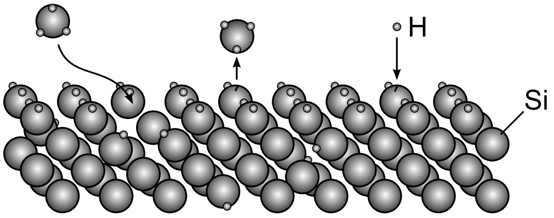

Figure 2.5: Surface diffusion model for the growth of μc-Si:H material based on ref. [31]. Hydrogen terminates the open bonds at the surface, but it can be subtracted by a SiH_3 radical. If a SiH_3 radical finds an open bond it may form an Si–Si bond and contribute to the layer growth.

There are basically two ways to increase the mobility of the SiH_3 radical. First, the dangling bonds at the surface of the growing layer should be terminated by hydrogen (see figure 2.5). This state can be reached by applying a low silane concentration, resulting in a high flux of atomic hydrogen to the surface. Second, a higher temperature may be used to increase the mobility of the growth precursor itself.

Both measures lead to an enhanced surface diffusion. As a result the SiH_3 radical has more time to find an energetically preferred site for layer growth. Ultimately, these conditions promote crystalline growth.

2.3.2 Etching model

The etching model focuses on the increasing hydrogen fraction at low silane concentrations. The atomic hydrogen can break weak Si–Si bonds that are typically found in amorphous silicon. This process results in a dangling bond at the surface. A subsequent SiH_3 radical may bond in an energetically preferred state. The new Si–Si bond could be more stable, resulting in a material that is more resistive against hydrogen etching [33].

Dingemans et al. investigated the process of hydrogen etching for silicon films with different degrees of crystallinity [33]. The optical emission spectra of hydrogen plasmas were investigated for a variety of silicon films. They found a correlation between the etch rate and the crystallinity of the material. The etch rate decreased with increasing crystallinity, indicating a higher resistance against hydrogen etching. This finding confirms the idea of a-Si:H being more susceptible to hydrogen etching than μc-Si:H.

2.3.3 Chemical annealing model

The chemical annealing model was introduced to explain an effect seen for a very specific deposition process. Nakamura et al. [34] observed that microcrystalline material can be grown by an alternating sequence of a-Si:H deposition and a hydrogen plasma treatment (layer-by-layer technique). The deposition rate of the material did not change, indicating that there was no etching of the film. Nakamura et al. concluded that the microcrystalline growth is caused by a rearrangement of the amorphous material, leading to the formation of crystals. This rearrangement is believed to be facilitated by hydrogen, penetrating the surface of the film.

Another study on layer-by-layer growth of microcrystalline silicon showed a different result. Vetterl et al. observed a decreasing growth rate with an increasing hydrogen treatment time [35]. This effect was attributed to hydrogen etching as discussed in the previous section. For extended hydrogen treatment times the material started to grow microcrystalline. Once the material grew microcrystalline, the grwoth rate stabilized. This finding is different from the work of Nakamura et al., indicating that the observation may depend on the process parameters of the hydrogen plasma treatment.

All three models focus on the role of hydrogen for the deposition of μc-Si:H material. They all indicate that a high density of atomic hydrogen promotes microcrystalline growth. This finding corresponds well with the low silane concentration / high hydrogen dilution process condition, typically applied to deposit μc-Si:H.

2.4 Material properties

2.4.1 Optical properties

Hydrogenated amorphous silicon and hydrogenated microcrystalline silicon are both semiconductors. Accordingly, photons need to have a certain energy in order to generate an electron–hole pair. This energy corresponds to the band gap E_g of the material as defined by the difference between valence band and conduction band.

Hydrogenated microcrystalline silicon has a band gap of 1.1 eV, similar to crystalline silicon. The transition of an electron from the valence band to the conduction band has to be facilitated by a phonon. The μc-Si:H material is therefore referred to as an indirect semiconductor. The chance of the photon to be absorbed is reduced because of the required phonon. Hence, the absorption coefficient is lower than for direct semiconductors (these materials do not require phonons to be involved).

Hydrogenated amorphous silicon has a different structure as has been shown in section 2.3. The deviations in bond lengths and bond angles allows photons to create electron–hole pairs without the assistance of a phonon. Hence, the absorption coefficient of a-Si:H is significantly higher compared to μc-Si:H for most wavelengths. The photons are absorbed more quickly, allowing the a-Si:H layers to be made only a few hundred nanometers thin (μc-Si:H absorber layers are typically 1–2 micrometers).

Additionally, the band gap of hydrogenated amorphous silicon is much higher (1.6–1.9 eV) compared to hydrogenated microcrystalline silicon. As a result both materials absorb different parts of the solar spectrum (see section 2.5.6).

2.4.2 Dangling bonds and hydrogen incorporation

If amorphous silicon is deposited by PECVD without any hydrogen the defect density due to dangling bonds is very high, resulting in electrical properties that impede any use in electronic devices. It was not until Chittick et al. introduced the PECVD technique using hydrogen containing gases that the material quality was radically improved [25].

The reason for the improved material quality is attributed to the presence of hydrogen atoms. These atoms passivate the dangling bonds that would otherwise act as recombination centers for photo-generated charge carriers. The recombination would lead to a reduced collection of photo-generated charge carriers. Only a fraction of the charge carriers could be extracted, reducing the current that can be drawn from the solar cell.

Microcrystalline silicon grows in small grains with a diameter in the order of a few tens of nanometers. Within the grains there are only very few dangling bonds that need passivation. For this type of material the passivation of the grain boundaries is much more important. The size of the crystals is much smaller than the thickness of a typical μc-Si:H solar cell. Hence, a large number of grain boundaries have to be passed by the charge carriers in order to get to the front or back contact of the solar cell. If the grain boundaries are not passivated well enough many charge carriers will recombine.

2.4.3 Staebler-Wronski effect

A few years after the first implementation of an a-Si:H layer it was shown that the conductivity of the intrinsic layer is reduced during light exposure [7]. The effect is attributed to an increase in the defect density of the layer and thus, a higher recombination rate of charge carriers.

The absorption of photons leads to the generation of charge carriers and the dissipation of the excess energy as heat. During the recombination of charge carriers their energy is converted into thermal energy as well. This energy may facilitate the breakage of weak bonds or the release of hydrogen from a dangling bond. Both processes lead to an increase in the defect density.

Figure 2.6 displays the solar cell efficiency η, depending on the degradation time t. During light soaking the efficiency of a-Si:H solar cells decreases due to a strong loss in the fill factor caused by the increasing defect density. The effect is typically more pronounced for solar cells with a thick intrinsic layer as well as for an increasing deposition rate r of the intrinsic layer.

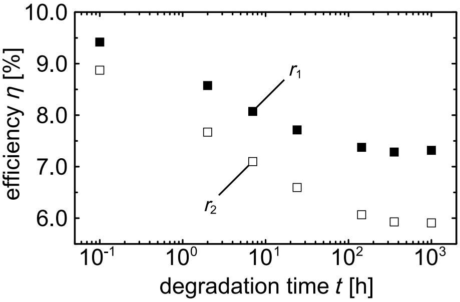

Figure 2.6: Exemplary degradation of the efficiency η for two a-Si:H solar cells as a function of the degradation time t and growth rate r of the intrinsic layer (with $r_1 < r_2$).

Because of the Stabler-Wronski effect a-Si:H solar cells are light soaked for 1000 h under a AM1.5 illumination (see section 2.5.5) at 50°C and open-circuit conditions. After this time the efficiency of the solar cell is typically stable (see figure 2.6).

2.5 Characterization methods

2.5.1 Conductivity measurement

One of the first techniques used to characterize the electrical properties of a-Si:H has been the conductivity measurement [7]. We distinguish between two different types of conductivity - the dark-conductivity σ_d and the photo-conductivity σ_ph.

Without illumination only thermally generated charge carriers contribute to the current transport. For a-Si:H the dark-conductivity σ_d is in the order of 10^{-11} S/cm. At a chosen voltage of 100 V and a film thickness of 1 μm the current is as low as 1 pA. In order to avoid side effects at this very low current level (e.g. due to humidity) the measurement is carried out in a vacuum chamber.

The photo-conductivity σ_ph of the film is measured under an illumination that matches the intensity of the standard solar spectrum AM1.5 (see section 2.5.5). The additional photo-generated charge carriers contribute to the current transport and lead to a photo-conductivity that is several orders of magnitude higher than the dark-conductivity. The ratio between photo- and dark-conductivity is called photosensitivity.

In order to determine the conductivity of single layers the films are deposited on a glass substrate. Two silver pads are evaporated onto the layer resulting in a co-planar structure with a pad width w_p and a pad distance d_p. If the film thickness d_film is known the conductivity σ can be calculated by

$$\sigma = \frac{d_\mathrm{p}}{w_\mathrm{p} d_\mathrm{film}} \frac{I}{V}. \tag{2.3}$$

In this formula I represents the current being measured for an applied voltage V. The pad width and pad distance are set to 5 mm and 0.5 mm, respectively. All samples are annealed at 160°C for 30 minutes in the vacuum chamber, prior to the measurement. The annealing procedure ensures a contact with low resistivity between the metal and the semiconductor. Otherwise, a four-point probe resistivity measurement may be required.

2.5.2 Photothermal deflection spectroscopy

In order to determine the absorption coefficient α of a film photothermal deflection spectroscopy (PDS) can be applied [36]. The concept of PDS is based on the idea that the absorption of photons causes the absorbing material to heat up. The change in temperature leads to a change in the refractive index of the material which can be detected through the deflection of a beam probing the sample. The deflection is thus proportional to the induced heat and therefore to the absorption coefficient.

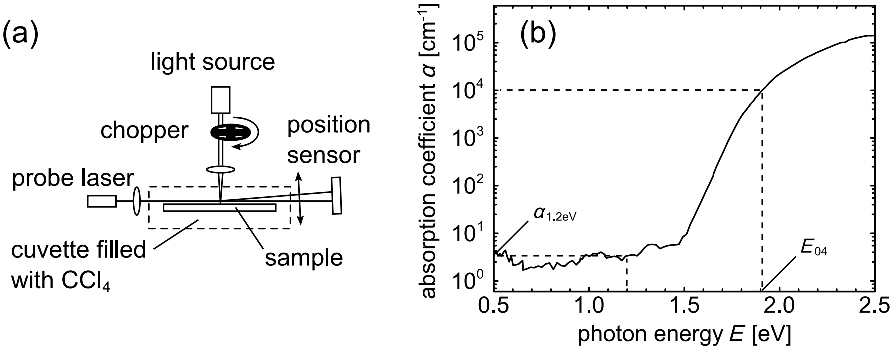

Figure 2.7: a) Schematic of the PDS measurement setup and b) absorption spectrum for an a-Si:H layer as obtained by PDS.

The configuration deployed in this work uses a slightly modified setup. The sample itself is fixed in a cuvette filled with carbon tetrachloride (CCl_4). Instead of probing the silicon film directly the beam is deflected within the liquid CCl_4 which is heated by the sample. The carbon tetrachloride is transparent and has a refractive index which is very sensitive to the temperature. Therefore even small changes in temperature caused by the absorption in the silicon film lead to a deflection that can be detected.

The basic PDS setup is shown in figure 2.7a. Monochromatic light is chopped and directed onto the sample. The probing laser beam is directed parallel and close to the substrate and onto a detector. Depending on the changes in the refractive index the beam is deflected and used as an indication for the absorption at a given wavelength. In order to account for changes in the light intensity and the light lost in transmission two additional monitor detectors are used (not shown in figure 2.7a).

Figure 2.7b displays the absorption spectrum of an intrinsic a-Si:H layer as obtained by PDS. For a-Si:H material the energy at which the absorption coefficient α becomes 10^4 cm^{-1} is referred to as E_{04} gap. Furthermore the sub-gap absorption $\alpha_{1.2\ \mathrm{eV}}$ between 1.1–1.3 eV can be used as a measure for the defect density [37, 38].

2.5.3 Raman spectroscopy

The method of Raman spectroscopy is based on the inelastic scattering of light due to the interaction with matter. Some of the incoming light interacts with vibrational modes of the material causing phonons to be created (Stokes peak) or absorbed (anti-Stokes peak). Hence, the frequency of the light is shifted. This shift is characteristic for the investigated material.

Due to its lattice structure and the very few defects single-crystalline silicon has a very narrow Stokes peak at a wavenumber of 520 cm^{-1} (transverse optic (TO) mode). Hydrogenated microcrystalline silicon (μc-Si:H) incorporates a large number of grain boundaries and some defects. As a result the TO mode shifts slightly towards lower wavenumbers and shows an asymmetric profile. For a-Si:H material the TO mode becomes even broader because of the large spread in bond lengths and bond angles. This spread results in a much wider range of possible phonon energies. Additionally, the peak center shifts to a wavenumber of about 480 cm^{-1}.

In order to determine the Raman crystallinity $I_{\mathrm{c}}^{\mathrm{RS}}$ the Raman spectrum is fitted between 400 cm^{-1} and 560 cm^{-1} with a linear baseline and an amorphous reference spectrum [39]. The difference between the measurement and the fit is attributed to the microcrystalline volume fraction of the material (see figure 2.8). The Raman crystallinity is calculated as

$$I_\mathrm{c}^\mathrm{RS} = \frac{I_\mathrm{c}}{I_\mathrm{a} + I_\mathrm{c}}, \tag{2.4}$$

with I_c and I_a being the areas of the two peaks corresponding to the crystalline phase and amorphous phase, respectively. A laser wavelength of 532 nm is used for all Raman measurements in this work, the Raman measurement is carried out from the layer side.

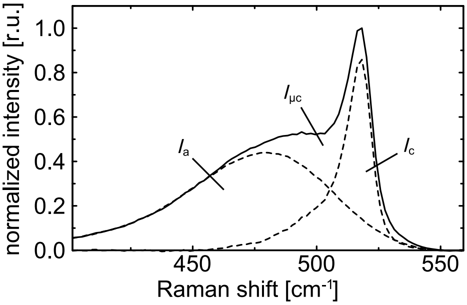

Figure 2.8: Raman spectra of a μc-Si:H layer and its deconvolution into the amorphous phase (I_a) and crystalline phase (I_c).

2.5.4 Fourier transform infrared spectroscopy

The silicon-hydrogen bonds found in a-Si:H and μc-Si:H are infrared active which means that vibrational modes can be excited with infrared light. This excitation of modes leads to an absorption which can be quantified by Fourier transform infrared (FTIR) spectroscopy. Typically two modes are analyzed to characterize the bonding configuration of hydrogen and the amount of hydrogen incorporated.

At a wavenumber ω of 640 cm^{-1} the wagging modes of SiH, $\mathrm{SiH_2}$ and $\mathrm{SiH_3}$ are found. The wagging mode was chosen to determine the hydrogen concentration c_H of the layer. First the absorption coefficient $\alpha(\omega)$ obtained by FTIR spectroscopy is corrected for multiple reflections. Maley et al. suggest to multiply the absorption coefficient $\alpha(\omega)$ for films with a low thickness d with a thickness dependent factor [40] giving

$$\alpha'(\omega) = \frac{\alpha(\omega)}{1.72 - 12\omega d}. \tag{2.5}$$

The corrected absorption coefficient $\alpha'(\omega)$ is then used to calculate the integrated absorption I

$$I = \int \frac{\alpha'(\omega)}{\omega} d\omega. \tag{2.6}$$

According to Langford et al. [41] the hydrogen density n_H is then determined as $n_\mathrm{H} = A_{640} I$ with A_{640} being a proportionally constant of 2.1×10^{19} cm^{-2}. The hydrogen concentration c_H is deduced from the hydrogen density as

$$c_\mathrm{H} = \frac{n_\mathrm{H}}{n_\mathrm{H} + 5 \times 10^{22}\ \mathrm{cm}^{-3}}. \tag{2.7}$$

Additionally, the stretching modes of SiH, $\mathrm{SiH_2}$ and $\mathrm{SiH_3}$ are analyzed to determine the bonding configuration. For dense material typically only one hydrogen atom bonds to a silicon atom (SiH) while more porous material also allows two or three hydrogen atoms bonding to a silicon atom ($\mathrm{SiH_2}$ and $\mathrm{SiH_3}$; e.g. at voids or grain boundaries). While the SiH stretching mode is found at 2000 cm^{-1}, the $\mathrm{SiH_2}$ and $\mathrm{SiH_3}$ stretching modes are found at 2090 cm^{-1}. Hence, it is possible to distinguish between dense and porous material by comparing the two modes. The parameter describing the porosity of the material is called the microstructure factor R.

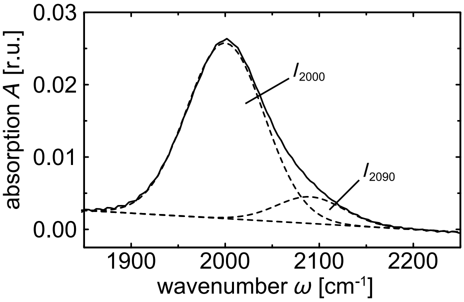

Figure 2.9: Exemplary stretching mode peak for intrinsic a-Si:H as obtained by Fourier transform infrared spectroscopy and its deconvolution into two Gaussian peaks at 2000 cm^{-1} (I_{2000}) and 2090 cm^{-1} (I_{2090}).

In figure 2.9 the stretching mode peak and its deconvolution can be seen. After subtracting a linear background between 1900 cm^{-1} and 2200 cm^{-1} the FTIR spectrum is fitted with two Gaussian peaks centered at 2000 cm^{-1} and 2090 cm^{-1}. The integrated absorption I determined for the two peaks (I_{2000} and I_{2090}) was used in order to calculate the microstructure factor R

$$R = \frac{I_{2090}}{I_{2000} + I_{2090}}. \tag{2.8}$$

The infrared absorption measurements were executed with a NICOLET 5700 FT-IR spectrophotometer using layers deposited on mono-crystalline silicon. The reference spectrum was measured using a blank mono-crystalline silicon wafer.

2.5.5 Current-voltage measurement

The most important technique to assess the performance of solar cells is the current-voltage measurement (IV-measurement). As the insolation changes during a year and throughout the day, an average spectrum has been defined by the American Society for Testing and Materials [42]. The AM1.5 spectrum has been chosen as a reference as it represents an average level of insolation on the earths surface. Figure 2.10 shows the standard spectrum in terms of spectral irradiance E_e versus the wavelength of the incoming light. Integrating the spectral irradiance E_e of the AM1.5 spectrum gives a value of $E_{\mathrm{AM1.5}} = 1000$ W/m^2 (or 100 mW/cm^2).

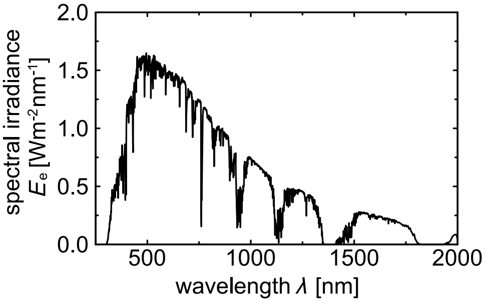

Figure 2.10: Spectral irradiance E_e depending on the wavelength of the light for the standard spectrum AM1.5 as defined by the American Society for Testing and Materials [42].

As can be seen in figure 2.10, most of the sun's energy is conveyed within the wavelength region of 350 nm to 1800 nm. Depending on the solar cell material different parts of the spectrum are utilized. For crystalline silicon wavelengths up to 1100 nm are absorbed while for amorphous silicon wavelengths up to about 800 nm are absorbed.

Figure 2.11 shows the current-voltage curve of a solar cell as measured under AM1.5 illumination. The parameters derived from the measurement are the open-circuit voltage V_{OC}, the short-circuit current density J_{SC} (given by the ratio of the short-circuit current I_{SC} and the solar cell area A), the fill factor FF and the efficiency η.

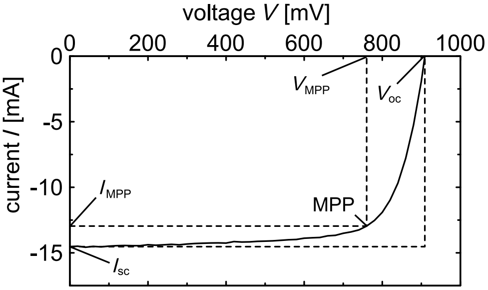

Figure 2.11: Exemplary current-voltage curve of a solar cell as measured under AM1.5 conditions.

At open-circuit voltage or short-circuit current conditions the product of voltage and current is zero – no power can be drawn from the solar cell in these points of operation. However, there is a maximum power point (labeled MPP) somewhere in between these two states. The ratio of the maximum power produced to the product of open-circuit voltage and short-circuit current is defined as fill factor

$$FF = \frac{I_{\mathrm{MPP}} V_{\mathrm{MPP}}}{I_{\mathrm{SC}} V_{\mathrm{OC}}}. \tag{2.9}$$

The efficiency η of the solar cell is given by the ratio of the maximum power produced by the cell to the product of irradiance $E_{\mathrm{AM1.5}}$ and cell area A as

$$\eta = \frac{I_{\mathrm{MPP}} V_{\mathrm{MPP}}}{E_{\mathrm{AM1.5}} A}. \tag{2.10}$$

The current-voltage curves of the solar cells are measured under AM1.5 illumination at 25°C using a WACOM class A sun simulator. The solar cells are annealed for 30 minutes at 160°C prior to the measurements. Unless stated otherwise the solar cell area is 1 cm^2.

2.5.6 Differential spectral response

The differential spectral response (DSR) measurement is used to obtain information about the extraction of photo-generated charge carriers. Depending on the wavelength λ and energy E of the light the photons are absorbed in different regions of the solar cell (see figure 2.1). As a consequence the charge carriers have to travel a shorter or longer path through the solar cell.

The external quantum efficiency (EQE) defines the ratio of electron-hole pares that can be extracted to the number of photons impinging on the solar cell. In the measurement setup this is translated to the electrical current delivered by the solar cell and the photon flux impinging on the solar cell, respectively. The EQE changes depending on the recombination and generation of charge carriers, the parasitic absorption and the electric field in the solar cell. The dependence on the electric field can be used in order to enhance the extraction of charge carriers by applying an external electric field.

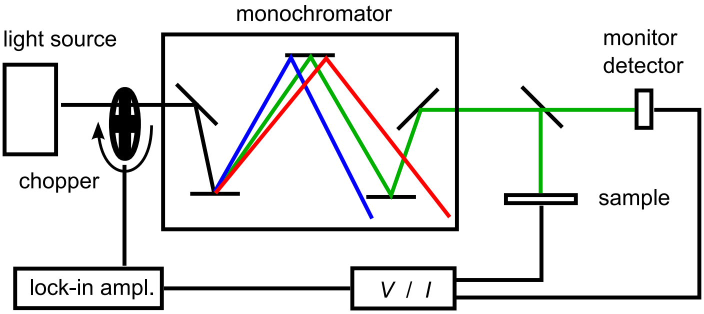

Figure 2.12: Differential spectral response (DSR) measurement system to determine the external quantum efficiency (EQE) of a solar cell.

The DSR measurement system is displayed in figure 2.12. It consists of a light source, a grated monochromator, a monitor diode, the solar cell, a current-to-voltage converter, a lock-in amplifier and a computer. The monochromator is needed in order to filter out narrow bandwidths of about 10 nm. These narrow parts of the light spectrum can be used to determine the external quantum efficiency at a certain wavelength.

For system calibration a solar cell with a known external quantum efficiency is used to determine the photon flux for the different wavelengths. In order to compensate any changes over time the light is split and one part of the light is always measured by a monitor diode. The current delivered by the monitor diode serves as a reference. This way intensity changes of the light source are monitored.

The external quantum efficiency accounts for any losses related to the solar cell structure. Hence, these losses depend on the properties of the substrate, the TCO layers and the silicon layers. A very detailed analysis of the optical and electrical losses can be found in ref. [43].

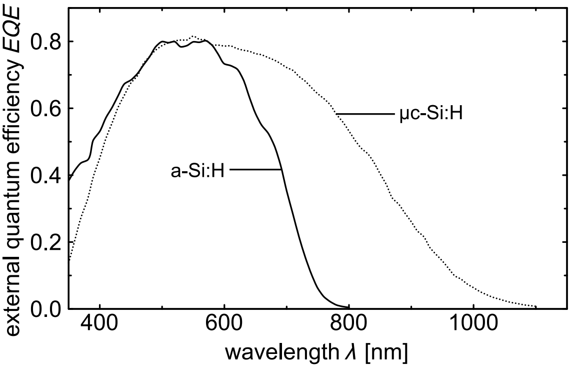

Figure 2.13: Exemplary external quantum efficiency as a function of the wavelength for an a-Si:H solar cell (solid line) and a μc-Si:H solar cell (dotted line).

Figure 2.13 shows the external quantum efficiency of an a-Si:H and a μc-Si:H solar cell. The μc-Si:H solar cells absorbs photons in a much wider wavelength range due to its lower band gap of 1.1 eV. This results in higher short-circuit current densities compared to a-Si:H solar cells.

3 Development of a dynamic deposition technique for thin-film silicon

In section 2.2 the basic concept of plasma-enhanced chemical vapor deposition (PECVD) was presented. In the present chapter a closer look is taken on the challenges related to the up-scaling of very-high frequency PECVD (VHF-PECVD) systems to large areas. State-of-the-art systems and the concept of dynamic deposition using linear plasma sources are described. The basic requirements for a homogeneous dynamic deposition process are identified and a dynamic deposition system is developed. At the end of the this chapter the process sequence for the preparation of single junction a-Si:H and μc-Si:H solar cells is outlined.

3.1 Large area deposition using very-high frequencies

Every solar cell technology is pursuing lower production costs as measured in \$/W and there are several ways to achieve this goal. The most direct way is to increase the efficiency and thus the power output of a solar module. Another option is to lower the material consumption in order to reduce the material cost. Additionally, the manufacturing cost can be lowered by increasing the productivity of a system which reduces the equipment-related costs. In the case of thin-film silicon solar cells the last point can be accomplished by increasing the substrate area or the deposition rate of the material.

In chapter 1 it was mentioned that the use of very-high frequencies is beneficial for the deposition of high quality μc-Si:H at high growth rates. However, if the electrode size is in the order of the wavelength of the VHF-signal, standing waves may occur. In this case the electrode potential becomes inhomogeneous leading to local differences in the strength of the electric field and thus, a non-uniform plasma density. In turn, this results in inhomogeneous layers in terms of film thickness and material properties.

A thin-film silicon solar module consists of many solar cells that are monolithically connected in series [44]. If the solar cell performance of one cell is reduced this affects the performance of the whole module. Hence, for highly efficient solar modules inhomogeneities have to be kept at a minimum.

3.1.1 State-of-the-art VHF-PECVD systems

Different system designs have been developed in order to minimize the standing wave effect related to the use of very-high frequencies on large areas. Schmidt et al. showed that a Gaussian-lens shaped electrode leads to a uniform plasma density [45].

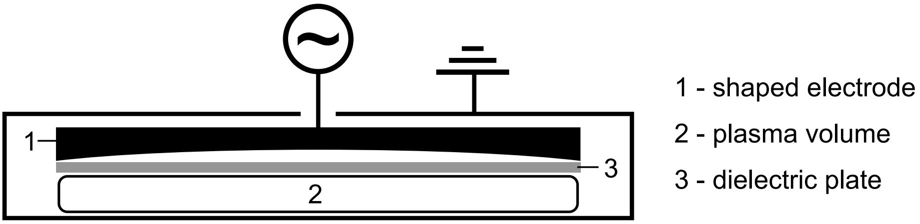

Figure 3.1: Design of a Gaussian-lens shaped electrode based on ref. [22].

For this electrode design the local electrode distance is adjusted in order to promote a constant electric field across the electrode (see figure 3.1). Additionally, the Gaussian-lens shaped electrode is covered with a dielectric plate to ensure a geometrically constant plasma thickness. As a result a homogeneous plasma density over the whole substrate area is accomplished.

Two other electrode configurations were presented by Takagi et al. [23] and Takatsuka et al. [16, 46]. Both designs use an array of rods rather than a planar showerhead electrode (see figure 3.2). The power is fed in at multiple points to the electrode, instead of just one point as for a conventional large area electrode.

For the ladder-shaped electrode presented by Takatsuka et al. the power is fed to both sides of the ladder (see figure 3.2a). By shifting the phase of the VHF signal applied to one side, it is possible to avoid the build-up of standing waves. So far deposition rates of up to 3 nm/s have been presented for high-quality μc-Si:H absorber layers [18].

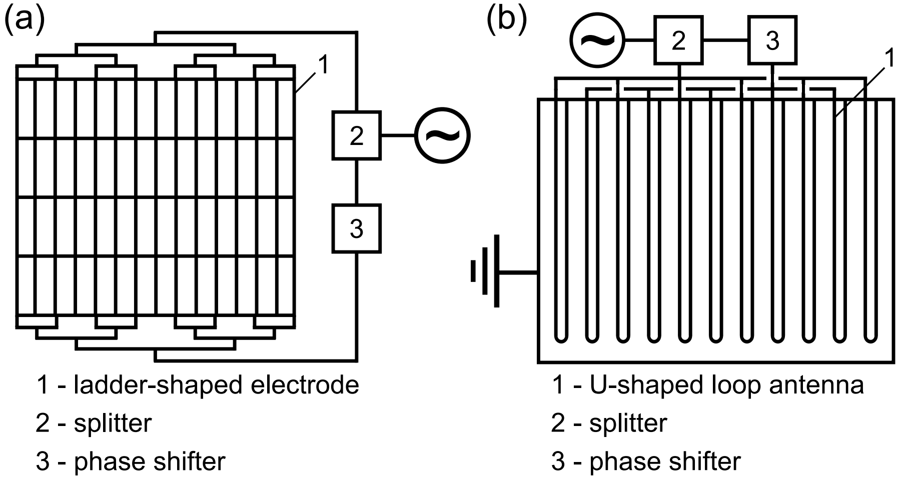

Figure 3.2: a) Design of a ladder-shaped electrode based on ref. [46]; b) Design of a U-shaped loop antenna electrode based on ref. [23].

The U-shaped loop antenna electrode presented by Takagi et al. works slightly different. There is no grounded counter-electrode as in a conventional parallel plate system. Instead, one end of the U-shaped loop is connected to the signal ground. The other end of the U-shaped loop is connected to the VHF signal (see figure 3.2a). However, if the same signal is applied to all of the U-shaped loops the deposition is inhomogeneous. In order to suppress the standing wave effect, the phase of the signal fed into every second loop is shifted by 180°. This so-called "anti-phase" configuration leads to a uniform deposition in both substrate dimensions [23].

A low deposition rate of 0.32 nm/s is obtained for μc-Si:H using an U-shaped loop antenna electrode, despite of an excitation frequency of 85 MHz [47]. Due to the electrode configuration two substrates can be processed at once, one at each side and parallel to the U-shaped loop antenna. This increases the throughput to the equivalent of one substrate at twice the deposition rate (0.64 nm/s). However, the throughput is still considerably lower than for the ladder-shaped electrode.

All three concepts apply showerhead electrodes which feed the gas to the deposition zone through multiple orifices in the electrode in order to promote a homogeneous gas distribution. The homogeneous gas distribution is a prerequisite for uniform static deposition process on large areas (along with the homogeneous plasma density).

In the subsequent section the concept of dynamic deposition using linear plasma sources is presented. This concept is believed to be better suited for the up-scaling of VHF-PECVD processes to large areas while using a simple electrode design.

3.1.2 Concept of dynamic deposition using linear plasma sources

In the present work a dynamic VHF-PECVD technique using linear plasma sources is developed. By using these electrodes that only extend in one direction, the standing wave effects can be controlled more easily. The linear plasma sources are based on a parallel plate electrode configuration. However, contrary to a static deposition technique the substrate moves in front of and parallel to the electrodes [24]. This deposition concept is different from the static deposition systems described in the previous section.

For dynamic deposition processes the homogeneity has to be guaranteed in only one electrode dimension: along the length of the electrode, perpendicular to the substrate movement direction. The homogeneity in the second dimension (in movement direction of the substrate) is ensured by stable plasma conditions in combination with the constant substrate velocity. As a result every point on the substrate encounters the same deposition conditions throughout the deposition process.

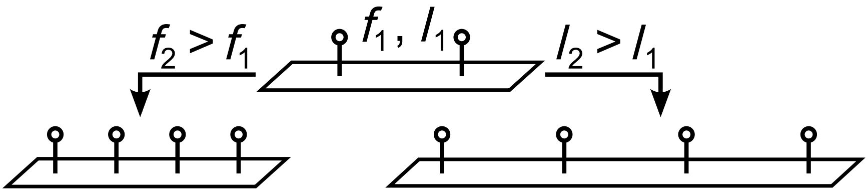

Figure 3.3: Concept of the linear plasma sources. The number of power feed in points scales with the length l of the electrode and the excitation frequency f.

In the present work the linear plasma sources are chosen to be only a few 10 cm wide. Their length however, can be adapted to the size of the substrate (currently up to 2.2 × 2.6 m^2 for a generation 8.5 substrate [48]). Hence, for electrode lengths larger than one tenth of the VHF wavelength the standing wave effect occurs in the direction perpendicular to the substrate movement. Therefore, the number of power feeds along the electrode has to be adapted to its length l and the excitation frequency f (see figure 3.3). As a result a more homogeneous voltage distribution is achieved.

At frequencies above 100 MHz standing waves may occur along the width of the electrode. However, due to the nature of the dynamic deposition process this is not necessarily a problem. The dynamic deposition process will result in a homogeneous layer growth in both substrate dimensions, as long as the plasma conditions are stable and homogeneous along the length of the electrode.

For an industrial system a continuous stream of substrates is envisaged to move in front of and parallel to the electrodes. A large number of linear plasma sources placed side by side would enable the deposition of intrinsic layers with thicknesses of several hundred nanometers with a high throughput.

3.2 Prerequisites for a uniform dynamic deposition process

It is assumed that the linear plasma sources guarantee a homogeneous voltage distribution perpendicular to the movement direction of the substrate. In addition the following requirements have to be fulfilled in order deposit homogeneously across the substrate area with a dynamic deposition process:

Stable carrier grounding In section 2.2.3 is was shown that the substrates are mounted onto a carrier in order to be transported within the deposition system. The electrical contact between the substrate carrier and the signal ground has to be reliable. If this condition is not met, the power supplied to the electrode may change, leading to a non-constant plasma composition or possible plasma outages.

Constant electrode distance The electrode distance may vary with time for a dynamic deposition due to the carrier movement. As a result, the plasma density can change. Sudden changes in the electrode distance may even cause the plasma to shut off.

Stable substrate temperature In section 2.2.2 it was mentioned that the substrate temperature has an influence on the growth process of thin-film silicon layers. As a consequence, the substrate temperature has to be kept within a few degrees Celsius.

Homogeneous gas distribution For conventional static deposition processes the gas has to be distributed homogeneously across the substrate area. For dynamic deposition processes it may be sufficient to distribute the gas homogeneously perpendicular to the movement direction of the carrier. An inhomogeneity in movement direction of the substrate carrier may be tolerable due to the dynamic deposition process itself. This subject is investigated in chapters 4 and 5.

3.3 Experimental realization of a dynamic deposition process

In the present section the challenges related to the development of a dynamic deposition technique are discussed. The aspects of plasma stability as well as homogeneity and stability of the process parameters are reviewed. The focus is on the design for the carrier grounding and the implementation of the dynamic deposition process in the LADA system. Additionally, a simple gas distribution system is presented, that is well suited for the dynamic deposition process.

3.3.1 Development of a stable carrier grounding

Plasma stability is an important requirement for the dynamic deposition process. The carrier has to move constantly, which is very different to the static deposition process. A permanent electrical contact between the substrate carrier and the grounded electrode shielding has to be implemented. The design used in this work consists of flat metal springs in combination with a long rail. The metal springs drag along the rail and allow enough flexibility to compensate for the carrier movement. However, even with a good electrical contact problems may occur (e.g. parasitic plasmas) as will be discussed in the following paragraphs.

Figure 3.4 displays the schematic of the initial grounding design. In this case the signal ground connects the electrode shielding to the inside of the deposition chamber. From there the current flows along the chamber walls towards the backside of the carrier (indicated by arrows in figure 3.4).

Though the electrical contact using this design is good, parasitic plasmas occurred, preferentially between the carrier and the heater as well as between the carrier and the gate valve housing. These parasitic plasmas result in an unstable plasma between the electrode and the carrier, leading to disruptions in the deposition process and sometimes a shutdown of the generators.

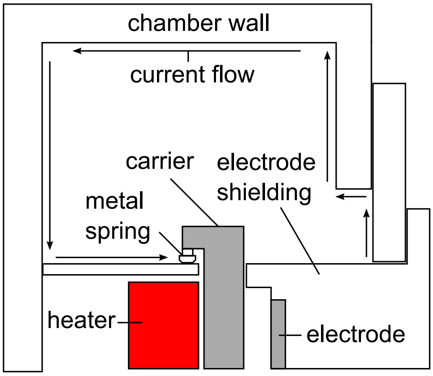

Figure 3.4: Schematic of the initial grounding design in PC2 of the LADA system. Arrows indicate the current flow for the signal ground.

A parasitic plasma may occur if two conditions are fulfilled. First, the combination of pressure and electrode distance has to provide a low threshold for plasma ignition (see "Paschen's Law" in section 2.2.2). Second, there has to be a difference in the electric potential between the two surfaces. If the electric field is strong enough a parasitic plasma is ignited.

In case of the LADA system, the distance between substrate carrier and heater as well as between substrate carrier and gate valve housing is roughly the same as the electrode distance. Therefore, a parasitic plasma may occur if the electric field is strong enough. The difference in the electrode potential can be caused by a phase difference in the signal ground between the two surfaces involved. Because the current flows along the chamber walls there can be a difference in the phase of the VHF-signal between the carrier and another surface, leading to a parasitic plasma.

The grounding of the carrier was evaluated and redesigned in order to avoid parasitic plasmas and promote stable plasma conditions. It was found through measurements of the carrier potential that only a direct connection between the grounded electrode shielding and the front of the carrier provides the conditions needed to successfully suppress parasitic plasmas.

Figure 3.5 shows the final grounding design. The electrical contact is made directly from the grounded electrode shielding to the front side of the carrier. As a result no current flows along the inner walls of the chamber or the backside of the carrier. Hence, no difference in the electric potential is created which would lead to parasitic plasmas. With the final grounding design parasitic plasmas are suppressed successfully.

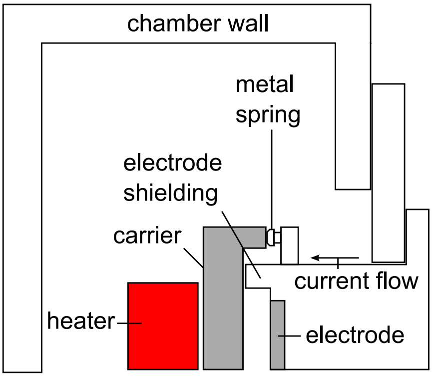

Figure 3.5: Schematic of the final grounding design in PC2 of the LADA system. Arrows indicate the current flow for the signal ground.

3.3.2 Design of the transport system

The carriers are moved throughout the LADA system using a number of actively powered rolls underneath the carrier. In order to ensure a parallel movement in front of the electrodes, the carriers are guided along a number of secondary rolls at the top of the carrier. The alignment of these secondary rolls ensures a stable distance between the electrodes and the carriers. The alignment error is less than ±1 mm. For the chosen geometry the alignment error has not proven to be critical for the plasma stability.

In an industrial reactor the substrates will move parallel to and in front of many linear plasma sources to deposit the intrinsic layer. In contrast, the LADA system contains only two linear plasma sources. Hence, the industrial process is simulated by moving the substrates back and forth until the desired layer thickness is deposited.

The substrates have to leave the plasma completely before the transport direction changes. Otherwise the deposition may become inhomogeneous because not every point on the substrate would encounter the same deposition conditions. Nevertheless, there always has to be a counter-electrode for the linear plasma sources, even during the times when the substrates are outside of the deposition area. There are two options to meet this requirement:

One way would be to make the substrate carrier long enough to constantly serve as the counter-electrode. The drawback of this design is a long and very heavy carrier. The transport distance between both turnaround points is roughly one meter. Adding the width of both linear plasma sources and the distance between them gives a total of about 1.5 m. A carrier of that length is not feasible for a laboratory scale system.

For this work a more practical solution has been chosen. The substrate carrier is made about 54 cm long. By itself this carrier is too short for a dynamic deposition process. Therefore, two so-called “dummy” carriers (one to each side of the substrate carrier) serve as counter-electrodes during the times the substrate carrier is outside the plasma (see section 2.2.3).

All three carriers move simultaneously within the system at the same speed to ensure that the gap between the carriers remains small. This configuration ensures that the plasma remains stable throughout the dynamic deposition process. Note, that the carriers are not connected mechanically or electrically. The chosen carrier configuration could also be implemented in an industrial deposition system

3.3.3 Temperature control during dynamic deposition processes

In section 2.2.3 it was shown that the substrate temperature is measured from the backside of the carrier using a pyrometer. Therefore, a small hole was drilled into the carrier in order to enable a temperature reading of the substrate. In case of a static deposition process, there is a permanent temperature reading which enables a continuous adjustment of the heater temperature.

During a dynamic deposition process the time t between two measurements is determined by the distance d between the two turnaround points (about 1 m) and the substrate carrier velocity v. A high carrier velocity would enable short response times, but there is a limitation. The hole in the carrier is about 8 mm in diameter. The pyrometer measures on the glass with a spot diameter of roughly 3 mm. From the minimal pyrometer integration time of 80 ms it is calculated that the maximum carrier velocity would be about 60 mm/s.

For this velocity there is only one temperature reading of the substrate for each pass of the carrier. Any other reading before or after this particular reading would be partially on the backside of the carrier. To improve the reliability of the temperature reading the substrate carrier velocity for all dynamic depositions is set to 15 mm/s (0.9 m/min). Hence, the time between two readings is a little more than one minute.

For the deposition of a-Si:H this carrier velocity is high enough to keep the substrate temperature within ±2 K (see figure 3.6a). In contrast to that, the temperature increases during the dynamic deposition of μc-Si:H (see figure 3.6b). The same effect is observed for statically grown μc-Si:H layers.

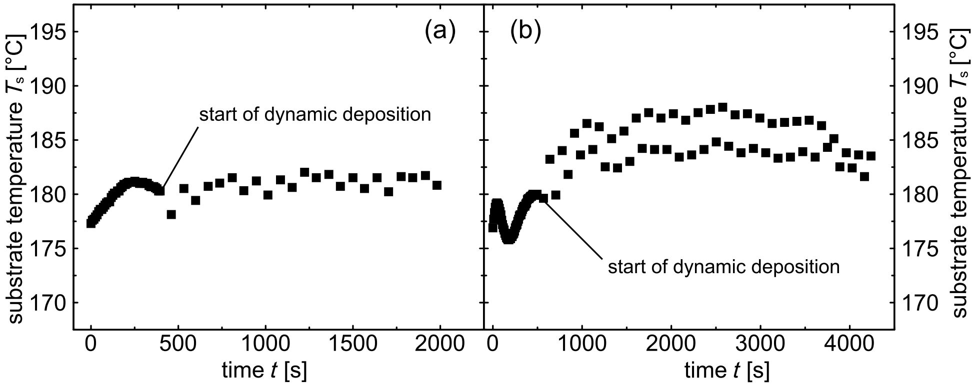

Figure 3.6: Temperature readings of the substrate during dynamic a) a-Si:H layer deposition and b) μc-Si:H layer deposition processes. In case of the μc-Si:H deposition process there is a temperature drift due to plasma-induced substrate heating.

This increase in substrate temperature is attributed to plasma-induced substrate heating. A similar observation has been reported by van den Donker et al. [49]. In this work it was not possible to fully counter-balance the plasma-induced substrate heating by adapting the heater temperature during high-rate growth of μc-Si:H.

3.3.4 Linear gas distribution system

In conventional PECVD systems a showerhead electrode promotes a homogeneous gas distribution. However, the manufacturing of this type of electrode for large areas is complex and costly. The concept of the dynamic deposition process requires homogeneous plasma conditions only along the length of the electrode. Possible changes in the gas composition in movement direction of the substrate may be tolerable because every point on the substrate encounters the same deposition conditions.

A linear gas distribution system is chosen in the present study to investigate the feasibility of such a configuration. The gas is injected between the two linear plasma sources and pumped out at the outer edges – this configuration is referred to as cross-flow design (see figure 3.7). Separating the gas distribution from the electrode design simplifies the manufacturing of the electrode considerably. Additionally, cleaning or replacing the electrode becomes much easier. Therefore, this configuration is promising for industrial application.

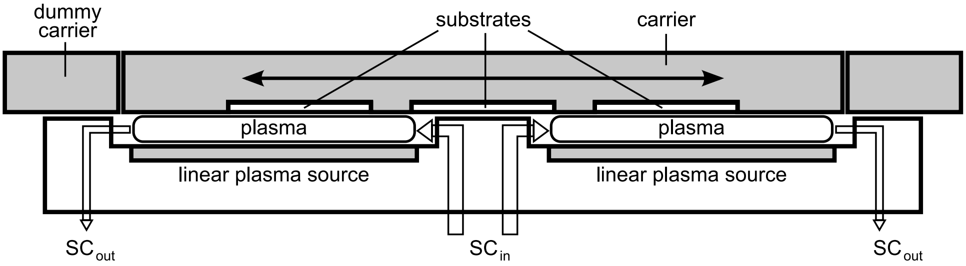

Figure 3.7: Schematic of the linear gas distribution system, implemented in PC2 of the LADA system (top view). The gas enters the chamber between the linear plasma sources with the silane concentration SC_{in} and is pumped at the outer edges of the electrode with SC_{out}.

In a cross-flow configuration the silane concentration changes along the gas flow direction because silane molecules are dissociated and the resulting radicals may be deposited on the electrode and carrier. The change in silane concentration may lead to changes in the material growth. Therefore, the implications of the chosen gas distribution system are studied in chapters 4 and 5.

3.4 Process sequence for thin-film silicon solar cells

In the present section the process sequence for the deposition of p–i–n a-Si:H and μc-Si:H thin-film solar cells is outlined. This sequence has been developed in order to ensure the reproducibility and comparability of RF- and VHF-PECVD processes.

First, the glass substrates, coated with a transparent conductive oxide (TCO), are mounted on the carrier. The carrier is preheated in the load lock for 10 minutes in order to evaporate water adsorbed to the surface. Afterwards the substrate carrier is transported into PC 1.

From there on the PECVD process sequence is an alternation of single layer deposition processes and ex-situ CO_2 plasma treatments. All PECVD processes follows the same procedure:

- waiting for base pressure to be lower than 9×10^{-7} mbar
- opening gas valves and mass flow controllers, stabilize pressure at chosen level
- stabilizing substrate temperature
- starting plasma for deposition process
- shutting off the plasma, pump the process gases
- purging with argon for 5 minutes

The deposition process sequence for a single junction solar cell consists of p-layer deposition, CO_2 plasma treatment, i-layer deposition, n-layer deposition and a final CO_2 plasma treatment.

After the PECVD processes an aluminum doped zinc oxide layer is sputtered onto the n-layer. Subsequently silver pads are evaporated onto the substrate to form the back contact. Both processes are carried out in different deposition systems. The solar cell size of 1 cm^2 is defined by a HCl etching step removing the ZnO:Al around the pads to avoid current collection.

In the present work commercial Asahi type U ($SnO:F_2$) substrates were used for a-Si:H solar cells while low-iron glass covered with a texture-etched aluminum doped zinc oxide (ZnO:Al) was used as substrate for μc-Si:H solar cells [50]. The μc-Si:H solar cells contain a 20 nm thick μc-Si:H p-layer while a-Si:H solar cells contain a 10 nm thick a-Si:H p-layer. In contrast, all μc-Si:H and a-Si:H solar cells contain the same a-Si:H n-layer. For details on the doped layers see appendix A.

Reducing the cross-contamination

Contrary to a cluster tool deposition system, the LADA system consists of two process chambers, one for RF- and one for VHF-PECVD. The gases that are used to dope the silicon layers (phosphine and trimethylboron for n- and p-doping, respectively) are solely connected to PC1. As a consequence of this setup p- and n-doped layers are deposited statically by RF-PECVD processes.

For solar cells with intrinsic layers grown by RF-PECVD all layers are deposited within PC1. Without additional process steps dopant atoms may be incorporated in the subsequently deposited layer, reducing the solar cell performance [51].

In order to minimize the problem of cross-contamination several chamber treatments have been suggested [15, 52, 53]. An ex-situ CO_2 plasma (substrate needs to be transported out of the chamber), a H_2O vapor flush or pumping the chamber to less than 10^{-6} mbar have proven to be successful to minimize the cross-contamination of boron. In the present work an ex-situ CO_2 plasma treatment is applied after every doped layer in order to keep cross-contamination to a minimum [53]. Therefore, the substrate carrier leaves PC1 and is replaced by a dummy carrier as counter-electrode during the CO_2 plasma treatment.

Determination of deposition rates for dynamic deposition processes

For any deposition process the deposition rate r can be calculated as $r = d/t$, with d being the layer thickness and t being the deposition time. For a static deposition rate this is straightforward. In case of dynamic deposition there are two different ways to quantify the deposition rate. First, an average deposition rate $\overline{r}$ can be calculated as

$$\overline{r} = \frac{d}{t} = \frac{dv}{nw}, \tag{3.1}$$

where v is the carrier velocity (0.015 m/s), n is the number of passes in front of the electrode and w is the total electrode width (40 cm in the LADA system). For a dynamic deposition process only an average deposition rate can be calculated. In order to obtain local growth rates it would be necessary to deposit the layer statically.

The second possibility is to define a dynamic deposition rate

$$r_{\mathrm{d}} = \frac{dv}{n}. \tag{3.2}$$

This quantity is related to the deposition rate and the specific geometry of the electrodes. The dynamic deposition rate increases with the electrode width, while the average dynamic deposition rate may remain constant. Therefore it is complicated to compare static and dynamic deposition rates. Hence, for this work the average deposition rate is chosen in order to compare static and dynamic deposition processes.

Note, that the layer thickness was measured using a DekTak surface profilometer with the silicon layer being removed locally by laser ablation.

3.5 Conclusions

In the present chapter the challenge of homogeneous VHF-PECVD processes on large substrate areas has been studied. First, state-of-the-art systems and their solution to the standing wave effect have been described. Subsequently, the concept of dynamic deposition was introduced and an experimental setup was developed.

The basic requirements for a homogeneous dynamic deposition process have been identified. The challenge of plasma stability and the aspect of parasitic plasmas was investigated. It was shown that this particular effect is related to the design of the carrier grounding. Parasitic plasmas were successfully suppressed by redesigning the carrier grounding.

The implications of the dynamic deposition process on the LADA system were discussed (e.g. carrier configuration and temperature stabilization). It was shown that the substrate temperature can be controlled successfully despite of the limited access to the substrate. Additionally, a simple gas distribution system was implemented that enables simpler electrode manufacturing and easier cleaning, while maintaining a homogeneous gas distribution along the length of the electrode.

At the end of this chapter the process sequence for the deposition of a-Si:H and μc-Si:H thin-film solar cells was presented. The results in chapters 4 and 5 have been obtained through experiments using the configuration and procedures developed in the present chapter.

4 Dynamic deposition of μc-Si:H solar cells

The μc-Si:H absorber layer makes up for most of the thickness of the silicon layers in an a-Si:H/μc-Si:H tandem solar cell [54–56]. Hence, the deposition rate of the μc-Si:H layer has a strong influence on the total deposition time. In the introduction it was pointed out that the use of very-high frequencies is beneficial for the properties of μc-Si:H grown at high deposition rates by PECVD when compared to radio-frequency PECVD processes. However, the application of very-high frequencies to large areas is challenging because the standing wave effect may lead to inhomogeneities in the deposition process.

In the previous chapter the concept of a dynamic deposition process using linear plasma sources was introduced. This concept is believed to be better suited for the up-scaling of VHF-PECVD processes to large substrate areas compared to systems using planar showerhead electrodes. In the present chapter static and dynamic processes are studied in order to identify possible implications of a dynamic deposition process using linear plasma sources on the quality of μc-Si:H. The aim is to study the influence of changing growth conditions during the deposition process and assess the potential of dynamic VHF-PECVD for the high-rate growth of high-quality μc-Si:H absorber layers.

4.1 Baseline static radio-frequency deposition process

It is known from literature that the efficiency of a μc-Si:H solar cell strongly depends on the crystallinity of the i-layer [57]. The crystallinity is typically varied by adjusting the silane concentration for the i-layer deposition process while keeping all other process parameters constant (see refs. [17, 58, 59]). A fixed set of process parameters (pressure, power, total gas flow, electrode distance, frequency, substrate temperature) is typically referred to as process regime.

In the present section a state-of-the-art RF-PECVD regime (sRFm1) using a showerhead electrode is applied in order to deposit i-layers with different crystallinities for μc-Si:H solar cells (for details on regime sRFm1 see table 4.1 and appendix B). The aim is to study the influence of the crystallinity on the photovoltaic parameters and investigate the correlation between silane concentration, deposition rate and crystallinity. For details on the process regime abbreviations and their meaning see appendix B.

Table 4.1: Static RF-PECVD regime for the growth of intrinsic μc-Si:H.

regime	frequency [MHz]	pressure [mbar]	power density [W/cm^2]	gas utilization [%]	growth rate at $I_{\mathrm{c,opt}}^{\mathrm{RS}}$ [nm/s]
sRFm1	13.56	12.5	0.33	60–65	0.53

4.1.1 Influence of the crystallinity on the solar cell performance

Solar cells incorporating i-layers grown in regime sRFm1 with different crystallinities have been deposited as a reference for all VHF-PECVD regimes. The crystallinity of the i-layer was varied by changing the silane concentration for the i-layer deposition process between 0.6–1.2 %. The i-layer thickness is kept constant between 1300-1400 nm in order to ensure that the effects seen are solely related to the crystallinity.

Figure 4.1 displays the photovoltaic parameters of μc-Si:H solar cells, depending on the Raman crystallinity. A maximum in efficiency of about 8 % is obtained at a Raman crystallinity between 50–70 % (see figure 4.1a). Within that range of crystallinities the solar cells deliver a short-circuit current density of 22–24 mA/cm^2, an open-circuit voltage of 480–520 mV and a fill factor of 66–68 %.

The solar cell efficiency declines towards very high crystallinities to about 6 % and it decreases towards low crystallinities to less than 3 %. The reduction in efficiency is partially caused by a decreasing fill factor as shown in figures 4.1a,b.

The high amorphous content at low crystallinity leads to a lower absorption of light in the infrared part of the spectrum. This effect contributes to the strong reduction in short-circuit current density towards low crystallinity as shown in figure 4.1c. The drop in efficiency towards high crystallinity is believed to be caused by an increasing void fraction [60, 61] and a poor grain boundary passivation, leading to a higher defect density. As a result, fill factor and open-circuit voltage are reduced.

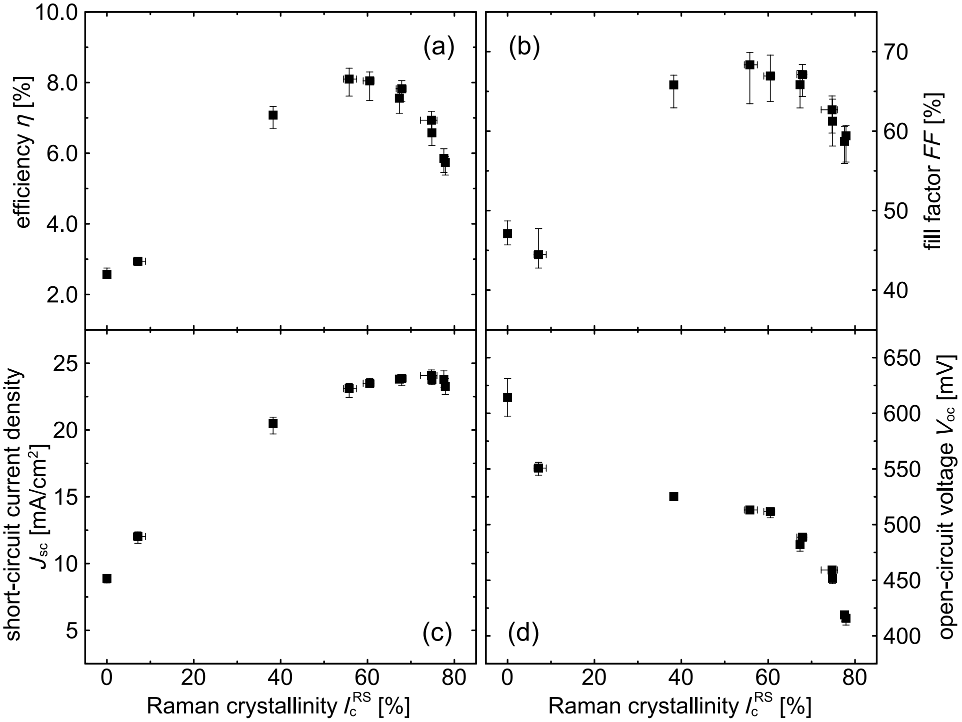

Figure 4.1: Efficiency η, open-circuit voltage V_{OC}, short-circuit current density J_{SC} and fill factor FF of μc-Si:H solar cells, depending on the Raman crystallinity I_c^{RS}. The solar cells incorporate i-layers grown statically in regime sRFm1.

In order to study the changes in short-circuit current density in more detail the external quantum efficiency (EQE) was measured. Figure 4.2 shows the EQE of μc-Si:H solar cells for different crystallinities. The solar cell with an optimum phase mixture [17] of the i-layer ($I_c^{\mathrm{RS}} = 56$ %) shows a high spectral response over a broad range of wavelengths. The EQE is almost independent of the bias voltage (dotted curve) which indicates a good charge carrier collection.

The spectral response improves for highly crystalline solar cells ($I_c^{\mathrm{RS}} = 78$ %) for wavelengths below 500 nm and above 850 nm. However, the EQE shows a bias voltage dependence which indicates a problem with the charge carrier collection. This problem may be caused by an increasing number of defects at high crystallinity.

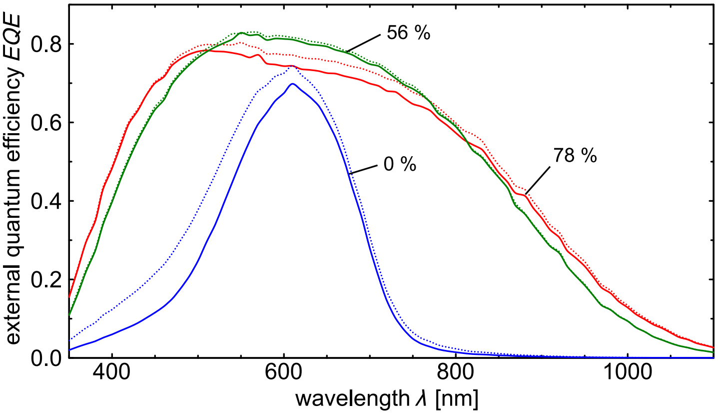

Figure 4.2: External quantum efficiency EQE depending on the wavelength λ of the incident light. The EQE is shown for a highly crystalline μc-Si:H solar cell (I_c^{RS} = 78 %), a solar cell with a Raman crystallinity I_c^{RS} of about 56 % and a solar cell with a very low crystallinity ($I_c^{RS} = 0$ %). The solid curves represent the EQE without bias voltage, the dotted curves represent the EQE at a bias voltage of -0.5 V.

For solar cells with a very low crystallinity ($I_c^{RS} = 0$ %) the EQE is significantly reduced across the whole spectrum. The reduction in the infrared part of the spectrum is due to the higher band gap of the amorphous material, leading to a reduced generation of charge carriers. At short wavelengths the EQE exhibits a strong bias voltage dependence which indicates a problem with the charge carrier collection close to the p/i interface. This finding indicates that the material quality is very low in the initial stage of layer growth.

4.1.2 Correlation between growth rate and crystallinity

In the previous section it was shown that there is a strong correlation between the crystallinity of the i-layer and the efficiency of μc-Si:H solar cells. The crystallinity was varied by using different silane concentrations for the i-layer deposition process. As a consequence, the growth rate changed due to the changing number of growth precursors. In the present section the correlation between silane concentration, growth rate and crystallinity is studied for reference regime sRFm1 (13.56 MHz, showerhead electrode).

Figure 4.3a shows the deposition rate of the μc-Si:H i-layer as a function of the silane concentration for regime sRFm1. A linear relationship between silane concentration and deposition rate is observed. The crystallinity decreases from 78 % at a deposition rate of 0.35 nm/s to 60 % at 0.53 nm/s, followed by a drop in crystallinity at higher deposition rates as shown in figure 4.3b.

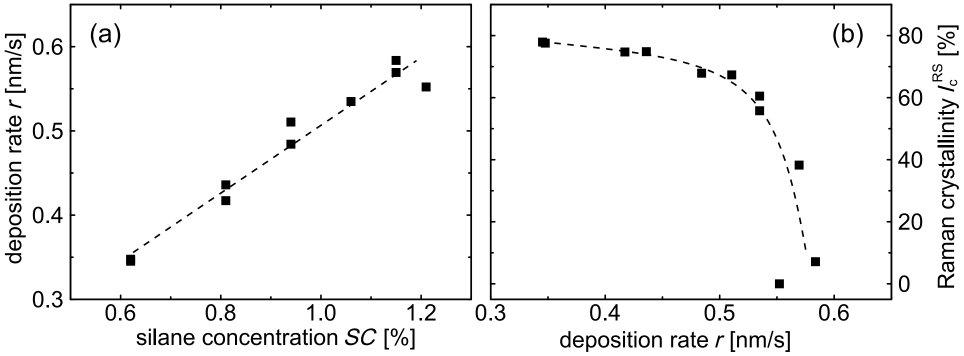

Figure 4.3: a) Deposition rate r of the i-layer as a function of the silane concentration SC and b) Raman crystallinity I_c^RS as a function of the deposition rate r of the i-layer. Lines are guides to the eye.

The optimum in solar cell efficiency is obtained for a Raman crystallinity of 50–70 %. According to figure 4.3 this corresponds to a deposition rate of 0.48–0.54 nm/s and a silane concentration of 0.94–1.08 % for regime sRFm1. Within the given range of crystallinity the open-circuit voltage and short-circuit current density vary by almost 10 %. Therefore, the process window for a homogeneous large-area deposition process may be more restrictive.

4.1.3 Summary

It was shown that μc-Si:H solar cells obtain the highest efficiency within a narrow range of crystallinities for a static RF-PECVD regime. The crystallinity itself strongly depends on the deposition rate of the i-layer which rises linearly with the silane concentration. Therefore, conventional large-area PECVD systems apply showerhead electrodes in order to promote a homogeneous gas distribution and facilitate a uniform deposition process.

In the subsequent section the implications of a linear gas distribution system are studied. The aim is to investigate the influence of an inhomogeneous gas composition on the uniformity of the deposition process.

4.2 Implications of a linear gas distribution system

In the present work linear plasma sources and a linear gas distribution system are applied for dynamic VHF-PECVD processes as shown in section 3.3.4. In this configuration the gas is injected into the chamber between the linear plasma sources and pumped at the outer edges, resulting in a gas flow parallel to the electrode (see figure 3.7). As the gas flow passes the electrode a part of the silane molecules is dissociated and the resulting radicals may be deposited on the substrate or electrode. Hence, the silane concentration decreases from the gas feed towards the exhaust [12, 62].

The aim of the present section is to study the implications of a linear gas distribution system on the homogeneity of a static deposition process. Two exemplary VHF-PECVD regimes are investigated which have been used to deposit the i-layers in μc-Si:H solar cells. The i-layers were grown statically in regimes sVHFm1 and sVHFm2, for details see table 4.2 and appendix B.

Table 4.2: Static VHF-PECVD regimes for the growth of intrinsic μc-Si:H.

regime	frequency [MHz]	pressure [mbar]	power density [W/cm^2]	gas utilization [%]	growth rate at $I_{\mathrm{c,opt}}^{\mathrm{RS}}$ [nm/s]
sVHFm1	60	4	0.22	55–65	0.65
sVHFm2	60	6	0.52	40–50	1.0

4.2.1 Homogeneity of solar cell performance

Microcrystalline silicon solar cells have been deposited incorporating i-layers grown statically in regimes sVHFm1 and sVHFm2 using linear plasma sources. Prior to the VHF-PECVD i-layer deposition process a 50 nm i-layer was deposited onto the p-layer using regime sRFm1 (showerhead electrode) and a silane concentration of 0.8 %. This was done in order to improve the homogeneity of the i-layers deposited statically by VHF-PECVD and to protect the p-layer from possible side effects (e.g. hydrogen etching).

Figure 4.4 shows the cross section of one half of the linear gas distribution system with a scale that depicts the distance to the gas feed x. For static VHF-PECVD processes the carrier is placed at the center of the two linear plasma sources. Hence, the substrates that are deposited with microcrystalline silicon extend from $x = 7.5$ cm to $x = 17.5$ cm.

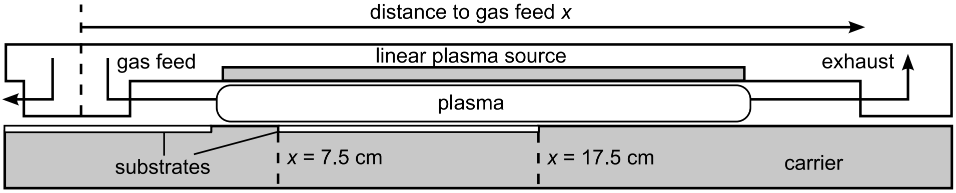

Figure 4.4: Schematic of one half of the linear gas distribution system according to figure 3.7 (top view), including a scale for the distance to the gas feed. Note, that the electrode extends from $x = 5$ cm to $x = 25$ cm.

Figure 4.5 shows the photovoltaic parameters of μc-Si:H solar cells with i-layers grown statically using the linear gas distribution system. The solid symbols represent regime sVHFm1 at $SC = 6.6$ % with an optimum phase mixture ($I_c^{RS} \approx 60$ %) grown at about 0.65 nm/s and a gas utilization of about 60 %. This regime was developed in order to obtain a similar growth rate and gas utilization as regime sRFm1 (see section 4.1).

The open symbols represent regime sVHFm2 at $SC = 2.2$ % with an optimum phase mixture grown at 1 nm/s and a gas utilization of about 45 %. This regime was developed to investigate the influence of a higher pressure and power density on the transition from microcrystalline to amorphous growth.

The efficiency of the μc-Si:H solar cells is plotted as a function of the distance to the gas feed in figure 4.5a. The error bars in the x-direction indicate the width of the solar cell of 1 cm. The efficiency of the best solar cell is close to 8 % for both deposition regimes of the i-layer. However, there is a very strong inhomogeneity in the photovoltaic parameters across the substrate in gas flow direction.

The solar cell efficiency is about 3 % close to the gas feed because of a low short-circuit current densities and a low fill factor. The efficiency then rises towards the exhaust because of a strong increase in short-circuit current density and fill factor. At the same time the open-circuit voltage decreases considerably. Close to the exhaust the efficiency decreases to about 6 % because of a reduction in open-circuit voltage, fill factor and short-circuit current density.

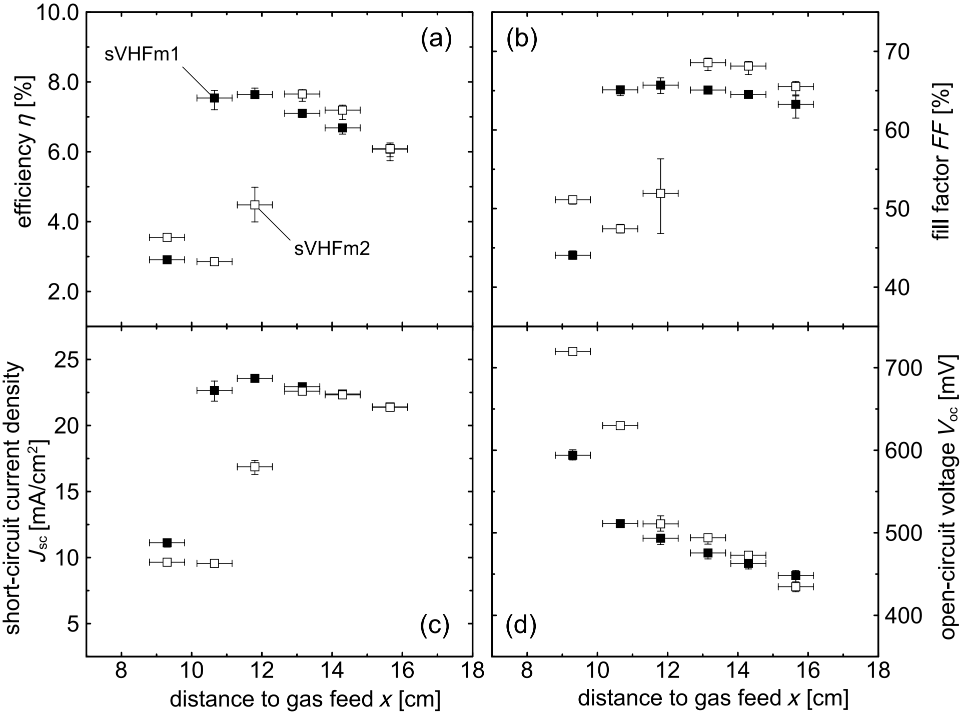

Figure 4.5: Efficiency η, open-circuit voltage V_{OC}, short-circuit current density J_{SC} and fill factor FF of μc-Si:H solar cells, depending on the distance to the gas feed x. The closed symbols represent solar cells with i-layers grown statically in regime sVHFm1, the open symbols represent regime sVHFm2.

The trends in the photovoltaic parameters indicate that the i-layer grows predominantly amorphous close to the gas feed and increases in crystallinity towards the exhaust (see section 4.1.1). Additional Raman measurements were carried out in order to investigate the crystallinity in more detail.

4.2.2 Local growth rate and crystallinity

The photovoltaic parameters shown in figure 4.5 indicate a change in the crystallinity from the gas feed towards the exhaust. Raman measurements were carried out in order to study the crystallinity at different positions. As shown in figure 4.6a the material is predominantly amorphous close to the gas feed and the crystallinity continuously increases towards the exhaust. A sudden change in crystallinity occurs close to the optimum phase mixture at $I_c^{RS} \approx 60$ %. As a consequence, the photovoltaic parameters change rapidly (see figure 4.5).

Assuming a continuous change in crystallinity it is apparent in figure 4.6a that the crystallinity of the i-layer changes within the area of one solar cell. Hence, the photovoltaic parameters of a solar cell can not be linked to a certain crystallinity because of the inhomogeneity of the i-layer across the solar cell area. Therefore, a corresponding error bar in crystallinity has to be incorporated if the photovoltaic parameters are plotted as a function of the crystallinity (see section 4.3).

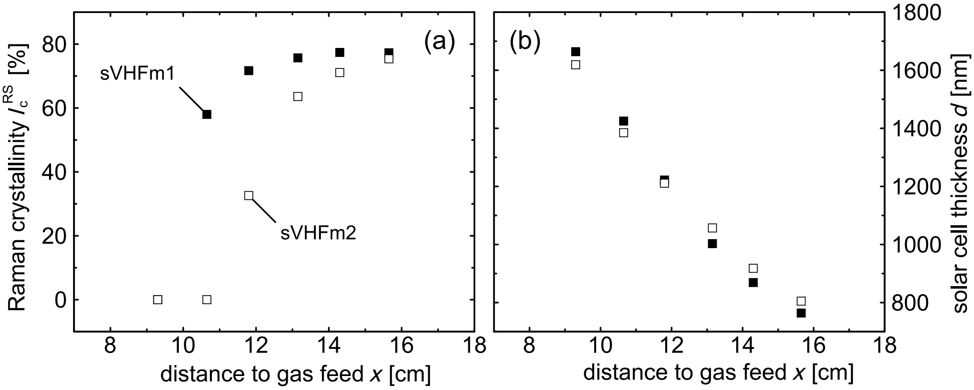

Figure 4.6: Raman crystallinity I_c^{RS} and solar cell thickness d, depending on the distance from the gas feed x. The closed symbols represent solar cells with i-layers grown statically in regime sVHFm1, the open symbols represent regime sVHFm2.

In figure 4.6b the solar cell thickness is displayed as a function of the distance to the gas feed. The thickness decreases from more than 1600 nm close to the gas feed to less than 800 nm towards the exhaust. This decrease is related to the reduction in silane concentration from the gas feed towards the exhaust. The number of growth precursors decreases with silane concentration leading to strong differences in the local deposition rate and film thickness.

In principle, the homogeneity can be improved by applying a regime with a low gas utilization which results in an almost constant silane concentration in gas flow direction [63]. However, the requirement of a low gas utilization for the linear plasma sources would be a drawback compared to the high gas utilization for static PECVD systems using showerhead electrodes. Therefore, it is not considered in this work.

4.2.3 Summary

It was shown that a linear gas distribution system and a high gas utilization leads to an inhomogeneous static deposition of μc-Si:H in terms of layer thickness and crystallinity. This inhomogeneity is due to the decreasing silane concentration from the gas feed towards the exhaust which results in a declining number of growth precursors in gas flow direction. This effect directly affects the growth rate and crystallinity of the material. As a consequence, the i-layer thickness, crystallinity and photovoltaic parameters depend on the position in front of the electrode.

In the subsequent section static RF- and VHF-PECVD regimes are compared in order to study the influence of the gas distribution system and deposition regime on the correlation between growth rate, crystallinity and the photovoltaic parameters.

4.3 Comparison of μc-Si:H solar cells deposited by static RF- and VHF-PECVD processes

In the present section solar cells with i-layers grown statically in regimes sVHFm1 and sVHFm2 (linear gas distribution - cross-flow geometry, 60 MHz) are compared to solar cells with i-layers grown in regime sRFm1 (showerhead electrode, 13.56 MHz). The aim is to study the influence of the deposition rate of the i-layer on the crystallinity and the photovoltaic parameters for different deposition regimes. The goal is to evaluate the material quality and identify effects related to the process parameters and the gas distribution system.

4.3.1 Influence of the crystallinity on the solar cell performance

Microcrystalline silicon solar cells have been deposited incorporating i-layers grown statically in regime sRFm1, sVHFm1 and sVHFm2. For all deposition regimes the crystallinity of the i-layer was varied by changing the silane concentration (from 0.6–1.2 %, 4.6–7.2 % and 1.2–2.2 % for sRFm1, sVHFm1 and sVHFm2, respectively). The i-layer thickness was kept constant within a deposition regime (1300–1400 nm for sRFm1 and 1000–1400 nm for sVHFm1 / sVHFm2) by adapting the deposition time to the growth rate of the i-layer in order to minimize thickness related effects. For details on the i-layer deposition regimes see appendix B.

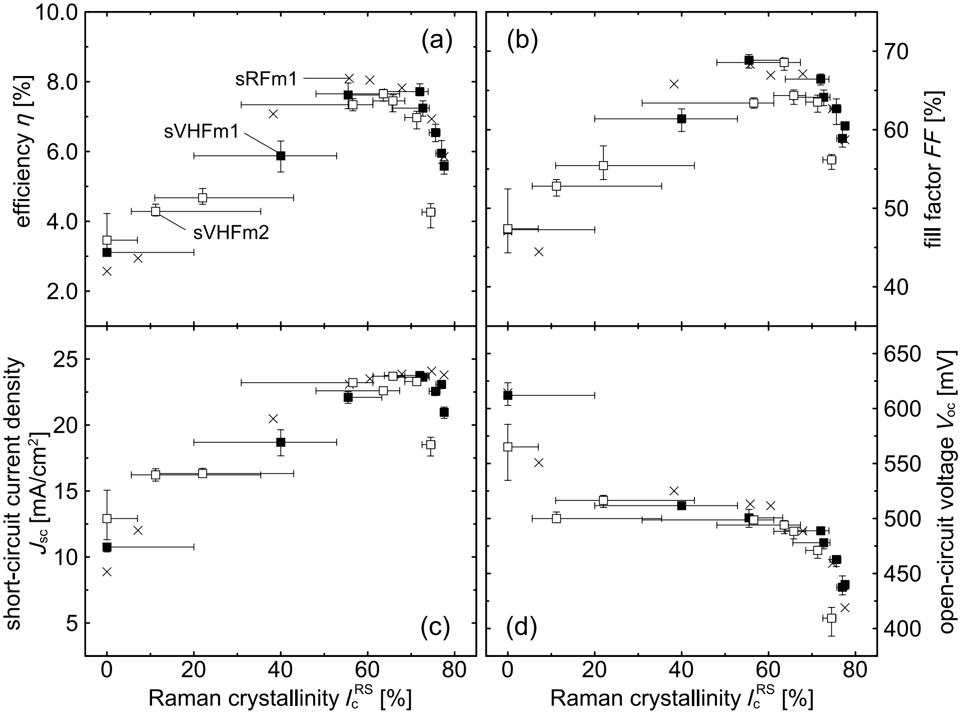

Figure 4.7: Efficiency η, open-circuit voltage V_{OC}, short-circuit current density J_{SC} and fill factor FF of μc-Si:H solar cells, depending on the Raman crystallinity I_c^{RS}. The closed squares represent solar cells with i-layers grown statically in regime sVHFm1, the open squares represent regime sVHFm2, the regime sRFm1 is represented by crosses.

Prior to the VHF-PECVD i-layer deposition process a 50 nm i-layer was deposited onto the p-layer using regime sRFm1 (showerhead electrode) and a silane concentration of 0.8 %. This was done in order to improve the homogeneity of the i-layers deposited statically by VHF-PECVD and to protect the p-layer from possible side effects (e.g. hydrogen etching). For the VHF regimes the results of the solar cells with a distance to the gas feed of 10.7 and 11.8 cm are shown (see section 4.2).

Figure 4.7 shows the photovoltaic parameters depending on the Raman crystallinity of the solar cells. The maximum efficiency for solar cells with i-layers grown in the VHF regimes using the cross-flow geometry is about 7.5–8 % at a Raman crystallinity of 55–70 % (see figure 4.7a). These values are comparable to the solar cells incorporating i-layers deposited in regime sRFm1 using a showerhead electrode. The small shift of the optimum in efficiency towards higher crystallinity for the VHF regimes may be related to the inhomogeneous crystallinity across the solar cells as indicated by the error bars.

The general trends in terms of efficiency, fill factor, short-circuit current density and open-circuit voltage are similar for the RF- and VHF regimes. However, there is a difference in the photovoltaic parameters at high crystallinity between solar cells with i-layers deposited at high growth rates (regime sVHFm2) and solar cells with i-layers grown at low growth rates (regimes sRFm1 and sVHFm1).

At a Raman crystallinity of about 75 % the photovoltaic parameters show a significant reduction for regime sVHFm2 compared to solar cells with i-layers grown in regime sVHFm1 or sRFm1. This finding indicates that the high deposition rate in regime sVHFm2 may lead to a reduced material quality for highly crystalline material.

In order to study the spectral response DSR measurements were carried out for some of the solar cells. The external quantum efficiency is shown in figure 4.8 for both VHF regimes at different crystallinities. The spectral response of the solar cells with optimum phase mixture ($I_c^{\mathrm{RS}} \approx 60$ %) and with very low crystallinity ($I_c^{\mathrm{RS}} \leq 10$ %) is similar to the results for regime sRFm1 shown in section 4.1.

In contrast, the solar cell with a highly crystalline i-layer grown at high deposition rate ($I_c^{\mathrm{RS}} = 75$ % in figure 4.8b) exhibits a reduced spectral response across the whole spectrum. The reduced spectral response is the cause for the lower short-circuit current density shown in figure 4.7c. Additionally, there is a strong bias voltage dependence which contributes to the low short-circuit current density. This finding is attributed to a poor charge carrier collection which indicates a high defect density of the i-layer.

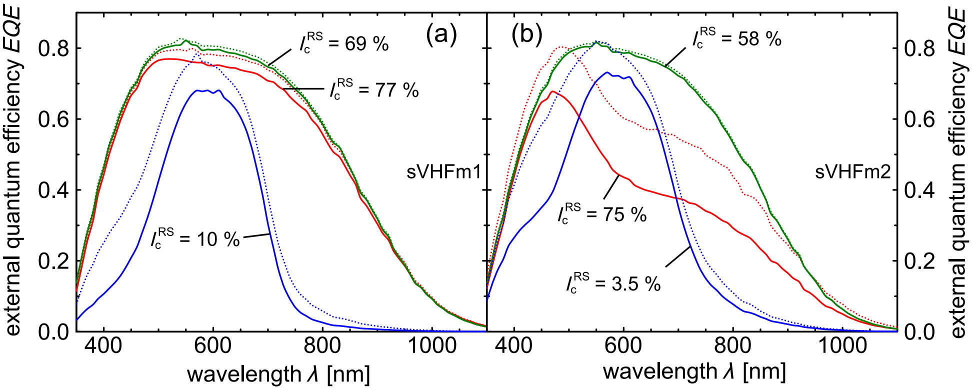

Figure 4.8: External quantum efficiency EQE of μc-Si:H solar cells, depending on the wavelength λ of the incident light for i-layers grown statically in a) regime sVHFm1 and b) regime sVHFm2. The EQE is displayed for a highly crystalline solar cell ($I_c^{RS} \geq 75$ %), a solar cell with a Raman crystallinity I_c^{RS} between 50–70 % and a solar cell with a very low crystallinity ($I_c^{RS} \leq 10$ %). The solid curves represent the EQE without bias voltage, the dotted curves represent the EQE at a bias voltage of -0.5 V.

4.3.2 Correlation between growth rate and crystallinity

In the previous section it was shown that the correlation between the crystallinity and the efficiency of μc-Si:H solar cells is very similar for the RF and VHF deposition regimes. It has been pointed out in section 4.1.2 that the crystallinity strongly depends on the growth rate of the μc-Si:H absorber layer for regime sRFm1. In the present section the correlation between growth rate and crystallinity is studied for regime sVHFm1 and sVHFm2 as well in order to identify effects related to the process parameters or gas distribution system.

The best solar cells are typically found at Raman crystallinities between 50–70 %. This range of crystallinities corresponds to a range of growth rates and silane concentrations as shown in section 4.1.2. In order to compare deposition regimes with different growth rates at the optimum phase mixture of $I_{c,opt}^{RS} = 60$ % a relative deposition rate r_{rel} is introduced. Within every deposition regime the deposition rate of an i-layer is compared to the deposition rate at the optimum phase mixture resulting in a relative deposition rate $r_{rel} = r/r(I_c^{RS} = 60\ \%)$. This relative deposition rate is now used to study the changes in crystallinity depending on the relative changes in the deposition rate.

In figure 4.9 the Raman crystallinity is plotted over the relative deposition rate of the bulk i-layer for the RF- and VHF regimes. The results show that the relative growth rate of the i-layer has to be between 0.85–1.05 in order to obtain a crystallinity of 50–70 %. Remarkably, there is little difference between the RF- and VHF regimes despite the differences in the process parameters and gas distribution system.

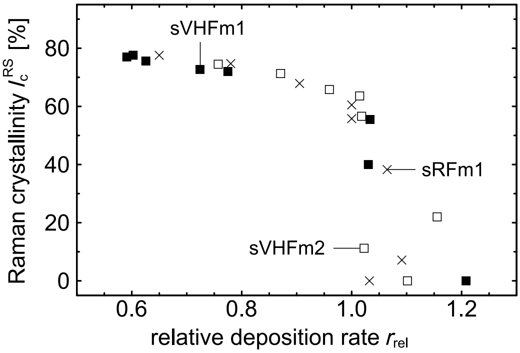

Figure 4.9: Raman crystallinity I_c^{RS} depending on the relative deposition rate r_{rel} for solar cells with i-layers grown statically in regime sVHFm1 (closed squares), regime sVHFm2 (open squares) and regime sRFm1 (crosses).

Deposition regimes sVHFm1 and sVHFm2 obtain a gas utilization of 40–65 %. Because of the cross-flow design at the linear plasma sources this means that the silane concentration decreases from the gas feed towards the exhaust by 40–65 % relative. The results in section 4.1 and refs. [17, 64] show that there is an almost linear dependence between the growth rate and silane concentration. It is therefore very likely that a similar correlation exists for the two VHF regimes. Hence, the strong change in silane concentration at high gas utilization leads to an inhomogeneous μc-Si:H layer growth for a linear gas distribution system and static deposition processes as shown in section 4.2.

4.3.3 Summary

It was shown that μc-Si:H solar cells incorporating i-layers grown statically in a RF- or VHF regime obtain the highest efficiency for a crystallinity of 50–70 %, independent of the gas distribution system or the chosen process parameters. State-of-the-art μc-Si:H solar cells were deposited incorporating i-layers grown statically by VHF-PECVD despite the strong inhomogeneity of the material properties due to the linear gas distribution system and high gas utilization (see table 4.3).

Table 4.3: Comparison of static deposition regimes for intrinsic μc-Si:H layers.

regime	frequency [MHz]	pressure [mbar]	power density [W/cm^2]	η_{gas} [%]	η_{opt} [%]	$I^{\text{RS}}_{\text{c,opt}}$ [%]	$r(I^{\text{RS}}_{\text{c,opt}})$ [nm/s]
sRFm1	13.56	12.5	0.33	60–65	8.1	61	0.53
sVHFm1	60	4	0.22	55–65	7.9	56	0.65
sVHFm2	60	6	0.52	40–50	7.8	64	1.0

Additionally, it was found that the correlation between crystallinity and deposition rate is very similar for regimes sRFm1, sVHFm1 and sVHFm2. Because of the interdependency between growth rate and silane concentration it is concluded that a deposition regime with high gas utilization always results in an inhomogeneous μc-Si:H layer growth in gas flow direction when using a linear gas distribution system.

In the subsequent section the influence of the deposition rate and thickness of the i-layer on the quality of the μc-Si:H solar cell is studied. The aim is to investigate the potential of reduced deposition times for the μc-Si:H absorber layer.

4.4 Reduced deposition times for μc-Si:H absorber layers

At the beginning of the present chapter it has been pointed out that the μc-Si:H absorber layer makes up for most of the thickness of the silicon layers in an a-Si:H/μc-Si:H tandem solar cell. Hence, the deposition rate of the μc-Si:H i-layer has a strong influence on the total deposition time of all silicon layers.

In the present section the influence of the deposition rate and thickness of the i-layer on the μc-Si:H solar cell efficiency is studied. The aim is to investigate the potential for reduced deposition times of the absorber layer using linear plasma sources and VHF-PECVD processes. The i-layers of the μc-Si:H solar cells were deposited statically using four different VHF-PECVD regimes, for details see table 4.4 and appendix B.

Table 4.4: Static VHF-PECVD regimes for intrinsic μc-Si:H layers grown at various deposition rates.

regime	pressure [mbar]	power density [W/cm^2]	silane concentration [%]	growth rates at $I_{\mathrm{c,opt}}^{\mathrm{RS}}$ [nm/s]
sVHFm1	4	0.22	4.6–7.2	0.54–0.7
sVHFm2	6	0.52	1.2–2.2	0.77-1.01
sVHFm3	7	0.69–0.94	2.2	1.11–1.39
sVHFm4	8	0.71–0.95	2.2	0.83–1.17

4.4.1 Correlation between growth rate and solar cell efficiency

In the previous sections the correlation between i-layer growth rate, crystallinity and photovoltaic parameters of μc-Si:H solar cells was studied. In contrast, the present section focuses on the influence of the deposition rate of the i-layer on the solar cell efficiency at optimum phase mixture ($I_{\mathrm{c}}^{\mathrm{RS}} \approx 60$ %).

Microcrystalline silicon solar cells have been deposited incorporating i-layers grown statically in deposition regimes sVHFm1–sVHFm4. Prior to the VHF-PECVD i-layer deposition process a 50 nm i-layer was deposited onto the p-layer using regime sRFm1 (showerhead electrode) and a silane concentration of 0.8 %. This was done in order to improve the homogeneity of the i-layers deposited statically by VHF-PECVD and to protect the p-layer from possible side effects (e.g. hydrogen etching).

Figure 4.10 shows the μc-Si:H solar cell efficiency for i-layers with an optimum phase mixture ($I_{\mathrm{c}}^{\mathrm{RS}} \approx 60$ %) as a function of the deposition rate and sorted by the VHF-PECVD regimes. The best solar cells obtain efficiencies close to 8 % for deposition rates up to 1.4 nm/s. The results in figure 4.10 indicate that the deposition rate of the bulk absorber layer has no negative impact on the efficiency of the μc-Si:H solar cells within the investigated range of growth rates when using a static VHF-PECVD process. This observation is in agreement with the findings in ref. [17].

The i-layer deposition rate of 1.36 nm/s at a solar cell efficiency of 7.7 % exceeds the best lab results for p–i–n μc-Si:H solar cells incorporating i-layers grown statically by RF-PECVD processes obtaining similar efficiencies by 0.5 nm/s [13]. This finding shows that the combination of linear plasma sources, VHF-PECVD and a linear gas distribution system is capable of producing high-quality μc-Si:H statically at higher deposition rates than conventional RF-PECVD systems using showerhead electrodes.

By increasing the deposition rate from 0.53 nm/s (regime sRFm1) to 1.4 nm/s (regime sVHFm3) the deposition time for a 1200 nm thick μc-Si:H absorber layer can be reduced from about 38 minutes to 14 minutes. The findings in [16, 18, 19] have shown that high-quality μc-Si:H solar cells can be deposited at i-layer growth rates exceeding 2 nm/s using VHF-PECVD processes. Hence, higher deposition rates than 1.4 nm/s may be possible for the linear plasma sources without compromising on the solar cell efficiency.

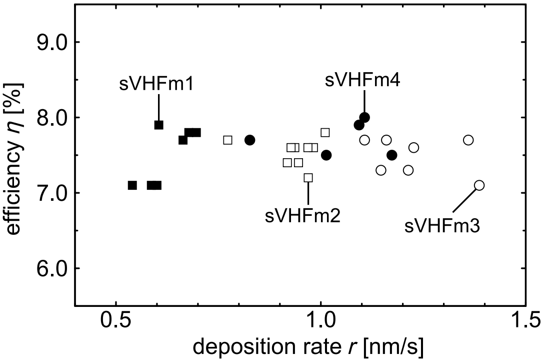

Figure 4.10: Efficiency η of μc-Si:H solar cells as a function of the deposition rate r of the i-layer. The results are sorted by the different static VHF-PECVD regimes described in table 4.4.

4.4.2 Influence of i-layer thickness on solar cell efficiency

In the previous section it was found that increasing the deposition rate of the i-layer has no negative influence on the efficiency of μc-Si:H solar cells. However, the deposition time of the absorber layer can also be reduced by using thinner i-layers.

In section 4.2 it was shown that the i-layer thickness is very inhomogeneous for static VHF-PECVD processes using the linear gas distribution system. Hence, μc-Si:H solar cells with varying i-layer thicknesses can be studied without carrying out additional deposition processes. In the present section μc-Si:H solar cells incorporating i-layers with an optimum phase mixture ($I_c^{RS} \approx 60$ %) and varying thicknesses deposited in regimes sVHFm1–sVHFm4 are studied. The results shown here are based on the deposition processes carried out for the μc-Si:H solar cells presented in the previous section.

Figure 4.11 shows the efficiency and short-circuit current density of μc-Si:H solar cells as a function of the absorber layer thickness and deposition regime. The short-circuit current density of the solar cells decreases from about 23.5 mA/cm^2 at an i-layer thickness of 1400 nm to 22 mA/cm^2 at 800 nm. However, the solar cell efficiency stays constant because of a rising fill factor and increasing open-circuit voltage towards thinner absorber layers. These findings are in agreement with the results published in [59, 65, 66].

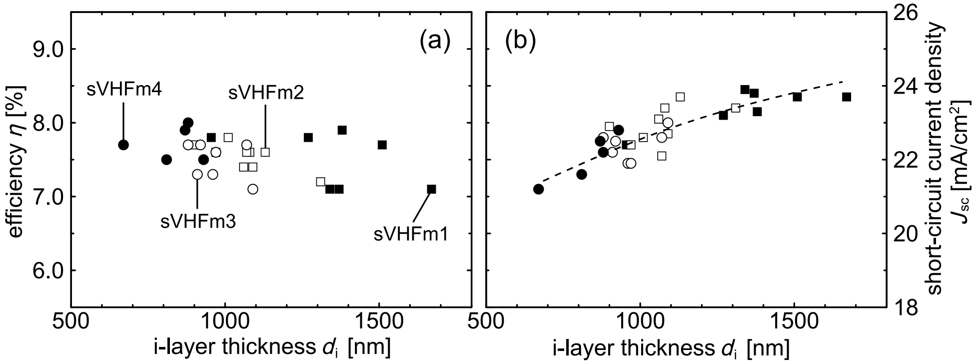

Figure 4.11: Efficiency η and short-circuit current density J_{SC} of μc-Si:H solar cells as a function of the i-layer thickness d_i of the solar cell. The results are sorted by the different static VHF-PECVD regimes described in table 4.4. The line is a guide to the eye.

State-of-the-art solar cells with an efficiency of 7.5–8 % are obtained at an i-layer thickness of only 900 nm using deposition regime sVHFm3. Hence, it is possible to deposit the i-layer of a μc-Si:H solar cell at a deposition rate of 1.4 nm/s statically within 11 minutes without compromising on the solar cell efficiency.

4.4.3 Summary

It was shown that the deposition time of statically deposited i-layers in high-quality μc-Si:H solar cells can be reduced by 60 % by increasing the deposition rate from 0.53 nm/s for RF-PECVD processes with a showerhead electrode to 1.4 nm/s for VHF-PECVD processes using linear plasma sources and a linear gas distribution system. This finding proves that the experimental setup developed in section 3.3 enables the static deposition of high-quality μc-Si:H absorber layers at high rates without compromising on the solar cell efficiency.

In the subsequent section the influence of a dynamic deposition process using linear plasma sources and a linear gas distribution system is studied in order to identify limitations due to the dynamic deposition process and the experimental setup.

4.5 Dynamic deposition of μc-Si:H absorber layers

In the previous section it was shown that μc-Si:H solar cells incorporating statically deposited i-layers grown in a VHF regime using linear plasma sources obtain state-of-the-art solar cell efficiencies for deposition rates up to 1.4 nm/s. However, the linear gas distribution system in combination with a high gas utilization leads to a decreasing silane concentration from the gas feed towards the exhaust (see section 4.2). Hence, the deposition conditions vary along the width of the electrode in gas flow direction.

The linear electrode design requires a dynamic deposition process in order to deposit homogeneously on the substrate area as discussed in section 3.1.2. The influence of the dynamic deposition on the photovoltaic parameters is studied in the present section. The aim is to investigate the correlation between growth rate, crystallinity and photovoltaic parameters of μc-Si:H solar cells with dynamically deposited i-layers and identify a possible influence of the dynamic deposition process in combination with the linear gas distribution system. For details on the dynamic deposition regimes for μc-Si:H i-layers see table 4.5 and appendix B.

Table 4.5: Dynamic VHF-PECVD regimes for intrinsic μc-Si:H layers.

regime	mode of operation	frequency [MHz]	pressure [mbar]	power density [W/cm^2]	gas utilization [%]
dfVHFm1	full oscillation	60	4	0.22	60
dfVHFm2	full oscillation	60	6	0.52	40
dsVHFm2	short oscillation	60	6	0.52	40

4.5.1 Influence of the dynamic deposition process on the solar cell performance

Microcrystalline silicon solar cells have been deposited incorporating i-layers grown statically (regime sVHFm1 and sVHFm2) and dynamically (regime dfVHFm1, dfVHFm2 and dsVHFm2) using linear plasma sources, VHF-PECVD processes and a linear gas distribution system. The crystallinity of the i-layer was varied for regimes sVHFm1 and sVHFm2 by changing the silane concentration from 4.6–7.2 % and 1.2–2.2 %, respectively.

Prior to the VHF-PECVD i-layer deposition process a 50 nm i-layer was deposited onto the p-layer using regime sRFm1 (showerhead electrode) and a silane concentration of 0.8 %. This was done in order to improve the homogeneity for statically deposited i-layers using VHF-PECVD processes and to protect the p/i interface from possible side effects (e.g. hydrogen etching). Additionally, the i-layer thickness of the μc-Si:H solar cells was kept between 1000–1400 nm in order to minimize thickness related effects.

In figure 4.12 the photovoltaic parameters of μc-Si:H solar cells are plotted as a function of the Raman crystallinity for different deposition regimes. The gray symbols represent solar cells with statically grown i-layers, red symbols represent solar cells with dynamically deposited i-layers. For dynamic deposition processes two modes of operation were applied.

Conventionally, the substrate carrier leaves the deposition zone during each pass of the linear plasma sources in a dynamic deposition process. The carrier therefore oscillations between $x = -50$ cm to $x = 50$ cm. This mode of operation is referred to as “full oscillation” (red circles, regimes dfVHFm1 and dfVHFm2). For the second mode of operation the carrier oscillates between $x = -15$ cm to $x = 15$ cm. Hence, the substrate carrier does not leave the deposition zone. This second mode is referred to as “short oscillation” (red squares, regime dsVHFm2).

It is shown in figure 4.12a that solar cells with i-layers grown dynamically in regime dfVHFm1 and dsVHFm2 obtain only slightly lower efficiencies than solar cells with i-layers grown statically at similar crystallinities. This finding is surprising considering the fact that the growth conditions on the substrate change considerably with time as it passes the electrode (see section 4.2).

For regime dfVHFm1 the crystallinity is lower than the optimum of 50–70 % which could be the cause for the lower short-circuit current density and the higher open-circuit voltage. Growing the i-layer at a lower silance concentration may lead to a more crystalline material, increasing the spectral response in the infrared part of the spectrum and thus, leading to a higher short-circuit current density (see section 4.3). As a result, the solar cell efficiency may increase to more than 7 % which would be comparable to μc-Si:H solar cells incorporating statically deposited i-layers at optimum phase mixture.

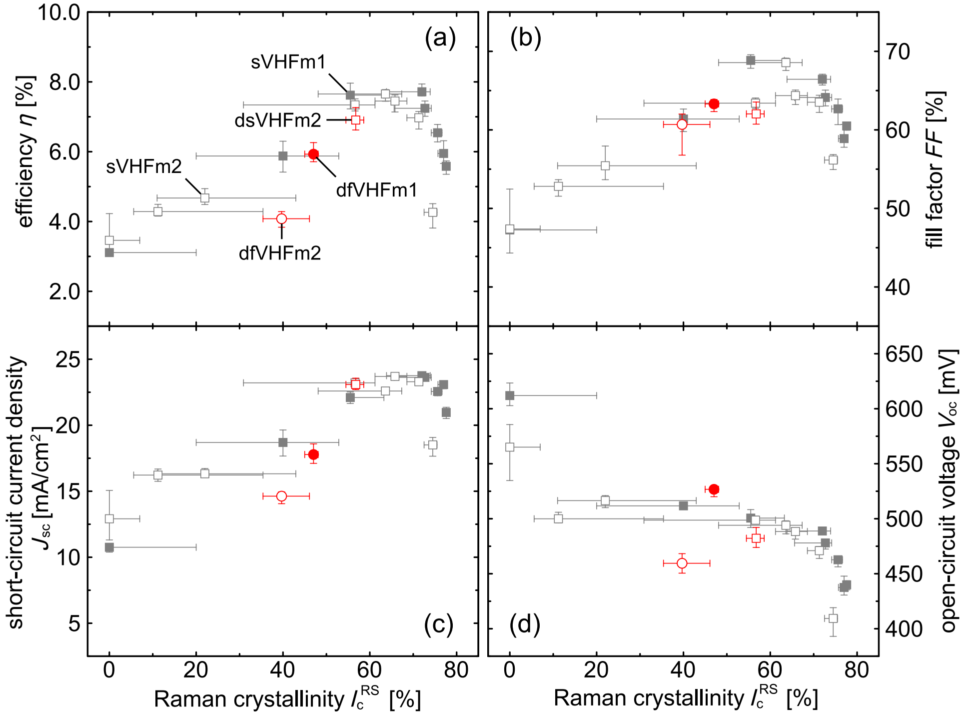

Figure 4.12: Efficiency η, open-circuit voltage V_{OC}, short-circuit current density J_{SC} and fill factor FF of μc-Si:H solar cells, depending on the Raman crystallinity $I_{\mathrm{c}}^{\mathrm{RS}}$. The gray symbols represent solar cells with statically grown i-layers (sVHFm1, sVHFm2), red symbols represent solar cells with dynamically grown i-layers (dfVHFm1, dfVHFm2, dsVHFm2). In regimes dfVHFm1 and dfVHFm2 the carrier oscillates from $x = -50$ cm to $x = 50$ cm. In regime dsVHFm2 the carrier oscillates from $x = -15$ cm to $x = 15$ cm.

Solar cells incorporating i-layers grown in regime dfVHFm2 obtain an efficiency of 4 %. The fill factor of 60 % is typical for the crystallinity of 40 % (see figure 4.12b), but short-circuit current density and open-circuit voltage are lower than for solar cells incorporating statically deposited i-layers at the same crystallinity. A higher crystallinity of the i-layer is expected to lead to a higher short-circuit current density due to a higher spectral response in the infrared part of the spectrum but is likely to cause a further reduction in the open-circuit voltage. Hence, reducing the silane concentration to obtain a more crystalline i-layer may not result in a state-of-the-art solar cell efficiency.

The results in figure 4.12 show that μc-Si:H solar cells with i-layers grown dynamically in regime dsVHFm2 obtain an efficiency of up to 7.3 %. This value is only slightly lower than for solar cells with statically grown i-layers using a similar deposition regime. This finding indicates that the changing growth conditions during the dynamic deposition process may have an influence on the μc-Si:H solar cell efficiency. In the subsequent section possible side effects of the dynamic deposition process are identified.

4.5.2 Sources of reduced layer quality in dynamic deposition processes

In the previous section it was shown that μc-Si:H solar cells incorporating dynamically grown i-layers obtain slightly lower efficiencies than solar cells with statically grown i-layers using a similar deposition regime. In the present section differences between static and dynamic deposition processes are identified.

Changing deposition conditions

The solar cell results in section 4.2 indicate that the local growth conditions strongly depend on the substrate position in front of the electrode. Hence, a fixed point on the substrate is exposed to a variety of growth conditions during a dynamic deposition process.

The silane concentration changes from the gas feed towards the exhaust because of the cross-flow design (see section 3.3.4). The magnitude of the decrease is directly related to the gas utilization. Hence, the gas utilization determines the inhomogeneity of the silane concentration across the width of the electrode (i.e. in gas flow direction).

Additionally, the electric field is not perfectly homogeneous across the electrode. The electric field is stronger at the edges of the electrode, leading to a higher plasma density. This effect may result in locally higher deposition rates as shown in [63].

Changes in gas composition and plasma density have a significant impact on material growth. The growth conditions may change from amorphous to microcrystalline within the width of the electrode (see section 4.2). Nevertheless, the results in figure 4.12 show that reasonable solar cell efficiencies are obtained despite the repeated alternation of changing plasma conditions during a dynamic deposition process.

i-layer contamination

The contamination of intrinsic μc-Si:H layers is another possible cause for a reduced solar cell efficiency [67]. It has been shown that the solar cell efficiency decreases if the contamination of the i-layer with oxygen or nitrogen exceeds a critical level [68]. This critical level depends on the contaminant, but also on the deposition regime [69].

Static VHF-PECVD processes are comparable to static RF-PECVD processes when considering the origin of contamination [70]. The contaminants can either enter the chamber with the source gas (gas pipe leak or impurity of source gas) or diffuse from the chamber walls into the deposition zone (chamber wall leak). However, in the latter case the contaminants have to overcome the resistance of the permanent gas flow across the substrate and towards the exhaust in order to enter the plasma zone.

The conditions are different for a dynamic deposition process where the substrate carrier leaves the deposition zone frequently. As a result, contaminants from the chamber walls may have a higher chance to adhere to the surface of the growing film while the substrate is outside the plasma. The contamination level may increase, which could have a negative impact on the i-layer properties and thus, on the solar cell efficiency [68, 69].

Powder incorporation

Another cause for a lower material quality can be the incorporation of powder into the i-layer. Powder formation typically occurs due to polymerization of negatively charged ions in the plasma bulk [71]. These negative ions can not escape the plasma bulk due to the negative potential of the electrodes. Hence, the powder is typically transported away from the plasma zone with the gas flow.

In the present work powder accumulation has been observed close to the exhaust on the carrier and electrode for the static RF- and VHF-PECVD processes. However, in static deposition processes the powder is not incorporated into the i-layer because the substrate stays in front of the electrode. Hence, the i-layer quality is not affected.

In case of a dynamic deposition process the substrates pass by the region of powder deposition. Hence, powder may be incorporated into dynamically grown i-layers, reducing the material quality. The incorporation of a thin layer of powder may lead to an interruption of the microcrystalline growth.

The formation of powder depends on the pressure, electrode distance, power level, temperature and gas residence time [72–74]. It has been shown that the onset of powder formation shifts to higher pressures for narrower electrode distances [74]. This finding indicates that it is possible to reduce the powder formation at a given pressure by reducing the electrode distance. A narrow electrode distance may also facilitate deposition rates of more than 2 nm/s as demonstrated in [18, 19].

4.5.3 Influence of the dynamic deposition processes on the transition from microcrystalline to amorphous layer growth

In section 4.5.1 it was shown that the efficiency of μc-Si:H solar cells is affected by the changing i-layer growth conditions during a dynamic deposition process. In the present section the influence of dynamic deposition processes on the transition from microcrystalline to amorphous layer growth is studied. Therefore, the correlation between the growth rate of the i-layer and the crystallinity is investigated for μc-Si:H solar cells with statically and dynamically deposited i-layers which were presented in section 4.5.1.

Figure 4.13 shows the Raman crystallinity as a function of the deposition rate and deposition regime of the i-layer. For dynamic deposition processes the average growth rate is calculated according to equation 3.1. The crystallinity of an i-layer deposited dynamically with full oscillation (regimes dfVHFm1 and dfVHFm2) is significantly lower than for a corresponding statically deposited i-layer at the same deposition rate (regimes sVHFm1 and sVHFm2). In contrast, the i-layer grown dynamically with short oscillation (regime dsVHFm2) has a similar crystallinity as a corresponding statically deposited i-layer at the same deposition rate (regime sVHFm2).

The difference between the i-layer deposition processes in regime dfVHFm2 and dsVHFm2 is the length of the path the carrier travels between the points where it switches the movement direction. In regime dfVHFm2 the carrier oscillates between $x = -50$ cm to $x = 50$ cm while it oscillates between $x = -15$ cm to $x = 15$ cm for regime dsVHFm2. As a result, the substrates encounter the same deposition conditions along the electrodes except for the region close to the exhaust. It is therefore concluded that the changing silane concentrations encountered by the substrate may not be the sole cause for the reduced crystallinity at a given deposition rate.

In section 4.5.2 it was mentioned that there are two other factors that may influence the quality of μc-Si:H material in a dynamic deposition process: an increasing contamination level and the incorporation of powder. The results published in ref. [75] indicate that a very high contamination level with oxygen (10^{20} cm^{-3}) may lead to a reduced crystallinity of the μc-Si:H layer. However, the incorporation of a thin layer of powder is very likely inhibiting the microcrystalline growth as well. Therefore, both effects may contribute to the reduced crystallinity for dynamically grown i-layers deposited with full oscillation.

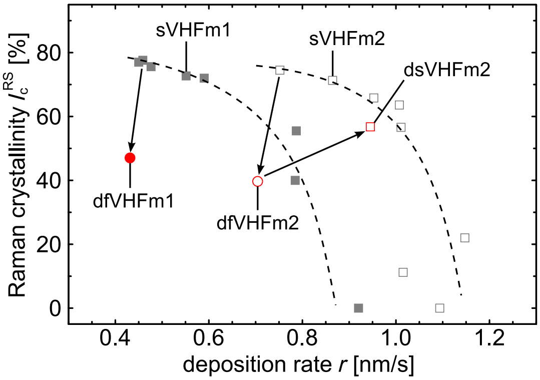

Figure 4.13: Raman crystallinity I_c^{RS} depending on the deposition rate of the i-layers for static deposition processes (gray symbols, regime sVHFm1 and sVHFm2) and dynamic deposition processes (red symbols, regimes dfVHFm1, dfVHFm2 and dsVHFm2). In regimes dfVHFm1 and dfVHFm2 the carrier oscillates from $x = -50$ cm to $x = 50$ cm. In regime dsVHFm2 the carrier oscillates from $x = -15$ cm to $x = 15$ cm. Lines are guides to the eye.

In section 4.6 the influence of changing silane concentrations encountered by a substrate during a dynamic deposition process is studied using a static deposition process and applying a time-dependent silane concentration. The aim is to investigate the effects on the photovoltaic parameters and material growth systematically.

4.5.4 Homogeneity of dynamic deposition process

It was found in section 4.3 that the efficiency of μc-Si:H solar cells strongly depends on the crystallinity of the i-layer and that the best solar cells are typically found for a crystallinity of 50–70 %. Because of the monolithic interconnection of solar cells in a solar module the local changes in the photovoltaic parameters may have a negative influence on the efficiency of the whole solar module. Hence, it is important for a large area processes to guarantee that the i-layer grows homogeneously in terms of crystallinity and film thickness in both substrate dimensions.

Raman measurements on the solar cells incorporating an i-layer grown dynamically in regime dsVHFm2 showed a crystallinity of 53-61 %. The homogeneity in terms of i-layer thickness was in the order of ±10 %. These findings prove that dynamic deposition processes using linear plasma sources in combination with a linear gas distribution system enables the homogeneous high-rate deposition of μc-Si:H layers.

4.5.5 Summary

It has been shown that solar cells incorporating dynamically deposited μc-Si:H absorber layer exhibit a slightly lower efficiency than solar cells with statically grown i-layers deposited in the same regime. This effect may be related to the changing silane concentrations throughout the dynamic deposition process.

The crystallinity of the i-layer appears to be reduced for a dynamic deposition process compared to static deposition processes at a given (average) growth rate. The results indicate that this effect is probably not caused by the changing silane concentrations but the incorporation of powder or an increasing contamination level of the i-layer.

For the investigated dynamic deposition processes the homogeneity in terms of film thickness and crystallinity was in the order of ±10 % (relative). This finding proves that the combination of VHF-PECVD with linear plasma sources and a linear gas distribution system enables the up-scaling of high-rate μc-Si:H VHF processes in a homogenous way.

4.6 Effects of changing silane concentrations during i-layer growth on μc-Si:H solar cells

In the previous section it was shown that the dynamic deposition process of a μc-Si:H absorber layer has an influence on the solar cell efficiency. This effect may be related to the inhomogeneity of deposition conditions in gas flow direction which is caused by the decreasing silane concentration from the gas feed towards the exhaust (see section 4.2).

In the present section the effect of changing silane concentrations encountered by a substrate during a dynamic i-layer deposition process is studied systematically by using a static deposition process and applying a time-dependent silane concentration [76]. This approach gives the possibility to investigate the influence of different process parameters independently.

4.6.1 Variation in growth conditions due to dynamic deposition processes

In the subsequent sections the results of μc-Si:H solar cells incorporating i-layers grown statically with a time-dependent silane concentrations are presented. In the present section the correlation between this setup and a dynamic deposition process using a linear gas distribution system is shown.

Figure 4.14 displays the exemplary time-dependent silane concentration in a dynamic deposition process using a linear gas distribution system for a fixed point on the substrate. For simplicity, the times outside the plasma have been left out because no material is deposited. Additionally, the oscillation is approximated by a triangular shape even though the exact shape depends on the process parameters.

In a dynamic deposition process using the configuration presented in section 2.2.3 the substrates enter the plasma close the exhaust of the first linear plasma source where the silane concentration is SC_{out}. As the substrates move towards the gas feed the silane concentration increases until it reaches SC_{in} (see figure 4.14). The silane concentration then decreases again to SC_{out} as the substrates pass the plasma zone of the second linear plasma source towards the exhaust. After one cycle is completed, the substrate changes movement direction and the next cycle begins.

There are two parameters that are deduced for a simplified model: the amplitude of change in silane concentration A and the period T of a deposition cycle. The first parameter that describes the dynamic deposition process is the amplitude of change in silane concentration. This parameter is used to derive the gas utilization as follows

$$\eta_{\text{gas}} = \frac{SC_{\text{in}} - SC_{\text{out}}}{SC_{\text{in}}} = \frac{2A/\overline{SC}}{1 + A/\overline{SC}}, \tag{4.1}$$

with $\overline{SC}$ being the mean silane concentration. This equation can be simplified by defining a relative amplitude $A_{\text{rel}} = A/\overline{SC}$ to

$$\eta_{\text{gas}} = \frac{2A_{\text{rel}}}{1 + A_{\text{rel}}}. \tag{4.2}$$

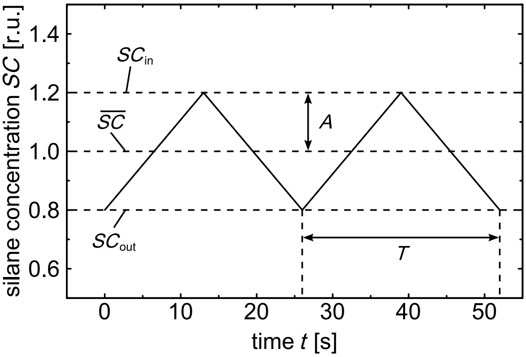

Figure 4.14: Silane concentration SC depending on the time t for a fixed point on the substrate in a dynamic deposition process. Note, that the times of no deposition (between the electrodes and outside the deposition area) have been left out for an easier understanding of the basic principles.

Hence, a certain gas utilization in a dynamic deposition process using the linear plasma sources may be studied with a static deposition process that employs an oscillating silane concentration around a median $\overline{SC}$ with a relative amplitude A_{rel}.

The second parameter that describes the dynamic deposition process is the period T of a deposition cycle. This period depends on the carrier speed v and the total width of the electrodes w as

$$T = \frac{w}{v}. \tag{4.3}$$

In the present work the width of the electrodes (2 × 20 cm) and the carrier velocity (15 mm/s) are kept constant, resulting in a period of about 27 seconds for a dynamic deposition process with full oscillation (see section 4.5.1). However, the layer thickness d_{T} deposited during each period changes with the average deposition rate $\overline{r}$ as

$$d_{\mathrm{T}} = \overline{r}T. \tag{4.4}$$

Accordingly, varying average deposition rates for dynamic deposition processes may be studied by varying the period of the oscillation in silane concentrations for a static deposition process with a given deposition rate in order to obtain the same thickness per period. However, it should be pointed out that this model neglects any plasma inhomogeneities along the electrode width and is therefore an approximation of the real parameter variations. In the subsequent sections the influence of the gas utilization and thickness per period are studied systematically under these assumptions.

4.6.2 Influence of the gas utilization on μc-Si:H solar cells

In the previous section it was pointed out that the changing silane concentrations during a dynamic deposition process may be studied using a static deposition process and applying a time-dependent silane concentration. Additionally, it was shown that the gas utilization of a dynamic deposition process is related to the amplitude of change in silane concentration applied during the static deposition process.

In the present section different levels of gas utilization for a dynamic deposition process are studied by applying different relative amplitudes of change in silane concentration to a static i-layer deposition process. Microcrystalline silicon solar cells are deposited incorporating i-layers grown statically in regime sRFm1 (see section 4.1) but applying an oscillating silane concentration during i-layer growth according to the previous section. The period T of the oscillation is adapted to the average growth rate in order to obtain a constant thickness per period d_T of 83 nm and a constant i-layer thickness of 1300 nm.

Figure 4.15 displays the photovoltaic parameters depending on the gas utilization η_gas in the initial state and for some solar cells also after light-induced degradation. The solar cells with i-layers grown at a constant silane concentration (corresponds to $\eta_\mathrm{gas} \to 0$) obtain an efficiency of about 7.6 % and are not prone to light-induced degradation.

To investigate the influence of the gas utilization the silane concentration at the optimum phase mixture ($I_\mathrm{c}^\mathrm{RS} \approx 60$ %) from section 4.1 was used as mean silane concentration (squares) and different amplitudes of change in silane concentration were applied. The solar cell efficiency remains almost constant up to a gas utilization of 40 % according to equation 4.2 but drops sharply for higher levels of gas utilization. Two vertical lines in figure 4.15a indicate the level of gas utilization for regimes dfVHFm1 and dfVHFm2.

The reduced efficiency is caused by a lower short-circuit current density and a lower fill factor. Both trends and the rising open-circuit voltage indicate a decreasing crystallinity of the i-layer which was confirmed by Raman measurements. This finding indicates that for a given mean silane concentration the material grows at a lower crystallinity with increasing amplitudes of change in silane concentration (higher gas utilization).

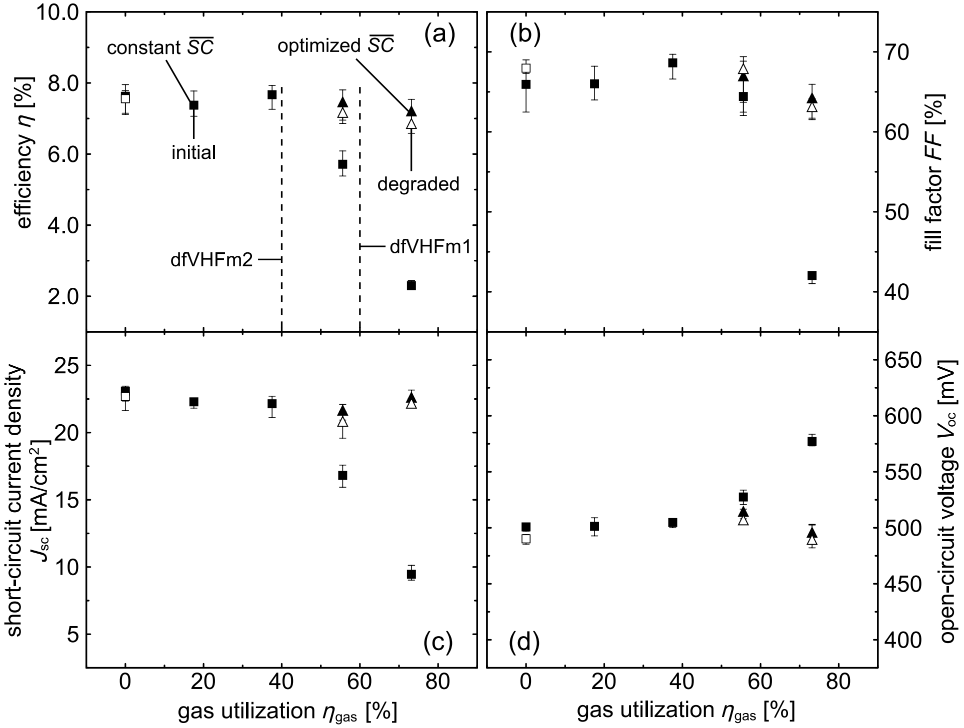

Figure 4.15: Efficiency η, open-circuit voltage V_{OC}, short-circuit current density J_{SC} and fill factor FF of μc-Si:H solar cells as a function of the gas utilization η_{gas} for a fixed thickness per period d_T of 83 nm. The photovoltaic parameters are displayed before degradation (closed symbols) and after degradation (open symbols) for i-layers grown with a fixed mean silane concentration (squares) and an optimized mean silane concentration (triangles).

Next, the crystallinity of the i-layer was optimized by reducing the mean silane concentration for the i-layer deposition while keeping the gas utilization constant. The solar cells with optimized mean silane concentration are represented by triangles in figure 4.15. The efficiency of the solar cells incorporating an i-layer deposited at a gas utilization of about 73 % increases from 2.3 % to 7.2 % by reducing the mean silane concentration from 1.06 % to 0.89 %. Hence, solar cells with i-layers grown with large variations in the silane concentration and growth conditions can still obtain reasonable efficiencies.

The solar cells incorporating i-layers grown with large variations in the silane concentration show a stronger degradation effect than the solar cells with i-layers grown at a constant silane concentration (see figure 4.15a). This finding may indicate that the amorphous fraction of i-layers grown with large variations in the silane concentration leads to a deterioration of the material properties during light soaking. Hence, the changes in silane concentration (gas utilization) may have to be limited to a certain level in order to avoid a negative influence on the solar cell efficiency.

The average growth rate at the optimum phase mixture was between 0.51-0.54 nm/s for all processes with a gas utilization lower than 60 % according to equation 4.2. For deposition processes applying a change in silane concentration corresponding to a gas utilization of 73 %, the average growth rate of the i-layer dropped to 0.43 nm/s. It is therefore concluded that high levels of gas utilization may have an impact on the average growth rate at optimum phase mixture in a dynamic deposition process using a linear gas distribution system.

4.6.3 Influence of the thickness per period on μc-Si:H solar cells

In section 4.6.1 it was shown that the changing silane concentrations throughout a dynamic deposition process may be studied using a static deposition process and applying a time-dependent silane concentration. In the previous section the influence of the gas utilization on the solar cell efficiency was investigated. Now, the influence of different i-layer deposition rates in dynamic deposition processes is studied by applying different thicknesses per period to a static deposition process with a time-dependent silane concentration.

The μc-Si:H solar cells presented in the present section incorporate i-layers deposited statically in regime sRFm1 (see section 4.1) but applying an oscillating silane concentration according to section 4.6.1. Different thicknesses per period d_{T} are studied by changing the period T of the oscillation while keeping the gas utilization according to equation 4.2 at 56 % and the i-layer thickness at about 1300 nm.

Figure 4.16 shows the correlation between the photovoltaic parameters and the thickness per period in the initial state (closed symbols) and after light-induced degradation (open symbols). The thickness per period was first varied using the silane concentration at the optimum phase mixture ($I_{\mathrm{c}}^{\mathrm{RS}} \approx 60$ %) from section 4.1 as mean silane concentration (squares). The efficiency decreases with an increasing thickness per period due to a reduction in the short-circuit current density (see figure 4.16a,b). The crystallinity as determined from the Raman measurement shows a reduction of I_c^{RS} to about 20–30 % at thicknesses per period of more than 20 nm.

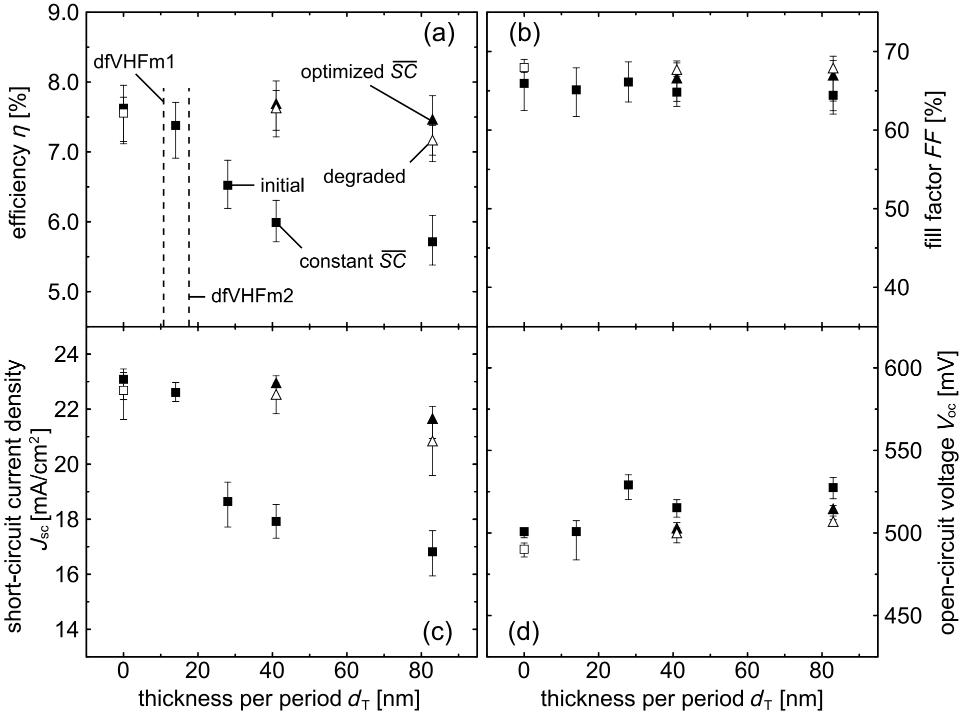

Figure 4.16: Efficiency η, open-circuit voltage V_{OC}, short-circuit current density J_{SC} and fill factor FF of μc-Si:H solar cells as a function of the thickness per period d_T for a fixed gas utilization η_{gas} of 56 %. The photovoltaic parameters are displayed before degradation (closed symbols) and after degradation (open symbols) for i-layers grown with a fixed mean silane concentration (squares) and an optimized silane concentration (triangles).

Next, the crystallinity of the i-layer was optimized by reducing the mean silane concentration for the i-layer deposition while keeping the thickness per period and the relative amplitude constant. The solar cells with optimized mean silane concentration are represented by triangles in figure 4.16.

Figure 4.16a shows that the efficiency of the solar cells with optimum phase mixture is comparable to the solar cells with an i-layer grown at a constant silane concentration ($d_{\mathrm{T}} = 0$ nm). However, at a thickness per period of 83 nm the solar cells degrade during light soaking by about 0.3 % absolute. Hence, the thickness per period should be limited to about 40 nm at a gas utilization of 56 %. For the given electrode dimension and carrier velocity this would correspond to an average growth rate $\overline{r}$ of about 1.5 nm/s. For comparison the thickness per period for regimes dfVHFm1 and dfVHFm2 is indicated by vertical lines in figure 4.16a.

4.6.4 Summary

It was shown that significant changes in silane concentration encountered by a substrate during a static deposition process can be tolerated without a negative impact on the μc-Si:H solar cell efficiency. These results indicate that high-quality μc-Si:H solar cells can be deposited despite the changing growth conditions encountered by a substrate during a dynamic deposition process.

Additionally, it was observed that the average growth rate at optimum phase mixture ($I_{\mathrm{c}}^{\mathrm{RS}} \approx 60$ %) was only affected by changing silane concentrations at a gas utilization of more than 70 % according to equation 4.2. For lower gas utilizations the average growth rate of the optimized layer stayed within 0.51–0.54 nm/s which is comparable to the process with constant silane concentration in regime sRFm1 (see section 4.1).

This finding could be an indication that the difference in the crystallinity for static and dynamic deposition processes at a given deposition rate found in section 4.5.3 is only partially related to the changing silane concentrations encountered by the substrate during a dynamic deposition process.

4.7 Conclusions

In the present chapter a scalable dynamic VHF-PECVD technique for the growth of μc-Si:H was investigated. First, the influence of the crystallinity on the photovoltaic parameters was studied for a static RF-PECVD regime using a showerhead electrode and static VHF-PECVD regimes using a linear gas distribution system. It was found that solar cells with i-layers grown statically by VHF-PECVD show a similar correlation between the i-layer growth rate, Raman crystallinity and the photovoltaic parameters as solar cells with i-layers grown by RF-PECVD.

Microcrystalline silicon solar cells with i-layers deposited statically by VHF-PECVD obtain efficiencies of 7.5–8 % at deposition rates up to 1.4 nm/s. This growth rate is a significant improvement compared to the 0.53 nm/s for the state-of-the-art RF-PECVD process, proving the capability of the linear plasma sources to deposit high-quality intrinsic μc-Si:H at high growth rates.

It was pointed out that the static VHF-PECVD process using a linear gas distribution system leads to an inhomogeneous layer growth in terms of deposition rate and crystallinity at high gas utilization. As a consequence, i-layers grown dynamically encounter changing growth conditions throughout the deposition process. Solar cells with dynamically deposited i-layers obtain efficiencies of about 7.3 % at a deposition rate of 0.95 nm/s. It was found that the changing silane concentrations during dynamic deposition processes may lead to a small reduction of the efficiency compared to solar cells with i-layers grown statically at a similar deposition rate and crystallinity.

A static RF-PECVD process with an oscillating silane concentration was applied in order to study the effect of varying silane concentrations during dynamic VHF-PECVD processes. The results indicate that the solar cell performance deteriorates with increasing amplitude of change in silane concentration (gas utilization) and increasing thickness per period (growth rate). The results also show that very small changes in the silane concentration during i-layer growth (e.g. a gas utilization of less than 20 %) do not lead to a deterioration of the solar cell efficiency, compared to solar cells with i-layers grown at a constant silane concentration.

The homogeneity of the dynamic deposition process in terms of deposition rate and Raman crystallinity was in the order of ±10 % (relative). This finding proves that the experimental setup developed in section 3.3 combines high deposition rates and good uniformity for the growth of microcrystalline silicon.

Some solar cells with dynamically deposited i-layers obtained significantly lower efficiencies than solar cells with i-layers grown statically at the same crystallinity. The cause of the reduced solar cell performance is not yet fully understood but there are two possible explanations. First, the i-layer leaves the deposition zone during the dynamic deposition process which could lead to an enhanced contamination compared to a static deposition process. Secondly, powder formation occurs for some process conditions. The incorporation of this powder into the i-layer may lower the material quality and lead to a lower solar cell efficiency.

5 Dynamic deposition of a-Si:H solar cells

In the previous chapter it was shown that μc-Si:H solar cells incorporating absorber layers grown statically using VHF-PECVD processes in combination with linear plasma sources obtain state-of-the-art efficiencies for deposition rates up to 1.4 nm/s. It was found that the deposition rate itself has no influence on the solar cell performance within the investigated range of growth rates. However, the results showed that a dynamic deposition process of the absorber layer has a small negative influence on the solar cell performance.

In the present chapter dynamic VHF-PECVD processes using linear plasma sources for the deposition of a-Si:H absorber layers are developed. The influence of the deposition rate on the i-layer properties, solar cell performance and degradation behavior of the a-Si:H solar cells is studied.

In an a-Si:H/μc-Si:H tandem solar cell the a-Si:H top cell delivers roughly two thirds of the total power because of its significantly higher open-circuit voltage compared to the μc-Si:H bottom cell. Hence, the efficiency of an a-Si:H/μc-Si:H tandem solar cell strongly depends on the performance of the a-Si:H top cell. It is therefore the aim of the present chapter to assess the potential of a dynamic deposition process for the deposition of state-of-the-art a-Si:H solar cells incorporating i-layers grown at high rates.

5.1 Influence of the deposition rate on the i-layer properties

In the present section the influence of the deposition rate on the i-layer properties is studied. A moderate deposition temperature of 180°C is chosen because it was demonstrated that high deposition temperatures of the i-layer lead to a deterioration of the p/i interface in p–i–n a-Si:H solar cells [77, 78]. The a-Si:H i-layers are deposited statically using a showerhead electrode and RF-PECVD processes or dynamically using linear plasma sources and VHF-PECVD processes. Within a deposition regime only one process parameter is changed at a time. A short summary of the deposition regimes is given in table 5.1, for more details see appendix C.

Table 5.1: Deposition regimes for the growth of intrinsic a-Si:H layers.

regime	mode	frequency [MHz]	power density [mW/cm^2]	silane concentration [%]	total gas flow [sccm]
sRFa1	static	13.56	21–94	12.4	395
sRFa2	static	13.56	33	4.6–25.3	580
dfVHFa1	dynamic	60	34–107	28.5	525
dfVHFa2	dynamic	60	53	11–41.6	445

5.1.1 Hydrogen incorporation

The incorporation of hydrogen plays a crucial role for the quality of a-Si:H layers because the hydrogen atoms passivate dangling bonds in the a-Si:H network that would otherwise serve as recombination centers for photo-generated charge carriers. Therefore, in the present section the amount of hydrogen and its bonding configuration is studied by analyzing the FTIR spectra of a-Si:H i-layers according to section 2.5.4.

Figure 5.1 shows the atomic hydrogen concentration and microstructure factor of the a-Si:H layers depending on the deposition rate. The deposition rate of the i-layer is varied by changing the power density (21–94 mW/cm^2 for sRFa1 and 34–107 mW/cm^2 for dfVHFa1) or changing the silane concentration (4.6–25.3 % for sRFa2 and 11–41.6 % for dfVHFa2) separately while keeping the other process parameters constant.

The atomic hydrogen concentration of the i-layer increases from 15 % at a deposition rate of 0.2 nm/s to 18 % at 1 nm/s (see figure 5.1a). The results indicate that the hydrogen concentration most notably depends on the deposition rate and not as much on the process parameter that is changed. This finding is remarkable because the power densities and silane concentrations change within a deposition regime by a factor of 3–5.

The microstructure factor as shown in figure 5.1b does not change with increasing power densities (squares). In contrast, the microstructure factor increases with silane concentration for both excitation frequencies (triangles). The latter effect is in agreements with the results published in ref. [79]. The increase in the microstructure factor indicates that the material becomes more porous when grown at high silane concentrations.

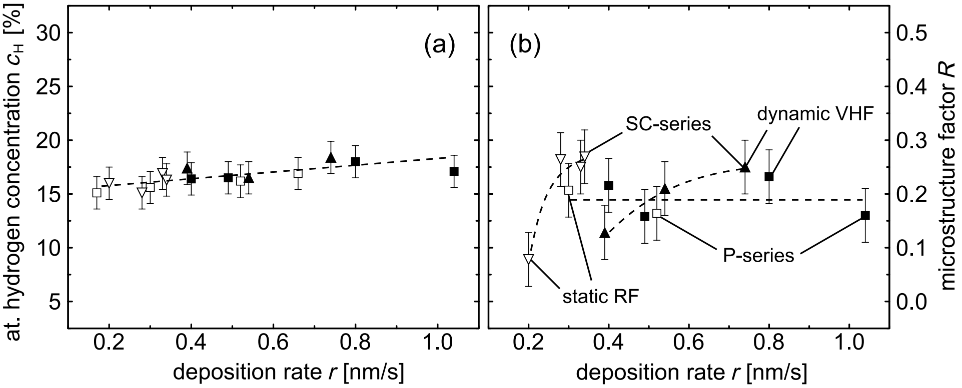

Figure 5.1: Atomic hydrogen concentration c_H and microstructure factor R as a function of the deposition rate r of the i-layer. Closed symbols represent i-layers grown dynamically by VHF-PECVD, open symbols represent i-layers grown statically by RF-PECVD. Layers deposited at different power densities are marked with squares, layers deposited at different silane concentrations are marked with triangles. Dashed lines are guides to the eye.

The increasing hydrogen concentration with deposition rate can intuitively be understood as follows. With increasing deposition rates there is less time for the hydrogen atoms to desorb from the surface. Hence, some hydrogen atoms may not be released into the gas but are trapped within the material. Therefore, the hydrogen concentration increases with deposition rate.

A possible explanation for the increasing microstructure factor at high silane concentrations is the formation of higher order silane molecules in the plasma. The incorporation of these higher order silane molecules into the growing material results in a more porous layer growth because these molecules are not as mobile as radicals. Hence, more silicon atoms are left with more than one dangling bond passivated by a hydrogen atom.

It is known that the incorporation of hydrogen has an influence on the properties of the layer. Therefore, the electrical and optical properties of these layers are studied in the following sections.

5.1.2 Electrical properties

The measurement of the dark- and photo-conductivity is a common method to determine the quality of an intrinsic a-Si:H layer. In the present section the conductivities of various a-Si:H layers are studied in order to investigate the influence of the deposition process and growth rate on the electrical properties.

Figure 5.2 shows the photo-conductivity of i-layers grown a) dynamically by VHF-PECVD processes and b) statically by RF-PECVD processes as a function of the deposition rate of the i-layer. The deposition rate is varied by changing the power density (deposition regimes sRFa1 and dfVHFa1) or the silane concentration (deposition regimes sRFa2 and dfVHFa2) separately while keeping the other process parameters constant. For details on the deposition regimes see table 5.1 and appendix C.

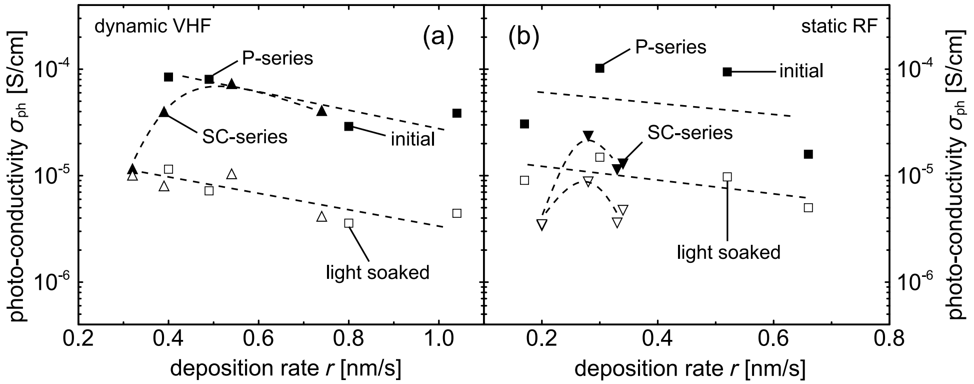

Figure 5.2: Photo-conductivity σ_{ph} in the initial state (closed symbols) and after 300 h of light soaking (open symbols) as a function of the deposition rate r of the i-layer for a) dynamic VHF-PECVD processes and b) static RF-PECVD processes. Layers deposited with varying power densities are marked with squares, layers deposited with varying silane concentrations are marked with triangles. Dashed lines are guides to the eye.

The photo-conductivity of the i-layers in the initial state (closed symbols) is in the order of 10^{-5} S/cm, the dark-conductivity (not shown) is in the order of 10^{-11} S/cm. According to ref. [80] these values are an indication for device quality a-Si:H material. The photo-conductivity decreases with increasing power densities and high deposition rates which is in agreement with the results published in ref. [81]. In contrast, the photo-conductivity decreases towards very low silane concentrations (triangles) and low deposition rates.

With respect to the Staebler-Wronski effect [7] it is known that the conductivity of a-Si:H layers changes during light exposure due to the creation of dangling bonds. In the present work the i-layers were light soaked for 300 h at 50°C under AM1.5 conditions. The aim was to study the light-induced changes in conductivity of the material, depending on the deposition rate and deposition process.

The photo-conductivity of the i-layers after light soaking is plotted with open symbols in figure 5.2. The photo-conductivity decreases during light soaking which is in agreement with the results in ref. [82, 83]. It is found that the ratio of the photo-conductivity before to the photo-conductivity after light soaking is almost constant for increasing power densities. In contrast, the ratio decreases towards very low silane concentrations. This finding indicates that the increase in the defect density depends on the process parameter that is changed in order to vary the deposition rate.

The photo-conductivity depends on the photo-generation of charge carriers as well as the recombination of the charge carriers at defects / dangling bonds. Hence, it is not possible to determine the cause of the trends in photo-conductivity without further assessment of the material properties. Therefore, additional PDS measurements were conducted.

5.1.3 Optical properties

It was mentioned in the previous section that the photo-conductivity of an i-layer depends on the photo-generation as well as on the recombination of charge carriers. Therefore, PDS measurements were carried out in order to study the influence of the deposition rate and process parameter on the absorption spectra of the i-layers. The absorption spectrum is used to derive the E_{04} gap and the sub-gap absorption $\alpha_{1.2\,\mathrm{eV}}$. The sub-gap absorption can be considered as a measure for the defect density for the a-Si:H material [37, 38].

The deposition rate of the i-layer is varied by changing the power density (deposition regime sRFa1 and dfVHFa1) or changing the silane concentration (deposition regime sRFa2 and dfVHFa2) separately while keeping the other deposition parameters constant. For details on the deposition regimes see table 5.1 and appendix C.

In figure 5.3a the E_{04} gap of the i-layers is plotted as a function of the deposition rate. The E_{04} gap is almost constant for varying power densities (squares) but increases towards low silane concentrations (triangles). The latter effect is in agreement with the findings in ref. [51]. The increasing E_{04} gap at low silane concentrations may contribute to the reduced photo-conductivity at low silane concentrations as presented in the previous section.

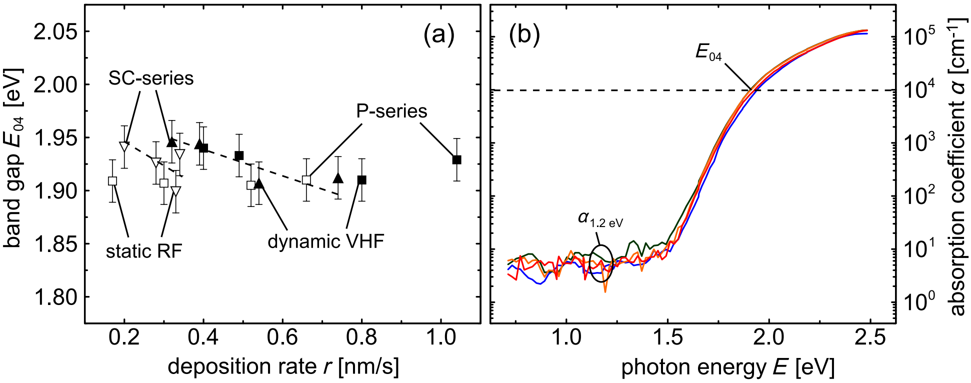

Figure 5.3: a) Band gap E_{04} derived from the PDS spectra of the i-layers as a function of the deposition rate. Closed symbols represent i-layers grown dynamically by VHF-PECVD, open symbols represent i-layers grown statically by RF-PECVD. Layers deposited with varying power densities are marked with squares, layers deposited with varying silane concentrations are marked with triangles. b) Exemplary PDS spectra of i-layers grown in deposition regime dfVHFa1. Dashed lines are guides to the eye.

Figure 5.3b shows the PDS spectra of the i-layers deposited with various power densities in deposition regime dfVHFa1. The absorption spectra do not exhibit a significant difference in the sub-gap absorption. It was found that the sub-gap absorption is between 3–10 cm^{-1} for all i-layers, independent of the deposition rate or process regime. The sub-gap absorption rises during the 300 h of light soaking, but again no correlation with the deposition rate or growth regime is found.

It was suggested in the literature that the sub-gap absorption derived from the PDS spectrum depends on the layer thickness [84]. This thickness dependence is attributed to the contribution of surface defects to the absorption signal. In the present work the i-layer thickness was around 500 nm. It may be possible that the contribution of the surface defects was too high to determine a difference in the defect density of the bulk layer. However, even with a thickness of 500 nm some layers peeled off before any measurement could be made. This problem is related to poor adhesion and mechanical stress within the layer which becomes worse for thicker films.

5.1.4 Summary

The influence of the deposition rate on the i-layer properties has been studied. It was shown that the hydrogen concentration increases with deposition rate, independent of the process parameter that was changed. Additionally, it was found that low silane concentrations lead to a reduction in the microstructure factor and an increase in the band gap. The effects on the i-layer properties were similar for dynamic deposition processes at 60 MHz and static deposition processes at 13.56 MHz.

In the next section i-layers grown at various power densities and silane concentrations are incorporated into a-Si:H solar cells. The aim is to investigate possible correlations between the process regime, deposition rate, i-layer properties and solar cell performance.

5.2 Influence of the deposition rate on the solar cell performance

In the previous section the correlation between the deposition rate and the properties of intrinsic a-Si:H layers has been studied. In the present section these i-layers are incorporated into a-Si:H solar cells in order to investigate the influence of the deposition process, layer properties and growth rate on the solar cell performance. The aim is to assess the potential of dynamic VHF-PECVD processes to deposit a-Si:H i-layers at high growth rates for state-of-the-art solar cells.

The a-Si:H i-layers are deposited statically using a showerhead electrode and RF-PECVD processes or dynamically using linear plasma sources and VHF-PECVD processes. Within a deposition regime only one process parameter is changed at a time. The i-layer thickness is kept between 320–350 nm to ensure that the effects seen are solely related to the deposition process of the i-layer. A short summary of the deposition regimes is given in table 5.2, for more details see appendix C.

Table 5.2: Deposition regimes for the growth of intrinsic a-Si:H layers.

regime	mode	frequency [MHz]	power density [mW/cm^2]	silane concentration [%]	total gas flow [sccm]
sRFa1	static	13.56	21–94	12.4	395
sRFa2	static	13.56	33	4.6–25.3	580
dfVHFa1*	dynamic	60	34–107	28.5	240–865
dfVHFa2*	dynamic	60	53	11–41.6	440-1140

5.2.1 Initial and stabilized solar cell performance as a function of the deposition rate

It is commonly observed that the efficiency of a-Si:H solar cells decreases due to light-induced degradation [7, 85]. The main reason for the decrease in efficiency is the increasing number of dangling bonds. In the present section the efficiency and fill factor of a-Si:H solar cells are studied in order to investigate the influence of the deposition process of the i-layer on the degradation behavior.

Figure 5.4 shows the efficiency and fill factor of the a-Si:H solar cells as a function of the deposition rate of the i-layer. The deposition rate is varied by changing the power density (21–94 mW/cm^2 for sRFa1 and 34–107 mW/cm^2 for dfVHFa1*) or changing the silane concentration (4.6–25.3 % for sRFa2 and 11–41.6 % for dfVHFa2*) separately while the other process parameters are kept constant.

The solar cell efficiency decreases in the initial state linearly with increasing power densities and deposition rates from 9.6 % at 0.2 nm/s to 8.9 % at 1.1 nm/s (squares in figure 5.4a). In contrast, the solar cell efficiency shows a maximum at medium silane concentrations (triangles) which are close to the silane concentrations chosen for deposition regimes sRFa1 and dfVHFa1*. Towards low silane concentrations the solar cell efficiency decreases to about 8.9 %.

The fill factor of the a-Si:H solar cells is almost constant in the initial state (see figure 5.4c). Only at very high power densities and high silane concentrations there is a small decrease in fill factor. Hence, the reduced solar efficiency at high power densities and low silane concentrations is related to changes in the short-circuit current density or open-circuit voltage.

The a-Si:H solar cells were light soaked for 1000 h in order to study the effect of light-induced degradation. The solar cell efficiency after degradation is shown in figure 5.4b.

The decrease in the solar cell efficiency towards high deposition rates is much more pronounced compared to the initial state. The stabilized solar cell efficiency decreases linearly with deposition rate for increasing power densities from 7.8 % at 0.2 nm/s to 5.9 % at 1.1 nm/s. The linear decrease in efficiency with deposition rate for increasing power densities is in agreement with the results published in ref. [86]. Solar cells containing i-layers grown dynamically at 60 MHz (dfVHFa1*) obtain a slightly higher stabilized efficiency than solar cells with i-layers grown statically at 13.56 MHz (sRFa1) at the same growth rate.

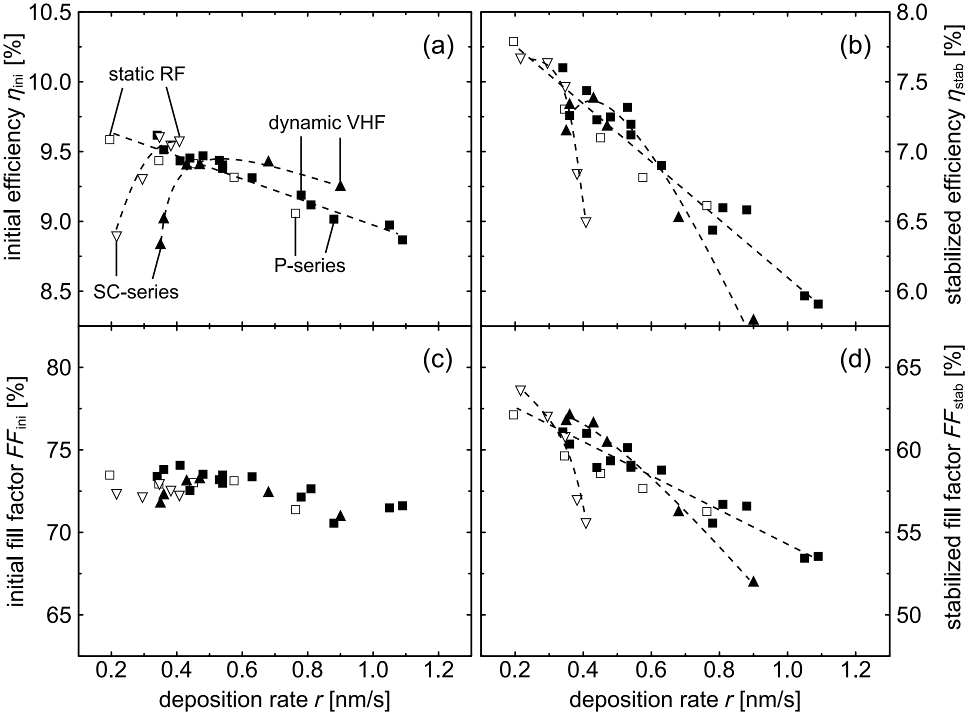

Figure 5.4: Efficiency η and fill factor FF of a-Si:H solar cells as a function of the i-layer deposition rate r. Closed symbols represent i-layers grown dynamically by VHF-PECVD, open symbols represent i-layers grown statically by RF-PECVD. Layers deposited with varying power densities are marked with squares, layers deposited with varying silane concentrations are marked with triangles. Dashed lines are guides to the eye.

The stabilized solar cell efficiency exhibits a maximum at low silane concentrations which is in agreement with the findings in ref. [51]. The maximum shifts towards lower silane concentrations compared to the initial state which indicates a stronger degradation loss at higher silane concentrations. The stabilized efficiency decreases more rapidly towards high silane concentrations than towards high power densities. This finding indicates that a high silane concentration during i-layer growth may lead to lower material quality and a stronger degradation loss than a high power density.

The fill factors of the a-Si:H solar cells after degradation are shown in figure 5.4d. The stabilized fill factor decreases linearly with the deposition rate of the i-layer for increasing power densities which is in agreements with the results published in refs. [86, 87]. Between deposition rates of 0.4–0.6 nm/s the solar cells incorporating i-layers grown dynamically at 60 MHz obtain about 2 % higher fill factors than solar cells incorporating i-layers grown statically at 13.56 MHz. The difference in fill factor is the main reason for the higher efficiencies for solar cells with i-layers grown dynamically at 60 MHz.

For increasing silane concentrations the stabilized fill factor continuously decreases with deposition rate, but more rapidly than for increasing power densities. The maximum in the stabilized efficiency at low silane concentrations can not be explained by the change in fill factor. Therefore, the open-circuit voltage and short-circuit current density have to be studied.

5.2.2 Influence of the process parameters on the stabilized open-circuit voltage and short-circuit current density

It was shown in the previous section that the a-Si:H solar cell efficiency decreases considerably during light soaking. Most of the loss is related to the reduced fill factor which is caused by an increasing number of dangling bonds. However, if the a-Si:H solar cell is to be incorporated into an a-Si:H/μc-Si:H tandem solar cell it is important to study the open-circuit voltage and short-circuit current density as well.

Figure 5.5 shows the stabilized open-circuit voltage and short-circuit current density of the a-Si:H solar cells after 1000 h of light-induced degradation as a function of the i-layer deposition rate. The deposition rate is varied by changing the power density (deposition regime sRFa1 and dfVHFa1*) or silane concentration (deposition regime sRFa2 and dfVHFa2*) separately while keeping the other process parameters constant. For more details on the deposition regimes see table 5.2 and appendix C.

The stabilized open-circuit voltage as shown in figure 5.5a is almost independent of the power density (squares). In contrast, there is a significant decrease in the open-circuit voltage from low to high silane concentrations (triangles) of 40–50 mV.

The reduction of the open-circuit voltage due to light-induced degradation increases with increasing power densities and increasing silane concentrations. Only at very low silane concentrations the open-circuit voltage remains stable. For the lowest silane concentration investigated for regime sRFa1 the open-circuit voltage even increases by 10 mV during light soaking. A similar observation has been reported in [51, 79, 88] but so far no explanation has been found.

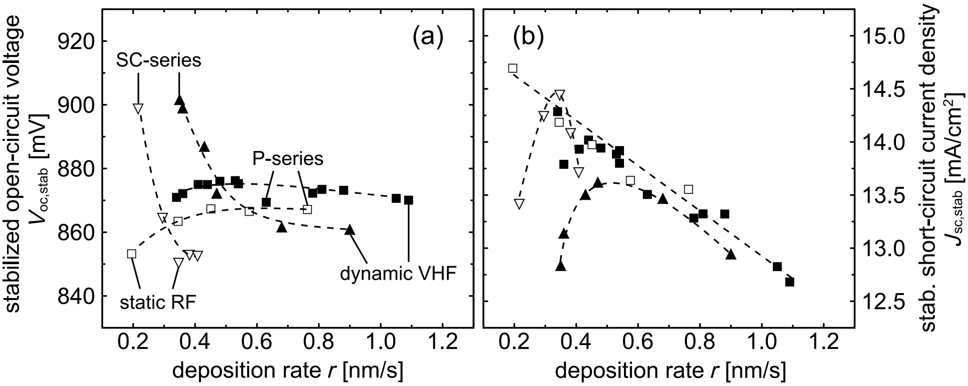

Figure 5.5: Stabilized open-circuit voltage V_{OC} and short-circuit current density J_{SC} of a-Si:H solar cells as a function of the i-layer deposition rate r. Closed symbols represent i-layers grown dynamically by VHF-PECVD, open symbols represent i-layers grown statically by RF-PECVD. Layers deposited with varying power densities are marked with squares, layers deposited with varying silane concentrations are marked with triangles. Dashed lines are guides to the eye.

The stabilized short-circuit current density decreases linearly with deposition rate for increasing power densities as shown in figure 5.5b. In contrast, the short-circuit current density exhibits a maximum at a medium silane concentration. The drop in short-circuit current density towards low silane concentrations coincides with the high open-circuit voltage. According to the results in section 5.1.3 this effect is due to an increasing band gap of the i-layer.

For a possible incorporation of an a-Si:H solar cell into an a-Si:H/μc-Si:H tandem solar cell it is important to study the changes in the short-circuit current density in more detail. Therefore, additional DSR measurements have been carried out.

5.2.3 Origin of reduced short-circuit current density at high growth rates

In the previous section it was shown that the short-circuit current density changes, depending on the process parameters of the i-layer. The short-circuit current density decreases during light-induced degradation, especially for high growth rates of the i-layer. In the present section the origin of the changes in short-circuit current density are studied by analyzing the spectral response of the a-Si:H solar cells.

Exemplary external quantum efficiency curves of solar cells incorporating dynamically deposited a-Si:H i-layers grown at 60 MHz are shown in figure 5.6. The a-Si:H solar cells were light soaked for 1000 h in order to study the effect of light-induced degradation. In figure 5.6 the exemplary external quantum efficiency curves are plotted after light soaking for DSR measurements without a bias voltage (solid curves) and with a bias voltage of -0.3 V (dotted curves).

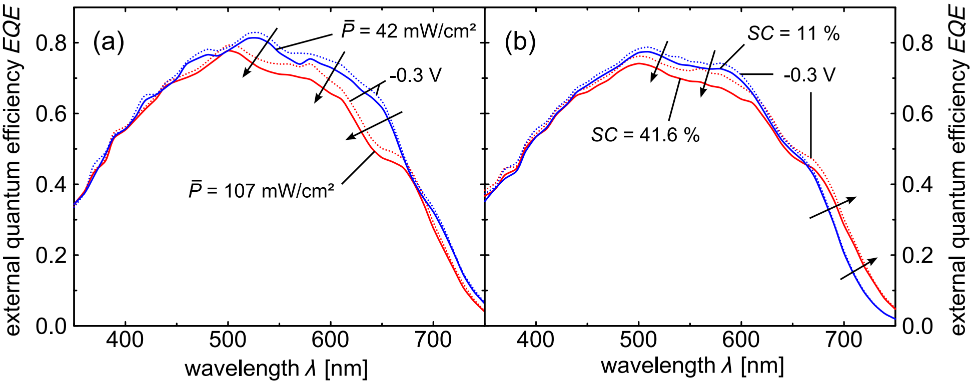

Figure 5.6: External quantum efficiency EQE of a-Si:H solar cells incorporating i-layers deposited at a) different power densities in regime dfVHFa1* and b) different silane concentrations in regime dfVHFa2*. The EQE of the a-Si:H solar cells is displayed after 1000 h of light soaking without bias voltage (solid curves) and with a bias voltage of -0.3 V (dotted curves).

The results in figure 5.6 show that the spectral response in the wavelength region up to about 450 nm is not affected by the deposition process. This finding indicates that within the investigated range of process parameters there is no negative effect of high deposition rates on the quality of the p/i interface. However, the spectral response changes considerably at longer wavelengths, depending on the process parameters.

The spectral response decreases for increasing power densities at wavelengths longer than 450 nm as shown in figure 5.6a. The spectral response can be increased by applying a negative bias voltage which is in conjunction with the low fill factor at high deposition rates as shown in figure 5.4d. The higher charge carrier collection is attributed to the external electric field applied to the solar cell.

The influence of the silane concentration on the spectral response is more complex. The external quantum efficiency increases with silane concentration for wavelengths longer than 650 nm. A possible explanation for this effect is the decreasing band gap of the i-layer at high silane concentrations as shown in section 5.1.3. In contrast, the spectral response decreases with silane concentrations for wavelengths between 450–650 nm. The spectral response can be increased for high silane concentrations using a negative bias voltage which indicates a problem with the charge carrier collection.

The results in the present section show that the decreasing short-circuit current density at high deposition rates (see figure 5.5b) is due to a reduced spectral response for wavelengths longer than 450 nm. The spectral response shows a strong bias voltage dependence indicating a problem with the charge carrier collection. Hence, the lower short-circuit current density at high deposition rates is mainly due to a reduced collection efficiency of photo-generated charge carriers. Only the decrease in short-circuit current density towards low silane concentration is related to a reduced photo-generation of charge carriers (see figure 5.5b).

5.2.4 Summary

The influence of the i-layer deposition process and growth rate on the a-Si:H solar cell performance was studied. It was found that the stabilized efficiency of solar cells incorporating i-layers grown dynamically at 60 MHz was higher than for solar cells incorporating i-layers grown statically at 13.56 MHz with the same deposition rate. It is therefore concluded that the concept of dynamic deposition using linear plasma sources and VHF-PECVD processes is suited to deposit state-of-the-art a-Si:H solar cells.

A stabilized efficiency of 7.6 % for solar cells with i-layers grown dynamically at 0.35 nm/s was obtained which is only marginally lower than the stabilized efficiency of 7.8 % for solar cells with i-layers grown statically at 0.2 nm/s. In the subsequent section the loss in efficiency due to light-induced degradation is studied. The aim is to investigate the correlation between process parameters, growth rate and degradation.

5.3 Influence of the process parameter on the degradation loss

In section 5.2.1 it was shown that the solar cell efficiency decreases for increasing power densities linearly with the deposition rate of the i-layer while there is a maximum in efficiency at medium silane concentrations. In the present section the degradation loss is studied in more detail in order to determine the influence of the process parameters.

Figure 5.4 shows the relative efficiency loss $\Delta\eta/\eta_{\mathrm{ini}}$ of a-Si:H solar cells as a function of the deposition rate of the i-layer. The deposition rate is varied by changing the power density (21–94 mW/cm^2 for sRFa1 and 34–107 mW/cm^2 for dfVHFa1*) or changing the silane concentration (4.6–25.3 % for sRFa2 and 11–41.6 % for dfVHFa2*) separately while the other process parameters are kept constant. For more details on the deposition regimes see table 5.2 and appendix C.

The relative efficiency loss increases continuously towards higher i-layer deposition rates for rising silane concentrations (triangles) and rising power densities (squares) as shown in figure 5.7. For static RF-PECVD processes and dynamic VHF-PECVD processes the relative efficiency loss increases more quickly with deposition rate for increasing silane concentrations than it does for increasing power densities. This finding indicates that the defect density caused by the light-induced degradation of the i-layer increases more rapidly with deposition rate for rising silane concentrations. The different influences of the process parameters on the degradation behavior can intuitively be understood as follows.

The deposition rate increases towards higher silane concentrations and power densities because of the larger number of growth precursors impinging on the surface. Hence, the time for the growth precursor to find an energetically preferred state for material growth is reduced. This effect may lead to a larger number of silicon atoms forming weak bonds with the surface. If these weak bonds are incorporated into the i-layer they can break during light-induced degradation leading to dangling bonds / defects.

High power densities lead to an increasing plasma potential and high ion energies. The higher kinetic energy of the ions increases the chance of removing weakly bonded silicon atoms off the surface during the impact of the ion. It is therefore suggested that the increased plasma potential at high power densities plays an important role for the i-layer quality at high deposition rates.

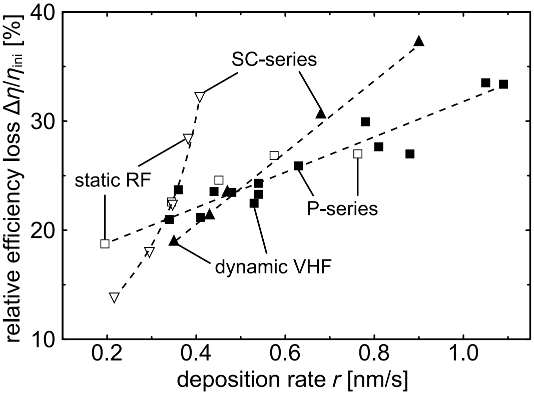

Figure 5.7: Relative efficiency loss $\Delta\eta/\eta_{\mathrm{ini}}$ of a-Si:H solar cells as a function of the i-layer deposition rate r. Closed symbols represent i-layers grown dynamically by VHF-PECVD, open symbols represent i-layers grown statically by RF-PECVD. Layers deposited with varying power densities are marked with squares, layers deposited with varying silane concentrations are marked with triangles. Dashed lines are guides to the eye.

It was shown that the relative efficiency loss increases more rapidly with deposition rate for rising silane concentration than it does for rising power densities. Hence, the relative efficiency loss at a certain deposition rate can be minimized by growing the i-layer at a high power density but a low silane concentration. However, it has to be noted that a low silane concentration may not lead to the highest stabilized efficiency because of the strong reduction in short-circuit current density as shown in figures 5.4 and 5.5. It is therefore suggested to first optimize the silane concentration for the i-layer process in order to obtain high stabilized efficiencies. Subsequently the deposition rate can be increased by applying a higher power density.

5.4 Interdependency of process parameters

In section 2.2.2 the process parameters for thin-film silicon PECVD processes have been discussed. Some process parameters can be changed without having a direct influence on other process parameters such as power density, total gas flow, silane concentration, electrode distance, excitation frequency, pressure and temperature. However, there are process parameters that depend on one or more process parameters such as the residence time of gas molecules or the gas utilization.

In the present section the influence of power density, silane concentration and total gas flow on the gas utilization and growth rate of the a-Si:H i-layer is studied. The aim is to investigate interdependencies between the process parameters and discuss the effects on the growth rate and solar cell performance.

In figure 5.8a the deposition rate of a-Si:H i-layers grown dynamically at 60 MHz is shown as a function of the power density at $SC = 28.5$ % (deposition regime dfVHFa1*) and of the silane concentration at $\overline{P} = 53$ mW/cm^2 (deposition regime dfVHFa2*). The process parameters are adjusted separately while keeping the other process parameters constant. For more details on the deposition regimes see table 5.2 and appendix C.

The deposition rate rises continuously with increasing power densities and silane concentrations for a fixed total gas flow as shown in figure 5.8a (closed symbols). In contrast, the gas utilization rises with increasing power densities but it decreases with rising silane concentrations as shown in figure 5.8b.

In section 4.2 it was shown that the local deposition conditions depend on the input silane concentration and the gas utilization because of the cross-flow geometry. Hence, different levels of gas utilization result in changing local silane concentrations in gas flow direction for a given input silane concentration. As a result, a dynamically deposited i-layer encounters different silane concentrations over the course of a deposition process, depending on the gas utilization.

Additional solar cells were deposited with different degrees of gas utilization for the i-layer deposition process by changing the total gas flow in order to study its influence on the deposition rate and solar cell performance (open symbols). The results in figure 5.8 indicate that there is little change in the deposition rate for a gas utilization up to about 25 %. However, the i-layer deposited at the highest power density and a gas utilization of more than 45 % (open square) exhibits a significantly lower deposition rate than the i-layers deposited at the same power density but lower gas utilization.

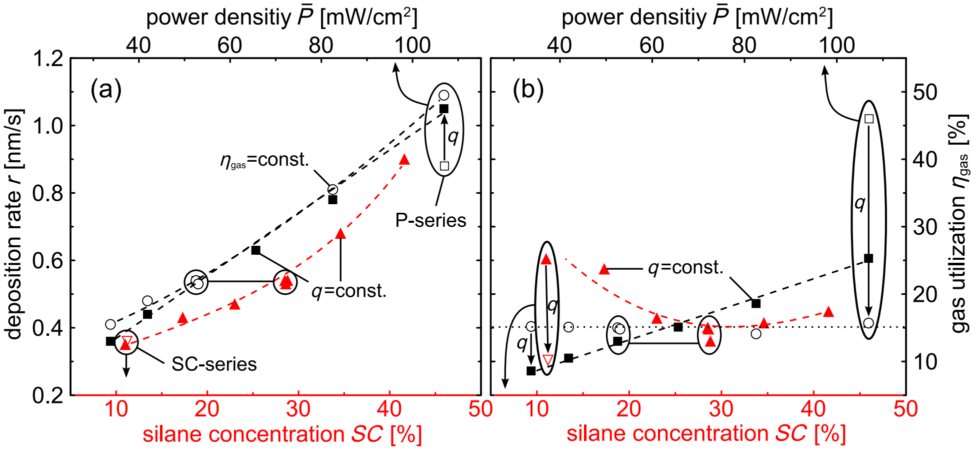

Figure 5.8: Deposition rate r of the i-layer and gas utilization η_{gas} as a function of the power density (squares and circles) or silane concentration (triangles) for dynamic VHF-PECVD processes. Closed symbols represent regimes where the total gas flow was kept constant, open symbols represent experiments where the total gas flow was varied in order to obtain a certain gas utilization.

The reduced average growth rate at high gas utilization and low gas flow can intuitively be explained as follows. At high gas utilization there is a strong gradient in the silane concentration from the gas feed towards the exhaust. Hence, the average silane concentration across the electrode decreases with increasing gas utilization for a given input silane concentration. The results in figure 5.8a show that the deposition rate decreases towards lower silane concentrations. Therefore, the average deposition rate decreases with increasing gas utilization for a fixed input silane concentration.

It was shown that varying the power density or silane concentration changes not only the deposition rate but also the gas utilization. Because of the cross-flow design for the linear plasma sources this effects leads to changes in the average silane concentration across the electrode which may influence the deposition rate. However, within the investigated range of gas utilization the solar cell performance correlates well with the i-layer deposition rate and the process parameter that was varied. Therefore, solar cells with i-layers grown at varying gas flows / gas utilization have not been marked separately for the deposition regimes dfVHFa1* and dfVHFa2* in sections 5.2 and 5.3.

5.5 Reduced deposition times for thin-film silicon tandem solar cells

In sections 4.4 and 5.2 the influence of the absorber layer deposition rate on the performance of single-junction μc-Si:H and a-Si:H solar cells was studied. Figure 5.9 shows the best solar cell efficiencies as a function of the i-layer deposition rate. It is found in figure 5.9a that the efficiency of μc-Si:H solar cells is almost independent of the deposition rate. In contrast, the stabilized solar cell efficiency of the a-Si:H solar cells strongly decreases with increasing deposition rate (see figure 5.9b).

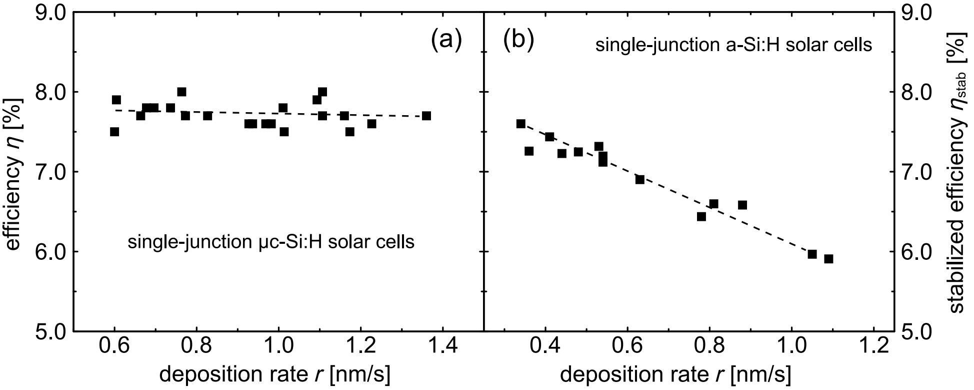

Figure 5.9: Efficiency η of a) single-junction μc-Si:H solar cells and b) single-junction a-Si:H solar cells as a function of the i-layer deposition rate. The lines are guides to the eye.

The efficiency of an a-Si:H/μc-Si:H tandem solar cells can not be calculated directly from the efficiencies of the single-junction solar cells. Therefore, a simplified model is applied in the present section that uses the photovoltaic parameters of the single-junction solar cells in order to get an estimate for the efficiencies of corresponding a-Si:H/μc-Si:H tandem solar cells. The aim is to study the influence of increasing deposition rates for the a-Si:H and μc-Si:H absorber layers on the tandem solar cell performance and assess the potential time reduction for the deposition process.

5.5.1 Simplified tandem solar cell model

The device characteristics of thin-film silicon solar cells have been simulated by various groups using models based on the optical and electrical parameters of all single layers [43, 89, 90]. These models are applied in order to study the influence of the absorber layer thickness or substrate morphology on the solar cell performance. The effect of light-induced degradation or reduced material quality due to high deposition rates is typically not investigated.

In the present section a simplified model is introduced that uses the photovoltaic parameters of single-junction solar cells in order to get an estimate for the a-Si:H/μc-Si:H tandem solar cell performance. The aim is not to predict the efficiency of a tandem solar cell with the same accuracy as device-based models but to obtain a qualitative measure for the tandem solar cell performance depending on the deposition rates of the a-Si:H and μc-Si:H absorber layers. As a result, it is possible to evaluate the potential for reduced deposition times with respect to the changes in the tandem solar cell efficiency.

Table 5.3 shows the photovoltaic parameters of a-Si:H and μc-Si:H solar cells incorporating i-layers grown at the standard rate or at high deposition rate. Note, that stabilized photovoltaic parameters are given for the a-Si:H solar cells.

Table 5.3: Photovoltaic parameters of a-Si:H and μc-Si:H solar cells incorporating intrinsic layers grown at different deposition rates.

		a-Si:H standard	a-Si:H high rate	μc-Si:H standard	μc-Si:H high rate
i-layer deposition rate	[nm/s]	0.35	1.05	0.6	1.4
efficiency	[%]	7.6	5.9	7.9	7.7
fill factor	[%]	61	53	67	68
open-circuit voltage	[mV]	870	870	510	505
short-circuit current density	[mA/cm^2]	14.3	12.8	23.3	22.6

The parameters shown in table 5.3 are used in order to determine the photovoltaic parameters of the tandem solar cell as follows:

- The fill factor of the tandem solar cell is assumed to be limited by the fill-factor of the single-junction a-Si:H solar cell: $FF_{\text{tandem}} = FF_{\text{a-Si:H}}$
- The open-circuit voltage of the tandem solar cell is the sum of the open-circuit voltages of the single-junction solar cells: $V_{\text{OC,tandem}} = V_{\text{OC,a-Si:H}} + V_{\text{OC},\mu\text{c-Si:H}}$

- The short-circuit current densities of the top- and bottom solar cell are assumed to be matched at 11.5 mA/cm^2 for a tandem solar cell incorporating a-Si:H and μc-Si:H i-layers grown at standard deposition rates.

- A reduced short-circuit current density in a single-junction solar cell at higher deposition rates leads to the same reduction in the short-circuit current density of the tandem solar cell (e.g. the drop in J_{SC} from 14.3 mA/cm^2 to 12.8 mA/cm^2 in the a-Si:H solar cell leads to a reduction of the J_{SC} in the tandem solar cell from 11.5 mA/cm^2 to 10 mA/cm^2).

- The a-Si:H/μc-Si:H tandem solar cell efficiency is calculated by multiplying the fill factor, open-circuit voltage and short-circuit current density and dividing the product by the integrated spectral irradiance of the AM1.5 spectrum (100 mW/cm^2).

By applying the method described above a stabilized tandem solar cell efficiency of about 9.7 % is estimated for i-layers deposited at the standard growth rates using VHF-PECVD processes. This efficiency is referred to as η_{std} and taken as a benchmark for tandem solar cells incorporating i-layers grown at higher deposition rates.

5.5.2 Correlation between growth rate and solar cell performance

In the previous section a simplified model has been introduced to get an estimate for the efficiency of an a-Si:H/μc-Si:H tandem solar cell based on the photovoltaic parameters of single-junction a-Si:H and μc-Si:H solar cells. In the present section the influence of the growth rates of the absorber layers on the tandem solar cell performance is studied.

In order to correlate the deposition rates with deposition times the thicknesses of the a-Si:H and μc-Si:H absorber layers are assumed to be 350 nm and 1200 nm (similar to the thicknesses in the single-junction solar cells presented in sections 5.2 and 4.3). Hence, the corresponding deposition times for the i-layers grown at standard deposition rates are 16.7 min and 33.3 min, respectively.

Figure 5.10 shows the relative efficiency η/η_{std} as a function of the ratio between the time saved (due to a higher deposition rate) and the total deposition time of the i-layers for standard deposition rates. To increase the number of data points a linear relationship between the deposition rate and the photovoltaic parameters of the single-junction solar cells is assumed.

The results in figure 5.10 show that the efficiency of the tandem solar cell strongly depends on the deposition rate of the a-Si:H absorber layer. This effect is due to the strong decrease in the stabilized solar cell efficiency of the a-Si:H single-junction solar cells with increasing i-layer deposition rate as shown in figure 5.9b.

In contrast, the tandem solar cell efficiency is almost constant for increasing deposition rates of the μc-Si:H absorber layer. This effect is due to the efficiency of the μc-Si:H solar cells being almost independent of the deposition rate within the investigated range of growth rates as shown in figure 5.9a.

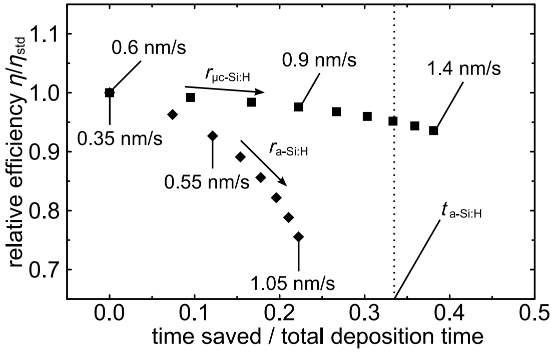

Figure 5.10: Relative efficiency η/η_{std} as a function of the ratio between time saved and total deposition time of the i-layers.

Increasing the deposition rate of the a-Si:H i-layer from 0.35 nm/s to 0.55 nm/s has about the same negative effect on the tandem solar cell efficiency as increasing the deposition rate of the μc-Si:H i-layer from 0.6 nm/s to 1.4 nm/s. However, increasing the μc-Si:H deposition rate to 1.4 nm/s leads to a reduction in the total deposition time of almost 40 % while the higher a-Si:H deposition rate decreases the total deposition time by only 12 %. The deposition time of the a-Si:H absorber layer can be reduced further by applying higher deposition rates but this leads to a strong decrease in the tandem solar cell efficiency.

The findings in the present section show that increasing the deposition rate of the μc-Si:H absorber layer has a significantly higher potential in reducing the total deposition time of the i-layers compared to increasing the deposition rate of the a-Si:H absorber layer. Additionally, the high deposition rate of the μc-Si:H absorber layer has only little influence on the performance of the tandem solar cell efficiency which is in agreement with the findings in ref. [91]. Furthermore, studies have shown that the deposition time of the i-layers can be reduced by using thinner absorber layers [54, 56, 66] and intermediate reflectors [92, 93] without compromising on the stabilized tandem solar cell efficiency.

5.5.3 Discussion of the model validity

In section 5.5.1 a simplified model was presented that gives an estimate for the efficiency of an a-Si:H/μc-Si:H solar cell using the photovoltaic parameters of the single-junction solar cells. In the present section the assumptions that the model is based on are discussed briefly.

- The chosen numbers for the i-layer thicknesses and the current-matching condition are based on results with state-of-the-art a-Si:H, μc-Si:H and tandem solar cells deposited using RF-PECVD processes in the LADA system. The results of the single-junction solar cells grown by RF-PECVD (see sections 4.1 and 5.2) are very similar to the results for solar cells incorporating i-layers grown by VHF-PECVD at standard growth rates (see table 5.3). Therefore, the i-layer thicknesses and current-matching condition are believed to introduce only a small error.

- The a-Si:H solar cells were deposited on Asahi type U substrates. Hence, the deposition of the tandem solar cell on texture-etched ZnO:Al may lead to changes in the spectral response and photovoltaic parameters of the a-Si:H top-cell [94]. However, the strong decrease in the stabilized efficiency at high i-layer deposition rates is mainly related to the reduced fill factor because of the higher defect density. This effect occurs independent of the substrate and leads to a similar trend for a-Si:H solar cells on a texture-etched ZnO:Al substrate.

- The lower short-circuit current density of the a-Si:H single-junction solar cells at high i-layer growth rates is due to a reduced spectral response for wavelengths longer than 450 nm. The model assumes that the loss in short-circuit current density in a single-junction a-Si:H solar cell has the same effect on the short-circuit current density in the tandem junction solar cell. This assumption is expected to overestimate the loss in the short-circuit current density because the spectral response of the a-Si:H top-cell and μc-Si:H bottom-cell overlap between 500–700 nm [66, 95].

- If the short-circuit current density of the top- / bottom-cell is reduced it would be possible to use a thinner bottom- / top-cell absorber layer because the other sub-cell does not need to generate 11.5 mA/cm^2 as for the standard tandem cell. Especially for high growth rates of the a-Si:H absorber layer this is important because the μc-Si:H absorber layer takes much longer to deposit. However, it has to be noted that the strong negative influence of high a-Si:H deposition rates on the tandem solar cell performance still occurs.

5.5.4 Summary

It was shown that high growth rates of the a-Si:H absorber layer have a strong negative impact on the performance of a-Si:H/μc-Si:H solar cells while high growth rates of the μc-Si:H absorber layer only lead to a small decrease in efficiency. Because of the μc-Si:H absorber layer being much thicker than the a-Si:H absorber layer it is concluded that increasing the deposition rate of μc-Si:H is the key to short deposition times without compromising on the tandem solar cell efficiency.

5.6 Conclusions

Deposition processes for a-Si:H absorber layers were developed using a dynamic VHF-PECVD technique that can be scaled up easily and allows high deposition rates for high-quality μc-Si:H absorber layers. It was found that that solar cells incorporating i-layers grown dynamically at 60 MHz perform as good or better than solar cells incorporating i-layers grown statically at 13.56 MHz with the same deposition rate. Hence, it is concluded that the dynamic VHF-PECVD technique developed in the framework of the present thesis is capable of producing state-of-the-art a-Si:H solar cells.

The best a-Si:H solar cells incorporating i-layers grown dynamically by VHF-PECVD obtained a stabilized efficiency of 7.6 % at a deposition rate of 0.35 nm/s which is only slightly lower than the efficiency of 7.8 % at a deposition rate of 0.2 nm/s for solar cells with i-layers grown statically by RF-PECVD. In general, the stabilized a-Si:H solar cell efficiency decreases towards high growth rates. However, at low silane concentrations and low growth rates the stabilized solar cell efficiency exhibits a maximum.

The comparison of initial and stabilized solar cell efficiencies shows that the degradation loss increases more rapidly with deposition rate for increasing silane concentrations than it does for rising power densities, independent of the excitation frequency and gas distribution system. This finding indicates that the defect density rises more quickly during light-induced degradation for i-layers deposited at high silane concentrations. It is therefore suggested to first optimize the silane concentration for the i-layer deposition and subsequently adjust the deposition rate by changing the power density.

For dynamic deposition processes using a linear gas distribution system it was found that a gas utilizations lower than 25 % has only a marginal influence on the deposition rate of the a-Si:H absorber layer and the solar cell performance. At higher gas utilizations the deposition rate of the absorber layer is reduced and the stabilized solar cell efficiency increases compared to processes using a low gas utilization and higher deposition rates. This effect is related to the reduced silane concentrations across the electrode at high gas utilization.

At the end of this chapter a simplified model was introduced to study the effect of increasing deposition rates for the i-layer deposition on the performance of thin-film silicon tandem solar cells. It was found that rising deposition rates for the a-Si:H absorber layer have a strong negative influence on the efficiency of the tandem solar cell and only a moderate potential for shorter deposition times. In contrast, high deposition rates for the μc-Si:H absorber layer offer a significant reduction in the total i-layer deposition time with little negative impact on the solar cell performance.

6 Summary and Outlook

The aim of the present work was to develop a scalable process for state-of-the-art a-Si:H and μc-Si:H solar cells at high rates. The use of very-high frequencies has proven to be beneficial for the quality of μc-Si:H grown at high deposition rates. However, very-high frequencies typically lead to an inhomogeneous deposition if conventional planar VHF-PECVD systems are scaled up to large areas. Therefore, the system used in the present study applies linear plasma sources which facilitate the up-scaling of VHF-PECVD processes to large substrate areas without compromising on the homogeneity.

In chapter 3a system for dynamic VHF-PECVD of thin-film silicon was developed. It was found that the plasma stability is strongly affected by the electrical contact between the moving substrate carrier and signal ground. This finding is due to the fact that the substrate carrier serves as counter electrode. Hence, a temporary loss of the electrical contact leads to an unstable plasma. Therefore, the carrier grounding was evaluated and redesigned in order to ensure stable plasma conditions.

In conventional large-area static PECVD systems showerhead electrodes are used to distribute the gas homogeneously across the substrate area to ensure a uniform deposition process. These electrodes are very complex which makes the manufacturing costly and complicates the electrode replacement. For the linear plasma sources a linear gas distribution system was chosen that separates the gas feed from the electrode and ensures a homogeneous gas distribution perpendicular the the movement direction of the substrate. Hence, this configuration eases manufacturing and reduces equipment related costs.

To ensure the reproducibility of the deposition processes for a-Si:H and μc-Si:H single-junction solar cells a process sequence was developed that minimizes effects of cross-contamination which may occur due to the deposition of doped and intrinsic layers within the same deposition chamber.

In chapter 4 the correlation between the growth rate of μc-Si:H i-layers, their crystallinity, the solar cell performance and the deposition process was studied. It was found that static RF- and static VHF-PECVD processes exhibit a very similar correlation between these parameters, independent of the deposition regime, excitation frequency or gas distribution system.

Microcrystalline silicon solar cells incorporating i-layers deposited statically by VHF-PECVD using linear plasma sources and a linear gas distribution system obtain state-of-the-art efficiencies close to 8 % at deposition rates up to 1.4 nm/s. Within the investigated range of i-layer deposition rates there is almost no negative influence of the growth rate on the performance of the μc-Si:H solar cell.

The results in section 4.2 show that the linear gas distribution system – also referred to as cross-flow geometry – leads to an inhomogeneous static deposition profile for μc-Si:H at high gas utilization because of the changing silane concentration in gas flow direction. The repeated change of growth conditions encountered by the moving substrate during a dynamic i-layer deposition process leads to a small decrease in the μc-Si:H solar cell efficiency. Solar cell incorporating i-layer deposited dynamically by VHF-PECVD obtained efficiencies up to 7.3 % at a growth rate of 0.95 nm/s.

The changing silane concentrations during a dynamic i-layer deposition process were studied systematically using a static RF-PECVD process and applying a time-dependent silane concentration. It was found that, if the change in silane concentration exceeds a critical level, the efficiency of the μc-Si:H solar cells is reduced. It is therefore concluded that a homogeneous silane concentration across the the width of the linear plasma source may facilitate the dynamic deposition of high-quality i-layers resulting in the same efficiency as for solar cells incorporating statically deposited i-layers.

In chapter 5 the influence of the a-Si:H i-layer growth rate, deposition technique and process parameters on the solar cell performance was studied. The results show that a-Si:H solar cells incorporating i-layers grown dynamically by VHF-PECVD perform as good or better as solar cells incorporating i-layers grown statically by RF-PECVD at the same deposition rate. State-of-the-art stabilized a-Si:H solar cell efficiencies of 7.6 % were obtained for a growth rate of 0.35 nm/s using dynamic VHF-PECVD processes.

It was found that the stabilized a-Si:H solar cell efficiency strongly decreases with higher i-layer deposition rates. The results in section 5.3 indicate that the degradation loss increases more rapidly with deposition rate for high silane concentrations than it does for high power densities. This finding suggests that the defect density due to light-induced degradation increases more rapidly with deposition rate for high silane concentrations.

A simplified model was presented that was used to obtain an estimate for the efficiency of an a-Si:H/μc-Si:H tandem solar cell based on the photovoltaic parameters of the single-junction solar cells. The aim was to study the effects of the individual i-layer deposition rates on the performance of the tandem solar cell. The results show that an increasing μc-Si:H deposition rate has a much higher potential to reduce the deposition time of the silicon absorber layers than an increasing a-Si:H deposition rate. Additionally, high a-Si:H deposition rates have a strong negative influence on the tandem solar cell performance, contrary to high μc-Si:H deposition rates. Hence, a high deposition rate of the μc-Si:H absorber layer is key to reduce the deposition times of the silicon absorber layers with compromising on the tandem solar cell performance.

The results in the present work show that state-of-the-art a-Si:H and μc-Si:H single-junction solar cells can be deposited incorporating i-layers grown dynamically by VHF-PECVD processes using linear plasma sources. The combination of very-high frequencies and electrodes that are scaled up in only one dimension offers the possibility to deposit high-quality thin-film silicon layers homogeneously on large areas at high rates. Ultimately, the dynamic deposition concept may be used to deposit high-quality thin-film silicon solar cells on cheap flexible substrates, further reducing the cost per watt.

Outlook

For μc-Si:H solar cells state-of-the-art efficiencies for i-layer deposition rates up to about 3 nm/s have been reported using VHF-PECVD processes [18, 19]. It is therefore concluded that the deposition rate of 1.4 nm/s obtained in this work can be further increased by optimizing the process parameters (e.g. reducing the electrode distance).

The results in the present work show that a dynamic μc-Si:H i-layer deposition process leads to a small reduction in the solar cell efficiency compared to solar cells with statically deposited i-layers. This effect is related to the changing growth conditions throughout the deposition process. Additionally, the possible incorporation of powder and an increasing contamination may have a negative influence on the material properties (see section 4.5). It is therefore suggested that future work has to focus on these two effects in order to determine if high-quality μc-Si:H layers can be deposited at high growth rates without any negative influence of the dynamic deposition process.

For a-Si:H it was shown that dynamic VHF-PECVD processes can be used to deposit i-layers of the same quality as for static RF-PECVD processes resulting in a state-of-the-art solar cell performance. However, the results indicate that the solar cell efficiency strongly decreases with deposition rate of the i-layer if the power density or silane concentration is increased.

Results presented in refs. [86, 96, 97] show that it is possible to increase the stabilized efficiency of a-Si:H solar cells at a given i-layer deposition rate by increasing the deposition pressure. This method is believed to be applicable to the dynamic VHF-PECVD process as well offering further improvements in the deposition rate while maintaining high stabilized a-Si:H solar cell efficiencies.

Within the last years it was demonstrated that a-Si:H/μc-Si:H tandem solar cells using very thin absorber layers offer a significant reduction in the deposition time without compromising on the solar cell performance [54, 56, 66]. The i-layer thicknesses of the a-Si:H top-cell and μc-Si:H bottom cell are in the order of 200 nm and 900 nm, respectively. Assuming a deposition rate of 0.35 nm/s for a-Si:H and 1.4 nm/s for μc-Si:H the total i-layer deposition time would be about 20 minutes. This value is roughly half the deposition time for a state-of-the-art industrial RF-PECVD system as shown in ref. [56]. This finding proves the potential of the dynamic deposition concept using linear plasma sources and VHF-PECVD to reduce the deposition time.

The key to high-efficiency a-Si:H/μc-Si:H tandem solar cells is the optimization of the light-trapping [98, 99]. The reflection of light as well as the parasitic absorption in the TCO and doped layers reduce the short-circuit current density considerably [43].

To improve the light scattering and minimize the reflection loss a textured glass can be used [100]. Additionally, doped amorphous silicon oxide layers with a microcrystalline phase can be grown with a large band gap and low absorption using PECVD processes. These doped layers can be used as p-layer of the a-Si:H top-cell reducing the parasitic absorption [95]. Furthermore, they can be applied as an interlayer between the top- and bottom-cell to reflect light back into the top-cell which allows using very thin a-Si:H absorber layers [92, 93]. The thinner a-Si:H top-cell would exhibit a lower degradation loss [65] and offer shorter deposition times. All these processes / concepts are basically compatible with the dynamic deposition technique.

Appendices

A Material properties of doped layers

Within the present work a fixed set of doped layers was used for the a-Si:H and μc-Si:H single-junction solar cells. Both cell types contain the same a-Si:H n-layer with a thickness of about 15 nm. In contrast, a 10 nm a-Si:H p-layer is used for the a-Si:H solar cell while a 20 nm μc-Si:H p-layer is used for the μc-Si:H solar cells. For details on the doped layer properties see table A.1. Note, that the crystallinity of the μc-Si:H p-layer was determined on a texture-etched ZnO:Al using a laser wavelength of 488 nm.

Table A.1: Material properties of the doped a-Si:H and μc-Si:H layers.

layer type	thickness [nm]	conductivity [S/cm]	crystallinity [%]	E_{04} gap [eV]
(n)-a-Si:H	≈15	9.65×10^{-3}		1.91
(p)-a-Si:H	≈10	4.6×10^{-6}		2.03
(p)-μc-Si:H	≈20	8.0×10^{-2}	63	2.01

The doped layers have been grown statically using RF-PECVD processes in PC1 with similar process parameters as the standard RF-PECVD i-layers. Phosphine was added to the gas phase in order to deposit the n-doped a-Si:H layer while TMB was added to the gas phase for the p-layer deposition. In case of the a-Si:H p-layer additionally methane was added to the gas phase in order to increase the band gap of the material and reduce the optical absorption.

B Deposition regimes for intrinsic μc-Si:H

In chapter 4 different deposition regimes for intrinsic μc-Si:H have been presented. The deposition regimes were abbreviated in a way that indicates the mode of operation, the excitation frequency, the material type and a number to identify the process regime.

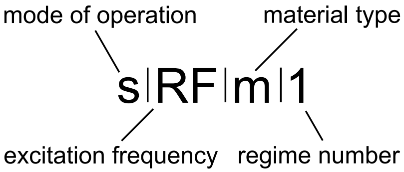

Table B.1 gives a list of the letters used for the abbreviation and their meaning.

Table B.1: Meaning of letters used for abbreviations of process regimes.

	letter(s)	meaning	remarks
mode of operation	s	static	
	df	dynamic, full oscillation	
	ds	dynamic, short oscillation	
excitation frequency	RF	13.56 MHz	planar electrode
	VHF	60 MHz	linear plasma source
material type	m	μc-Si:H	
	a	a-Si:H	

Note, that the planar electrode uses a showerhead while the linear plasma sources are using a linear gas distribution system. Hence, the electrode type is linked to a certain gas distribution system and a certain excitation frequency.

Table B.2 lists the process parameters for all μc-Si:H i-layer deposition regimes used in chapter 4.

Table B.2: Process parameters for μc-Si:H i-layer deposition regimes.

regime	f [MHz]	p [mbar]	$\overline{P}$ [W/cm^2]	q_{total} [sccm]	SC [%]	T_s [°C]	d_el [mm]	η_gas [%]
sRFm1	13.56	12.5	0.33	3030	0.6–1.2	180	≈10	60–65
sVHFm1	60	4	0.22	525	4.6–7.2	180	≈11	55–65
sVHFm2	60	6	0.52	5100	1.2–2.2	180	≈11	40–50
sVHFm3	60	7	0.69-0.94	5100	2.2	180	≈11	35
sVHFm4	60	8	0.71-0.95	5100	2.2	180	≈11	30
dfVHFm1	60	4	0.22	525	4.7	180	≈11	60
dfVHFm2	60	6	0.52	5100	1.2	180	≈11	40
dsVHFm2	60	6	0.52	5100	1.2	180	≈11	40

C Deposition regimes for intrinsic a-Si:H

In chapter 5 different deposition regimes for intrinsic a-Si:H have been presented. The deposition regimes were abbreviated in a way that indicates the mode of operation, the excitation frequency, the material type and a number to identify the process regime. For details on the encoding of the abbreviation see table B.1 in the previous section.

Table C.1 lists the process parameters for all a-Si:H i-layer deposition regimes used in chapter 5.

Table C.1: Process parameters for a-Si:H i-layer deposition regimes.

regime	f [MHz]	p [mbar]	$\overline{P}$ [mW/cm^2]	q_{total} [sccm]	SC [%]	T_{s} [°C]	d_{el} [mm]	η_{gas} [%]
sRFa1	13.56	4	21–94	395	12.4	180	≈10	14–55
sRFa2	13.56	4	33	580	4.6–25.3	180	≈10	10–29
dfVHFa1	60	1	34–107	525	28.5	180	≈11	9–25
dfVHFa1*	60	1	34–107	240–865	28.5	180	≈11	5–46
dfVHFa2	60	1	53	445	11–41.6	180	≈11	15–25
dfVHFa2*	60	1	53	440–1140	11–41.6	180	≈11	10–25

Bibliography

[1] D. M. Chapin, C. S. Fuller, G. L. Pearson. A New Silicon p–n Junction Photocell for Converting Solar Radiation Into Electrical Power. *Journal of Applied Physics* **1954**;**25(5)**, pp. 676–677. doi:10.1063/1.1721711.

[2] A. L. Endrös. Mono- and Tri-Crystalline Si for PV Application. *Solar Energy Materials and Solar Cells* **2002**;**72(1-4)**, pp. 109–124. doi:10.1016/S0927-0248(01)00156-8.

[3] L. L. Kazmerski. Solar Photovoltaics R&D at the Tipping Point: A 2005 Technology Overview. *Journal of Electron Spectroscopy and Related Phenomena* **2006**;**150(2-3)**, pp. 105–135. doi:10.1016/j.elspec.2005.09.004.

[4] D. E. Carlson, C. R. Wronski. Amorphous Silicon Solar Cell. *Applied Physics Letters* **1976**;**28(11)**, pp. 671–673. doi:10.1063/1.88617.

[5] D. A. Cusano. CdTe Solar Cells and Photovoltaic Heterojunctions In II–VI Compounds. *Solid-State Electronics* **1963**;**6(3)**, pp. 217–232. doi:10.1016/0038-1101(63)90078-9.

[6] S. Wagner, J. L. Shay, P. Migliora, H. M. Kasper. CulnSe2CdS Heterojunction Photovoltaic Detectors. *Applied Physics Letters* **1974**;**25(8)**, pp. 434–435. doi:10.1063/1.1655537.

[7] D. Staebler, C. Wronski. Reversible Conductivity Changes in Discharge-Produced Amorphous Si. *Applied Physics Letters* **1977**;**31(4)**, pp. 292–294. doi:10.1063/1.89674.

[8] J. Meier, R. Fluckiger, H. Keppner, A. Shah. Complete Microcrystalline p–i–n Solar-Cell – Crystalline or Amorphous Cell Behavior? *Applied Physics Letters* **1994**;**65(7)**, pp. 860–862. doi:10.1063/1.112183.

[9] F. Finger, P. Hapke, M. Luysberg, R. Carius, H. Wagner, M. Scheib. Improvement of Grain Size and Deposition Rate of Microcrystalline Silicon by use of Very High Frequency Glow Discharge. *Applied Physics Letters* **1994**;**65(20)**, pp. 2588–2590. doi:10.1063/1.112604.

[10] A. V. Shah, M. Vanecek, J. Meier, F. Meillaud, J. Guillet, D. Fischer, C. Droz, X. Niquille, S. Fay, E. Vallat-Sauvain, V. Terrazzoni-Daudrix, J. Bailat. Basic Efficiency Limits, Recent Experimental Results and Novel Light-Trapping Schemes in a-Si:H, μc-Si:H and 'Micromorph Tandem' Solar Cells. *Journal of Non-Crystalline Solids* **2004**;**338**, pp. 639–645. doi:10.1016/j.jnoncrysol.2004.03.074.

[11] T. Roschek, T. Repmann, O. Kluth, J. Muller, B. Rech, H. Wagner. High Rate Deposition of Microcrystalline Silicon Solar Cells Using 13.56 MHz PECVD – Prerequisites and Limiting Factors. In *MRS Proceedings*, volume 715 of *San Francisco*. **2002**; pp. 635–640. doi:DOI:10.1557/PROC-715-A26.5.

[12] T. Roschek, T. Repmann, J. Muller, B. Rech, H. Wagner. Comprehensive Study of Microcrystalline Silicon Solar Cells Deposited at High Rate Using 13.56 MHz Plasma-Enhanced Chemical Vapor Deposition. *Journal of Vacuum Science & Technology A* **2002**;**20(2)**, pp. 492–498. doi:10.1116/1.1450585.

[13] B. Rech, T. Roschek, T. Repmann, J. Müller, R. Schmitz, W. Appenzeller. Microcrystalline Silicon for Large Area Thin Film Solar Cells. *Thin Solid Films* **2003**; **427(1-2)**, pp. 157–165. doi:10.1016/S0040-6090(02)01210-5.

[14] B. Rech, T. Repmann, J. Hüpkes, M. Berginski, H. Stiebig, W. Beyer, V. Sittinger, F. Ruske. Recent Progress in Amorphous and Microcrystalline Silicon Based Solar Cell Technology. In *Proceedings of the 20th European Photovoltaic Solar Energy Conference*, Barcelona. **2005**; pp. 1481–1486.

[15] T. Repmann, W. Appenzeller, B. Sehrbrock, H. Stiebig, B. Rech. Advanced PECVD Process for Thin-Film Silicon Solar Cells on Glass. In *Proceedings of the 19th European Photovoltaic Solar Energy Conference*, Paris. **2004**; pp. 1334–1339.

[16] H. Takatsuka, M. Noda, Y. Yonekura, Y. Takeuchi, Y. Yamauchi. Development of

High Efficiency Large Area Silicon Thin Film Modules Using VHF-PECVD. *Solar Energy* **2004**;**77(6)**, pp. 951–960. doi:10.1016/j.solener.2004.06.007.

[17] Y. Mai, S. Klein, R. Carius, J. Wolff, A. Lambertz, F. Finger, X. Geng. Microcrystalline Silicon Solar Cells Deposited at High Rates. *Journal of Applied Physics* **2005**;**97(11)**, p. 114913. doi:10.1063/1.1927689.

[18] Y. Nakano, S. Goya, T. Watanabe, N. Yamashita, Y. Yonekura. High-Deposition-Rate of Microcrystalline Silicon Solar Cell by Using VHF PECVD. *Thin Solid Films* **2006**;**506–507**, pp. 33–37. doi:10.1016/j.tsf.2005.08.026.

[19] A. Gordijn, M. Vanecek, W. J. Goedheer, J. K. Rath, R. E. I. Schropp. Influence of Pressure and Plasma Potential on High Growth Rate Microcrystalline Silicon Grown by Very High Frequency Plasma Enhanced Chemical Vapour Deposition. *Japanese Journal of Applied Physics* **2006**;**45(8A)**, pp. 6166–6172. doi:10.1143/JJAP.45.6166.

[20] X. Han, G. Hou, X. Zhang, G. Li, C. Wei, Z. Dai, X. Chen. Two Effective Approaches for Improvement of High Rate Growth μc-Si:H Solar Cell Performance. In *Proceedings of the 24th European Photovoltaic Solar Energy Conference*, Hamburg. **2009**; pp. 2631–2633. doi:10.4229/24thEUPVSEC2009-3AV.2.8.

[21] X. Y. Han, G. F. Hou, X. D. Zhang, C. C. Wei, G. J. Li, J. J. Zhang, X. L. Chen, D. K. Zhang, J. Sun, Y. Zhao, X. H. Geng. Improvement of Hydrogenated Microcrystalline Silicon Solar Cell Performance by VHF Power Profiling Technique. *Solar Energy Materials and Solar Cells* **2010**;**94(2)**, pp. 254–257. doi:10.1016/j.solmat.2009.09.010.

[22] L. Sansonnens, J. Schmitt. Shaped Electrode and Lens for a Uniform Radio-Frequency Capacitive Plasma. *Applied Physics Letters* **2003**;**82(2)**, pp. 182–184. doi:10.1063/1.1534918.

[23] T. Takagi, M. Ueda, N. Ito, Y. Watabe, H. Sato, K. Sawaya. Large Area VHF Plasma Sources. *Thin Solid Films* **2006**;**502(1-2)**, pp. 50–54. doi:10.1016/j.tsf.2005.07.235.

[24] J. Rüdiger, H. Brechtel, A. Kottwitz, J. Kuske, U. Stephan. VHF Plasma Processing for In-Line Deposition Systems. *Thin Solid Films* **2003**;**427(1-2)**, pp. 16–20. doi:10.1016/S0040-6090(02)01174-4.

[25] R. C. Chittick, J. H. Alexander, H. F. Sterling. The Preparation and Properties of Amorphous Silicon. *Journal of the Electrochemical Society* **1969**;**116(1)**, pp. 77–81. doi:10.1149/1.2411779.

[26] S. Veprek, V. Marecek. Preparation of Thin Layers of Ge and Si by Chemical Hydrogen Plasma Transport. *Solid-State Electronics* **1968**;**11(7)**, pp. 683–684. doi:10.1016/0038-1101(68)90071-3.

[27] M. N. van den Donker, B. Rech, F. Finger, W. M. M. Kessels, M. C. M. van de Sanden. Highly Efficient Microcrystalline Silicon Solar Cells Deposited From a Pure SiH4 Flow. *Applied Physics Letters* **2005**;**87(26)**, p. 263503. doi:10.1063/1.2152115.

[28] B. Strahm, A. A. Howling, L. Sansonnens, C. Hollenstein, U. Kroll, J. Meier, C. Ellert, L. Feitknecht, C. Ballif. Microcrystalline Silicon Deposited at High Rate on Large Areas From Pure Silane With Efficient Gas Utilization. *Solar Energy Materials and Solar Cells* **2007**;**91(6)**, pp. 495–502. doi:10.1016/j.solmat.2006.10.024.

[29] T. Roschek, B. Rech, J. Muller, R. Schmitz, H. Wagner. Influence of the Total Gas Flow on the Deposition of Microcrystalline Silicon Solar Cells. *Thin Solid Films* **2004**;**451**, pp. 466–469. doi:10.1016/j.tsf.2003.10.128.

[30] J. Meier, U. Kroll, E. Vallat-Sauvain, J. Spitznagel, U. Graf, A. Shah. Amorphous Solar Cells, the Micromorph Concept and the Role of VHF-GD Deposition Technique. *Solar Energy* **2004**;**77(6)**, pp. 983–993. doi:10.1016/j.solener.2004.08.026.

[31] A. Matsuda. Thin-Film Silicon – Growth Process and Solar Cell Application. *Japanese Journal of Applied Physics Part 1 – Regular Papers Short Notes & Review Papers* **2004**;**43(12)**, pp. 7909–7920. doi:10.1143/JJAP.43.7909.

[32] A. Matsuda. Growth Mechanism of Microcrystalline Silicon Obtained From Reactive Plasmas. *Thin Solid Films* **1999**;**337(1-2)**, pp. 1–6. doi:10.1016/S0040-6090(98)01165-1.

[33] G. Dingemans, M. N. van den Donker, A. Gordijn, W. M. M. Kessels, M. C. M. van de Sanden. Probing the Phase Composition of Silicon Films In Situ by Etch Product Detection. *Applied Physics Letters* **2007**;**91(16)**, p. 161902. doi:10.1063/1.2799738.

[34] K. Nakamura, K. Yoshino, S. Takeoka, I. Shimizu. Roles of Atomic Hydrogen in Chemical Annealing. *Japanese Journal of Applied Physics Part 1 – Regular Papers Short Notes & Review Papers* **1995**;**34(2A)**, pp. 442–449. doi:10.1143/JJAP.34.442.

[35] O. Vetterl, P. Hapke, F. Finger, L. Houben, M. Luysberg, H. Wagner. Growth of Microcrystalline Silicon Using the Layer-by-Layer Technique at Various Plasma Excitation Frequencies. *Journal of Non-Crystalline Solids* **1998**;**227**, pp. 866–870. doi:10.1016/S0022-3093(98)00198-7.

[36] W. B. Jackson, N. M. Amer, A. C. Boccara, D. Fournier. Photothermal Deflection Spectroscopy and Detection. *Applied Optics* **1981**;**20(8)**, pp. 1333–1344. doi:10.1364/AO.20.001333.

[37] W. B. Jackson, N. M. Amer. Direct Measurement of Gap-State Absorption in Hydrogenated Amorphous Silicon by Photothermal Deflection Spectroscopy. *Physical Review B* **1982**;**25(8)**, pp. 5559–5562. doi:10.1103/PhysRevB.25.5559.

[38] N. Wyrsch, F. Finger, T. J. McMahon, M. Vanecek. How to Reach More Precise Interpretation of Subgap Absorption Spectra in Terms of Deep Defect Density in a-Si:H. *Journal of Non-Crystalline Solids* **1991**;**137**, pp. 347–350. doi:10.1016/S0022-3093(05)80127-9.

[39] C. Smit, R. A. C. M. M. van Swaaij, H. Donker, A. M. H. N. Petit, W. M. M. Kessels, M. C. M. van de Sanden. Determining the Material Structure of Microcrystalline Silicon from Raman Spectra. *Journal of Applied Physics* **2003**;**94(5)**, pp. 3582–3588. doi:10.1063/1.1596364.

[40] N. Maley. Critical Investigation of the Infrared-Transmission-Data Analysis of Hydrogenated Amorphous Silicon Alloys. *Physical Review B* **1992**;**46(4)**, pp. 2078–2085. doi:10.1103/PhysRevB.46.2078.

[41] A. Langford, M. Fleet, B. Nelson, W. Lanford, N. Maley. Infrared Absorption Strength and Hydrogen Content of Hydrogenated Amorphous Silicon. *Physical Review B* **1992**;**45(23)**, pp. 13367–13377. doi:10.1103/PhysRevB.45.13367.

[42] C. A. Gueymard, D. Myers, K. Emery. Proposed Reference Irradiance Spectra for Solar Energy Systems Testing. *Solar Energy* **2002**;**73(6)**, pp. 443–467. doi: 10.1016/S0038-092X(03)00005-7.

[43] K. Ding, T. Kirchartz, B. E. Pieters, C. Ulbrich, A. M. Ermes, S. Schicho, A. Lambertz, R. Carius, U. Rau. Characterization and Simulation of a-Si:H/μc-Si:H Tandem Solar Cells. *Solar Energy Materials and Solar Cells* **2011**;**95**, pp. 3318–3327. doi:10.1016/j.solmat.2011.07.023.

[44] P. Lechner, H. Schade. Photovoltaic Thin-Film Technology Based on Hydrogenated Amorphous Silicon. *Progress In Photovoltaics* **2002**;**10(2)**, pp. 85–97. doi:10.1002/pip.412.

[45] H. Schmidt, L. Sansonnens, A. A. Howling, C. Hollenstein, M. Elyaakoubi, J. P. M. Schmitt. Improving Plasma Uniformity Using Lens-Shaped Electrodes in a Large Area Very High Frequency Reactor. *Journal of Applied Physics* **2004**;**95(9)**, pp. 4559–4564. doi:10.1063/1.1690096.

[46] H. Takatsuka, Y. Yamauchi, K. Kawamura, H. Mashima, Y. Takeuchi. World's Largest Amorphous Silicon Photovoltaic Module. *Thin Solid Films* **2006**;**506**, pp. 13–16. doi:10.1016/j.tsf.2005.08.011.

[47] T. Takagi, M. Ueda, N. Ito, Y. Watabe, M. Kondo. Microcrystalline Silicon Solar Cells Fabricated Using Array-Antenna-Type Very High Frequency Plasma-Enhanced Chemical Vapor Deposition System. *Japanese Journal of Applied Physics Part 1 – Regular Papers Brief Communications & Review Papers* **2006**; **45(5A)**, pp. 4003–4005. doi:10.1143/JJAP.45.4003.

[48] M. Vetter, J. P. Borrajo, C. Mata, J. Andreu. Progress in the Fabrication of Amorphous Silicon Photovoltaic Modules on Very Large 2.60$m \times$2.20m Glass Substrates. In *Proceedings of the 24th European Photovoltaic Solar Energy Conference*, Hamburg. **2009**; pp. 2408–2411. doi:10.4229/24thEUPVSEC2009-3CO.13.4.

[49] M. N. van den Donker, R. Schmitz, W. Appenzeller, B. Rech, W. M. M. Kessels, M. C. M. van de Sanden. The Role of Plasma Induced Substrate Heating During High Rate Deposition of Microcrystalline Silicon Solar Cells. *Thin Solid Films* **2006**;**511**, pp. 562–566. doi:10.1016/j.tsf.2005.12.167.

[50] O. Kluth, B. Rech, L. Houben, S. Wieder, G. Schope, C. Beneking, H. Wagner, A. Loffl, H. W. Schock. Texture Etched ZnO : Al Coated Glass Substrates for Silicon Based Thin Film Solar Cells. *Thin Solid Films* **1999**;**351(1-2)**, pp. 247–253. doi:10.1016/S0040-6090(99)00085-1.

[51] R. Platz, D. Fischer, S. Dubail, A. Shah. a-Si:H/a-Si:H Stacked Cell From VHF-Deposition in a Single Chamber Reactor With 9 % Stabilized Efficiency. *Solar Energy Materials and Solar Cells* **1997**;**46(2)**, pp. 157–172. doi:10.1016/S0927-0248(97)00008-1.

[52] U. Kroll, C. Bucher, S. Benagli, I. Schonbachler, J. Meier, A. Shah, J. Ballutaud, A. Howling, C. Hollenstein, A. Buchel, M. Poppeller. High-Efficiency p–i–n a-Si:H Solar Cells With Low Boron Cross-Contamination Prepared in a Large-Area Single-Chamber PECVD Reactor. *Thin Solid Films* **2004**;**451**, pp. 525–530. doi:10.1016/j.tsf.2003.11.036.

[53] T. Merdzhanova, J. Wördenweber, T. Zimmermann, U. Zastrow, A. J. Flikweert, H. Stiebig, W. Beyer, A. Gordijn. Single-Chamber Process for a-Si:H Solar Cell Deposition. *Solar Energy Materials and Solar Cells* **2011**;doi:DOI:10.1016/j.solmat.2011.10.022.

[54] J. Bailat, L. Fesquet, J.-B. Orhan, Y. Djeridane, B. Wolf, P. Madliger, J. Steinhauser, S. Benagli, D. Borrello, L. Castens, G. Monteduro, M. Marmelo, B. Dehbozorghi, E. Vallat-Sauvain, X. Multone, D. Romang, J.-F. Boucher, J. Meier, U. Kroll, M. Despeisse, G. Bugnon, C. Ballif, S. Marjanovic, G. Kohnke, N. Borrelli, K. Koch, J. Liu, R. Modavis, D. Thelen, S. Vallon, A. Zakharian, D. Weidman. Recent Developments of High-Efficiency Micromorph Tandem Solar Cells in KAI-M PECVD Reactors. In *Proceedings of the 25th European Photovoltaic Solar Energy Conference and Exhibition / 5th World Conference on Photovoltaic Energy Conversion*, Valencia. **2010**; pp. 2720–2723. doi:10.4229/25thEUPVSEC2010-3BO.11.5.

[55] Y. Ue, S. Asari, K. Saito. Evolution of Amorphous/Microcrystalline Silicon Tandem Solar Cells. In *Proceedings of the 25th European Photovoltaic Solar Energy Conference and Exhibition / 5th World Conference on Photovoltaic Energy Conversion*, Valencia. **2010**; pp. 2713–2715. doi:10.4229/25thEUPVSEC2010-3BO.11.2.

[56] S. Klein, M. Rohde, S. Buschbaum, D. Severin. Throughput Optimized a-Si/μc-Si Tandem Solar Cells on Sputter-Etched ZnO Substrates. *Solar Energy Materials and Solar Cells* **2012**;**98**, pp. 363–369. doi:10.1016/j.solmat.2011.10.029.

[57] Y. Mai, S. Klein, R. Carius, H. Stiebig, G. X, F. Finger. Open Circuit Voltage Improvement of High-Deposition-Rate Microcrystalline Silicon Solar Cells by Hot Wire Interface Layers. *Applied Physics Letters* **2005**;**87(7)**, p. 073503. doi:10.1063/1.2011771.

[58] O. Vetterl, R. Carius, L. Houben, C. Scholten, M. Luysberg, A. Lambertz, F. Finger, H. Wagner. Effects of Structural Properties of μc-Si:H Absorber Layers on Solar Cell Performance. In *MRS Proceedings*, volume 609 of *San Francisco*. **2000**; pp. 1521–1526. doi:10.1557/PROC-609-A15.2.

[59] S. Klein, T. Repmann, T. Brammer. Microcrystalline Silicon Films and Solar Cells Deposited by PECVD and HWCVD. *Solar Energy* **2004**;**77(6)**, pp. 893–908. doi:10.1016/j.solener.2004.08.029.

[60] L. Houben, M. Luysberg, P. Hapke, R. Carius, F. Finger, H. Wagner. Structural Properties of Microcrystalline Silicon in the Transition From Highly Crystalline to Amorphous Growth. *Philosophical Magazine A – Physics of Condensed Matter Structure Defects and Mechanical Properties* **1998**;**77(6)**, pp. 1447–1460. doi:10.1080/01418619808214262.

[61] F. Finger, S. Klein, T. Dylla, A. L. B. Neto, O. Vetterl, R. Carius. Defects in Microcrystalline Silicon Prepared With Hot Wire CVD. In *MRS Proceedings*, volume 715 of *San Francisco*. **2002**; pp. 123–134.

[62] A. Gordijn, A. Pollet-Villard, M. van den Donker, J. Wolff, F. Finger. Influence of the Gas Flow Geometry on the Performance of Microcrystalline Silicon P-I-N Solar

Cells. In *Proceedings of the 22nd European Photovoltaic Solar Energy Conference*, Milan. **2007**; pp. 2222–2225.

[63] T. Zimmermann, C. Strobel, M. Albert, W. Beyer, A. Gordijn, A. J. Flikweert, J. Kuske, J. W. Bartha. Inline Deposition of Microcrystalline Silicon Solar Cells Using a Linear Plasma Source. *Physica Status Solidi C – Current Topics In Solid State Physics* **2010**;**7(3-4)**, pp. 1097–1100. doi:10.1002/pssc.200982684.

[64] O. Vetterl, F. Finger, R. Carius, P. Hapke, L. Houben, O. Kluth, A. Lambertz, A. Muck, B. Rech, H. Wagner. Intrinsic Microcrystalline Silicon: A New Material for Photovoltaics. *Solar Energy Materials and Solar Cells* **2000**;**62(1-2)**, pp. 97–108. doi:10.1016/S0927-0248(99)00140-3.

[65] S. Benagli, D. Borrello, E. Vallat-Sauvain, J. Meier, U. Kroll, J. Hoetzel, J. Bailat, J. Steinhauser, M. Marmelo, G. Monteduro, L. Castens. High-Efficiency Amorphous Silicon Devices on LPCVD-ZnO TCO Prepared in Industrial KAI-M R & D Reactor. In *Proceedings of the 24th European Photovoltaic Solar Energy Conference*, Hamburg. **2009**; pp. 2293–2298. doi:10.4229/24thEUPVSEC2009-3BO.9.3.

[66] S. Schicho, D. Hrunski, R. van Aubel, A. Gordijn. High Potential of Thin (< 1 μm) a-Si:H/μc-Si:H Tandem Solar Cells. *Progress In Photovoltaics* **2010**;**18(2)**, pp. 83–89. doi:10.1002/pip.929.

[67] P. Torres, J. Meier, R. Fluckiger, U. Kroll, J. A. A. Selvan, H. Keppner, A. Shah, S. D. Littelwood, I. E. Kelly, P. Giannoules. Device Grade Microcrystalline Silicon Owing to Reduced Oxygen Contamination. *Applied Physics Letters* **1996**;**69(10)**, pp. 1373–1375. doi:10.1063/1.117440.

[68] T. Kilper, W. Beyer, G. Brauer, T. Bronger, R. Carius, M. N. van den Donker, D. Hrunski, A. Lambertz, T. Merdzhanova, A. Muck, B. Rech, W. Reetz, R. Schmitz, U. Zastrow, A. Gordijn. Oxygen and Nitrogen Impurities in Microcrystalline Silicon Deposited Under Optimized Conditions: Influence on Material Properties and Solar Cell Performance. *Journal of Applied Physics* **2009**;**105(7)**, p. 074509. doi:10.1063/1.3104781.

[69] T. Merdzhanova, J. Woerdenweber, W. Beyer, U. Zastrow, H. Stiebig, A. Gordijn. High Critical Oxygen Concentration in Microcrystalline Silicon Solar Cells. *Phys-*

ica Status Solidi – Rapid Research Letters **2010**;**4(11)**, pp. 323–325. doi: 10.1002/pssr.201004312.

[70] J. Woerdenweber, T. Merdzhanova, H. Stiebig, W. Beyer, A. Gordijn. Critical Oxygen Concentration in Hydrogenated Amorphous Silicon Solar Cells Dependent on the Contamination Source. *Applied Physics Letters* **2010**;**96(10)**, p. 103505. doi:10.1063/1.3357424.

[71] A. A. Howling, L. Sansonnens, J. L. Dorier, C. Hollenstein. Time-Resolved Measurements of Highly Polymerized Negative Ions in Radio Frequency Silane Plasma Deposition Experiments. *Journal of Applied Physics* **1994**;**75(3)**, pp. 1340–1353. doi:10.1063/1.356413.

[72] J. L. Dorier, C. Hollenstein, A. A. Howling, U. Kroll. Powder Dynamics In Very High Frequency Silane Plasmas. *Journal of Vacuum Science & Technology A* **1992**; **10(4)**, pp. 1048–1052. doi:10.1116/1.578200.

[73] M. N. van den Donker, E. A. G. Hamers, G. M. W. Kroesen. Measurements and Semi-Empirical Model Describing the Onset of Powder Formation as a Function of Process Parameters in an RF Silane-Hydrogen Discharge. *Journal of Physics D-applied Physics* **2005**;**38(14)**, pp. 2382–2389. doi:10.1088/0022-3727/38/14/013.

[74] B. Strahm, C. Hollenstein. Powder Formation in SiH4-H2 Discharge in Large Area Capacitively Coupled Reactors: A Study of the Combined Effect of Interelectrode Distance and Pressure. *Journal of Applied Physics* **2010**;**107(2)**, p. 023302. doi: 10.1063/1.3282802.

[75] T. Kamei, T. Wada. Oxygen Impurity Doping into Ultrapure Hydrogenated Microcrystalline Si Films. *Journal of Applied Physics* **2004**;**96(4)**, pp. 2087–2090. doi:10.1063/1.1767609.

[76] A. J. Flikweert, T. Zimmermann, T. Merdzhanova, D. Weigand, W. Appenzeller, A. Gordijn. Microcrystalline Thin-Film Solar Cell Deposition on Moving Substrates Using a Linear VHF-PECVD Reactor and a Cross-Flow Geometry. *Journal of Physics D – Applied Physics* **2012**;**45(1)**, p. 015101. doi: 10.1088/0022-3727/45/1/015101.

[77] T. Takahama, S. Okamoto, K. Ninomiya, M. Nishikuni, N. Nakamura, S. Tsuda, M. Ohnishi, S. Nakano, Y. Kishi, Y. Kuwano. Application of High Temperature Deposition to a-Si Solar Cells. In *Technical Digest of the International PVSEC-5*, Kyoto. **1990**; pp. 375–378.

[78] R. Platz, C. Hof, D. Fischer, J. Meier, A. Shah. High-T_s Amorphous Top Cells for Increased Top Cell Currents in Micromorph Tandem Cells. *Solar Energy Materials and Solar Cells* **1998**;**53(1-2)**, pp. 1–13. doi:10.1016/S0927-0248(97)00284-5.

[79] C. Beneking, B. Rech, J. Folsch, H. Wagner. Recent Developments in Amorphous Silicon-Based Solar Cells. *Physica Status Solidi B – Basic Research* **1996**;**194(1)**, pp. 41–53. doi:10.1002/pssb.2221940106.

[80] R. Schropp, M. Zeman. *Amorphous and Microcrystalline Silicon Solar Cells: Modeling, Materials and Device Technology.* 0-7923-8317-6. Kluwer Academic Publishers, **1998**.

[81] T. Seth, P. N. Dixit, O. S. Panwar, R. Bhattacharyya. Effect of Power and Pressure on the Properties of Hydrogenated Amorphous Silicon Films Prepared by DC Glow Discharge. *Solar Energy Materials and Solar Cells* **1993**;**31(2)**, pp. 215–226. doi:10.1016/0927-0248(93)90052-5.

[82] R. Banerjee, S. Ghosh, S. Chattopadhyay, A. K. Bandyopadhyay, P. Chaudhuri, A. K. Batabyal, A. K. Barua. Hydrogenated Amorphous Silicon Films Prepared at High Substrate Temperature: Properties and Light Induced Degradation. *Journal of Applied Physics* **1993**;**73(11)**, pp. 7435–7440. doi:10.1063/1.353986.

[83] D. Das, S. Chattopadhyay, A. K. Barua, R. Banerjee. Study of Effects of Interelectrode Spacing and Preheating of Source Gases on Hydrogenated Amorphous Silicon Films Prepared at High Growth Rates. *Journal of Applied Physics* **1995**;**78(5)**, pp. 3193–3199. doi:10.1063/1.360689.

[84] H. Curtins, N. Wyrsch, A. V. Shah. High-Rate Deposition of Amorphous Hydrogenated Silicon: Effect of Plasma Excitation Frequency. *Electronics Letters* **1987**;**23(5)**, pp. 228–230. doi:10.1049/el:19870160.

[85] M. Stutzmann, W. B. Jackson, C. C. Tsai. Light-Induced Metastable Defects in Hydrogenated Amorphous Silicon : A Systematic Study. *Physical Review B* **1985**; **32(1)**, pp. 23–47. doi:10.1103/PhysRevB.32.23.

[86] S. Sheng, L. Li, T. K. Won, Y. K. Chae, S. Y. Choi, J. White, M. Frei. Amorphous Silicon Solar Cells and Modules Fabricated at High Deposition Rates for Optimal Resistance to Light Degradation Based on Large Area PECVD Cluster System. In *Proceedings of the 22th European Photovoltaic Solar Energy Conference*, Milan. **2007**; pp. 2234–2237.

[87] B. Rech, H. Wagner. Potential of Amorphous Silicon for Solar Cells. *Applied Physics A – Materials Science & Processing* **1999**;**69(2)**, pp. 155–167. doi:10.1007/s003390050986.

[88] S. Muthmann, A. Gordijn. Amorphous Silicon Solar Cells Deposited With Non-Constant Silane Concentration. *Solar Energy Materials and Solar Cells* **2011**; **95(2)**, pp. 573–578. doi:10.1016/j.solmat.2010.09.019.

[89] M. Zeman, J. A. Willemen, L. L. A. Vosteen, G. Tao, J. W. Metselaar. Computer Modelling of Current Matching in a-Si:H/a-Si:H Tandem Solar Cells on Textured TCO Substrates. *Solar Energy Materials and Solar Cells* **1997**;**46(2)**, pp. 81–99. doi:10.1016/S0927-0248(96)00094-3.

[90] J. Krc, F. Smole, M. Topic. Analysis of Light Scattering in Amorphous Si:H Solar Cells by a One-Dimensional Semi-Coherent Optical Model. *Progress In Photovoltaics* **2003**;**11(1)**, pp. 15–26. doi:10.1002/pip.460.

[91] A. Terakawa, M. Hishida, S. Yata, W. Shinohara, A. Kitahara, H. Yoneda, Y. Aya, I. Yoshida, M. Iseki, M. Tanaka. SANYO's R&D on Thin-Film Silicon Solar Cells. In *Proceedings of the 26th European Photovoltaic Solar Energy Conference and Exhibition*, Hamburg. **2011**; pp. 2362–2365. doi:10.4229/26thEUPVSEC2011-3BO.4.2.

[92] D. Dominé, P. Buehlmann, J. Bailat, A. Billet, A. Feltrin, C. Ballif. High-Efficiency Micromorph Silicon Solar Cells with In-Situ Intermediate Reflector Deposited on Various Rough LPCVD ZnO. In *Proceedings of the 23rd European Photovoltaic*

Solar Energy Conference and Exhibition, Valencia. **2008**; pp. 2091–2095. doi: 10.4229/23rdEUPVSEC2008-3CO.9.3.

[93] A. Lambertz, T. Grundler, F. Finger. n-Type Hydrogenated Amorphous Silicon Oxide Containing a Microcrystalline Silicon Phase as an Intermediate Reflector in Thin-Film Silicon Solar Cells. In *Proceedings of the 24th European Photovoltaic Solar Energy Conference*, Hamburg. **2009**; pp. 2402–2407. doi: 10.4229/24thEUPVSEC2009-3CO.13.3.

[94] S. Benagli, J. Hötzel, D. Borrello, J. Spitznagel, U. Kroll, J. Meier, E. Vallat-Sauvain, J. Bailat, L. Castens, P.-A. Madliger, B. Dehbozorgi, G. Monteduro, M. Marmelo, Y. Djeridane. High Performance LPCVD-ZnO TCO used in P-I-N Amorphous Silicon & Micromorph Tandem Devices Prepared in Industrial Kai-M R&D Reactor. In *Proceedings of the 23rd European Photovoltaic Solar Energy Conference and Exhibition*, Valencia. **2008**; pp. 2414–2418. doi:10.4229/23rdEUPVSEC2008-3AV.2.23.

[95] S. Klein, S. Wieder, S. Buschbaum, K. Schwankitz, T. Stolley, D. Severin, P. Obermeyer, M. Kress, E. Sommer, T. Marschner, M. Martini, S. Noll-Baumann, J. Haack, U. I. Schmidt, A. Straub, K. Ahmed, K. Schuegraf. Large Area Thin-Film Solar Modules With 10 % Efficiency for Mass Production. In *Proceedings of the 25th European Photovoltaic Solar Energy Conference and Exhibition / 5th World Conference on Photovoltaic Energy Conversion*, Valencia. **2010**; pp. 2708–2712. doi:10.4229/25thEUPVSEC2010-3BO.11.1.

[96] B. Rech, T. Roschek, J. Muller, S. Wieder, H. Wagner. Amorphous and Microcrystalline Silicon Solar Cells Prepared at High Deposition Rates using RF (13.56 MHz) Plasma Excitation Frequencies. *Solar Energy Materials and Solar Cells* **2001**;**66(1-4)**, pp. 267–273. doi:10.1016/S0927-0248(00)00183-5.

[97] D. Hrunski, B. Rech, T. Repmann, J. Kirchhoff, A. Gordijn, J. Hüpkes, W. Appenzeller. A Novel Method of Optimization at a Constant Desposition Rate: Application to Thin-Film Amorphous Silicon Solar Cells. In *Proceedings of the 23rd European Photovoltaic Solar Energy Conference and Exhibition*, Valencia. **2008**; pp. 2292–2296. doi:10.4229/23rdEUPVSEC2008-3AV.1.36.

[98] M. Vanecek, J. Springer, A. Poruba, O. Kluth, T. Repmann, B. Rech, N. Wyrsch, J. Meier, A. Shah. Light Trapping and Optical Losses in Microcrystalline Si and Micromorph Solar Cells. In *Proceedings of the 3rd World Conference on Photovoltaic Energy Conversion*, Osaka. **2003**; pp. 1527–1532.

[99] J. Muller, B. Rech, J. Springer, M. Vanecek. TCO and Light Trapping in Silicon Thin Film Solar Cells. *Solar Energy* **2004**;**77(6)**, pp. 917–930. doi:10.1016/j.solener.2004.03.015.

[100] U. Kroll, J. Meier, L. Fesquet, J. Steinhauser, S. Benagli, J. Orhan, B. Wolf, D. Borrello, L. Castens, Y. Djeridane, X. Multone, G. Choong, D. Domine, J.-F. Boucher, P.-A. Madliger, M. Marmelo, G. Monteduro, B. Dehbozorgi, D. Romang, E. Omnes, M. Chevalley, G. Charitat, A. Pomey, E. Vallat-Sauvain, S. Marjanovic, G. Kohnke, K. Koch, J. Liu, R. Modavis, D. Thelen, S. Vallon, A. Zakharian, D. Weidman. Recent Developments of High-Efficiency Micromorph Tandem Solar Cells in KAI-M/ Plasmabox PECVD Reactors. In *Proceedings of the 26th European Photovoltaic Solar Energy Conference*, Hamburg. **2011**; pp. 2340–2343. doi:10.4229/26thEUPVSEC2011-3BO.2.6.

Acknowledgements

First of all I would like to thank Prof. Bartha and Prof. Rau for giving me the chance to work at IHM and IEK5 during the time of my dissertation as well as their effort of being the reviewers of this thesis. Furthermore, I'm very thankful to Dr. Aad Gordijn for being my mentor during the last two and a half years. You were always pushing me to make sure I'll understand all aspects related to my work.

Next, I have to name a few colleagues who made sure that the experiments ran smoothly. Thank you Arjan for all your work on the LADA system - without you it would not have been possible to run it fully automated. Taking out the human factor was key to ensure the reproducibility of the experiments. Thanks to Daniel and Wolfgang for your help with all the hardware. It was a bumpy ride but you guys made sure that the downtimes never became too long.

Tsveti, Jan and Joachim - I very much lived of the standard processes that you developed - one more thing I didn't need to take care of and which really helped me focus on my work.

Thank you Carsten for the degradation of the amorphous silicon solar cells and making sure the sun simulator was always working properly. That's one of the reasons the results are as consistent. Thank you Joseph and Oliver for the numerous PDS measurements. We didn't find the correlation between the material properties and the degradation behavior of a-Si:H but I guess the results obtained by Florian make up for that.

There are many more people who helped in terms of preparation and processing at the different stages of the solar cell manufacturing - thanks everyone for making sure there is something to show off.

During the three years at IEK5 there was always a lot of work to do but I always enjoyed it. Sorry guys that I couldn't stay on for much longer, it really was a great time.

After all I would like to thank my family and friends back home for never giving me a hard time when I wasn't around. You know it wasn't an easy choice and I guess my weekend schedule from back then is proof of that.

Last but not least I have to thank two people who had a big influence on my decision to follow this path. I'm very grateful to Dave Fork and Steve Horne for igniting my interest in solar cell technologies and showing me that engineering is what I'm meant for. I can't thank you enough and I hope one of us will succeed in making a difference.

List of Publications

Publications associated with this study

T. Zimmermann, A. J. Flikweert, T. Merdzhanova, J. Woerdenweber, A. Gordijn, U. Rau, F. Stahr, K. Dybek and J. W. Bartha. *Deposition of intrinsic hydrogenated amorphous silicon for thin-film solar cells – a comparative study for layers grown statically by RF-PECVD and dynamically by VHF-PECVD.* Progress in Photovoltaics: Research and Applications, published online July 31st, 2012. **DOI: 10.1002/pip2254.**

A. J. Flikweert, T. Zimmermann, T. Merdzhanova, D. Weigand, W. Appenzeller and A. Gordijn. *Microcrystalline thin-film solar cell deposition on moving substrates using a linear VHF-PECVD reactor and a cross-flow geometry.* Journal of Physics D – Applied Physics 45(1), 015101 (2012). **DOI: 10.1088/0022-3727/45/1/015101.**

T. Zimmermann, A. J. Flikweert, T. Merdzhanova, J. Woerdenweber, A. Gordijn, K. Dybek, F. Stahr and J. W. Bartha. *High rate deposition of intrinsic a-Si:H and μc-Si:H layers for thin-film silicon solar cells using a dynamic deposition process.* MRS Proceedings, 1426, pp. 27–32. **DOI: 10.1557/opl.2012.833.**

A. J. Flikweert, T. Zimmermann, D. Weigand, W. Appenzeller, C. Strobel, B. Leszczynska, M. Albert, K. Dybek, J. Palme, K. Schade, J. Hartung, O. Steinke, F. Stahr, W. Beyer and A. Gordijn. *High-Rate Dynamic VHF Plasma Deposition of a-Si:H and μc-Si:H Thin-Film Solar Cells.* In Proceedings of the 26th European Photovoltaic Solar Energy Conference, pp. 2577–2579 (2011). **DOI: 10.4229/26thEUPVSEC2011-3AV.1.45.**

T. Zimmermann, C. Strobel, M. Albert, W. Beyer, A. Gordijn, A. J. Flikweert, J. Kuske and J. W. Bartha. *Inline deposition of microcrystalline silicon solar cells using a linear plasma source.* Physica Status Solidi C – Current Topics in Solid State Physics 7(3–4), pp. 1097–1100 (2010). **DOI: 10.1002/pssc.200982684.**

T. Zimmermann, A. J. Flikweert, D. Weigand, W. Appenzeller, W. Beyer, A. Gordijn, C. Strobel, M. Albert, K. Dybek, J. Palme, K. Schade, J. Hartung, O. Steinke and F. Stahr. *Inline dynamic deposition of a-Si:H and μc-Si:H thin-film solar cells.* In Proceedings of the 25th European Photovoltaic Solar Energy Conference / 5th World Conference on Photovoltaic Energy Conversion, pp. 2983–2986 (2010). **DOI: 10.4229/25thEUPVSEC2010-3AV.1.36.**

Other publications

F. Köhler, T. Zimmermann, S. Muthmann, A. Gordijn and R. Carius. *Structural order and Staebler-Wronski effect in hydrogenated amorphous silicon films and solar cells.* Submitted to the 39th IEEE PVSC, June 16–21 2013, Tampa (FL).

G. Jost, T. Merdzhanova, T. Zimmermann and J. Huepkes. *Process monitoring of texture-etched high-rate ZnO:Al front contacts for silicon thin-film solar cells.* Thin Solid Films (2012), available online since December 22nd, 2012. **http://dx.doi.org/10.1016/j.tsf.2012.11.147.**

T. Merdzhanova, J. Woerdenweber, T. Zimmermann, U. Zastrow, A. J. Flikweert, H. Stiebig, W. Beyer and A. Gordijn. *Single-chamber process for a-Si:H solar cell deposition.* Solar Energy Materials and Solar Cells 98, pp. 146–153 (2012). **DOI: 10.1016/j.solmat.2011.10.022.**

J. Woerdenweber. T. Merdzhanova, A. J. Flikweert, T. Zimmermann, U. Zastrow, L. Niessen, W. Reetz, H. Stiebig, W. Beyer and A. Gordijn. *Single-Chamber Process for Deposition of Thin-Film Silicon Solar Cells without Plasma Treatment.* In Proceedings of the 25th European Photovoltaic Solar Energy Conference / 5th World Conference on Photovoltaic Energy Conversion, pp. 2978–2982 (2010). **DOI: 10.4229/25thEUPVSEC2010-3AV.1.35.**

C. Strobel, T. Zimmermann, M. Albert, J. W. Bartha and J. Kuske. *Productivity potential of an inline deposition system for amorphous and microcrystalline silicon solar cells.* Solar Energy Materials and Solar Cells 93(9), pp. 1598–1607 (2009). **DOI: 10.1016/j.solmat.2009.04.023.**

C. Strobel, T. Zimmermann, M. Albert, J. Bartha, W. Beyer and J. Kuske. *Dynamic High-Rate-Deposition of Silicon Thin Film Layers for Photovoltaic Devices.* In Proceedings of the 23rd European Photovoltaic Solar Energy Conference, pp. 2497–2504 (2008). **DOI: 10.4229/23rdEUPVSEC2008-3AV.2.54.**

Curriculum Vitae

Name:	Thomas Zimmermann
Date and place of birth:	08.01.1982, Jena (Germany)

Since 11/2012	**Development engineer** at BATOP GmbH, Jena
05/2012–10/2012	**Research fellow** at IEK5 of Forschungszentrum Jülich working on the European Fast Track project
10/2009–04/2012	**PhD thesis** at IEK5 of Forschungszentrum Jülich entitled: "High-rate growth of hydrogenated amorphous and microcrystalline silicon for thin-film silicon solar cells using dynamic very-high frequency plasma-enhanced chemical vapor deposition"
03/2008–09/2009	**Research assistant** at IHM of TU Dresden working on dynamic plasma deposition processes for thin-film silicon
01/2007–09/2007	**Diploma thesis** at IHM of TU Dresden entitled: "Development of amorphous and microcrystalline silicon thin-film solar cells using a dynamic VHF-PECVD system"
10/2001–09/2007	**Studies of Electrical Engineering** at TU Dresden Major: Microelectronics
10/2005–03/2006	**Internship** at Palo Alto Research Center working on: High aspect ratio gridline printing for crystalline silicon solar cells and thermal simulations for high concentration photovoltaics (in collaboration with SolFocus)

Band / Volume 170
Ion Beam Treatment of Functional Layers in Thin-Film Silicon Solar Cells
W. Zhang (2013), xi, 191 pp
ISBN: 978-3-89336-864-8

Band / Volume 171
Pulvermetallurgische Herstellung von porösem Titan und von NiTi-Legierungen für biomedizinische Anwendungen
M. Bram (2013), X, 238 pp
ISBN: 978-3-89336-866-2

Band / Volume 172
IEK-3 Report 2013. Langlebige Elektrochemische Verfahrenstechnik
(2013), ca. 185 pp
ISBN: 978-3-89336-868-6

Band / Volume 173
Combined Steady State and High Cycle Transient Heat Load Simulation with the Electron Beam Facility JUDITH 2
Th. Loewenhoff (2013), XVI, 108 pp
ISBN: 978-3-89336-869-3

Band / Volume 174
High-Quality Thorium TRISO Fuel Performance in HTGRs
K. Verfondern, H. Nabielek, M.J. Kania, H.-J. Allelein (2013), viii, 109 pp
ISBN: 978-3-89336-873-0

Band / Volume 175
Characterization of effective hydraulic properties of unsaturated porous media using spectral induced polarization (SIP)
K. Breede (2013), xiv, 72 pp
ISBN: 978-3-89336-875-4

Band / Volume 176
Zur Mikrostruktur siliziumbasierter Dünnschichten für die Photovoltaik
F. Köhler (2013), i, 100 pp
ISBN: 978-3-89336-876-1

Band / Volume 177
Grundlagen für die Transformation von Energiesystemen
Texte und Ergebnisse der Cadenabbia-Tagung 2012
der Konrad-Adenauer-Stiftung und des Forschungszentrum Jülich GmbH
L. Gruber, J.-F. Hake (Eds.) (2013), VI, 114 pp
ISBN: 978-3-89336-877-8

Band / Volume 178
Thermo - mechanical investigations and predictions for oxygen transport membrane materials
G. Pećanac (2013), 143 pp
ISBN: 978-3-89336-878-5

Band / Volume 179
Thermomechanische Charakterisierung neu entwickelter Feuerfestwerkstoffe
E. Skiera (2013), III, 133 pp
ISBN: 978-3-89336-885-3

Band / Volume 180
Entwicklung und Herstellung von metallgestützten Festelektrolyt-Brennstoffzellen mit Hilfe des Hohlkathoden-Gasflusssputterns
M. Haydn (2013), XVI, 174 pp
ISBN: 978-3-89336-886-0

Band / Volume 181
Characterization and stability investigation of water dispersible colloids (WDCs) in natural soils
C. Jiang (2013), X, 102 pp
ISBN: 978-3-89336-887-7

Band / Volume 182
Monazite-type Ceramics for Conditioning of Minor Actinides: Structural Characterization and Properties
C. Babelot (2013), x, 127 pp
ISBN: 978-3-89336-889-1

Band / Volume 183
High-rate growth of hydrogenated amorphous and microcrystalline silicon for thin-film silicon solar cells using dynamic very-high frequency plasma-enhanced chemical vapor deposition
T. Zimmermann (2013), x, 126 pp
ISBN: 978-3-89336-892-1

Weitere ***Schriften des Verlags im Forschungszentrum Jülich*** unter
http://wwwzb1.fz-juelich.de/verlagextern1/index.asp

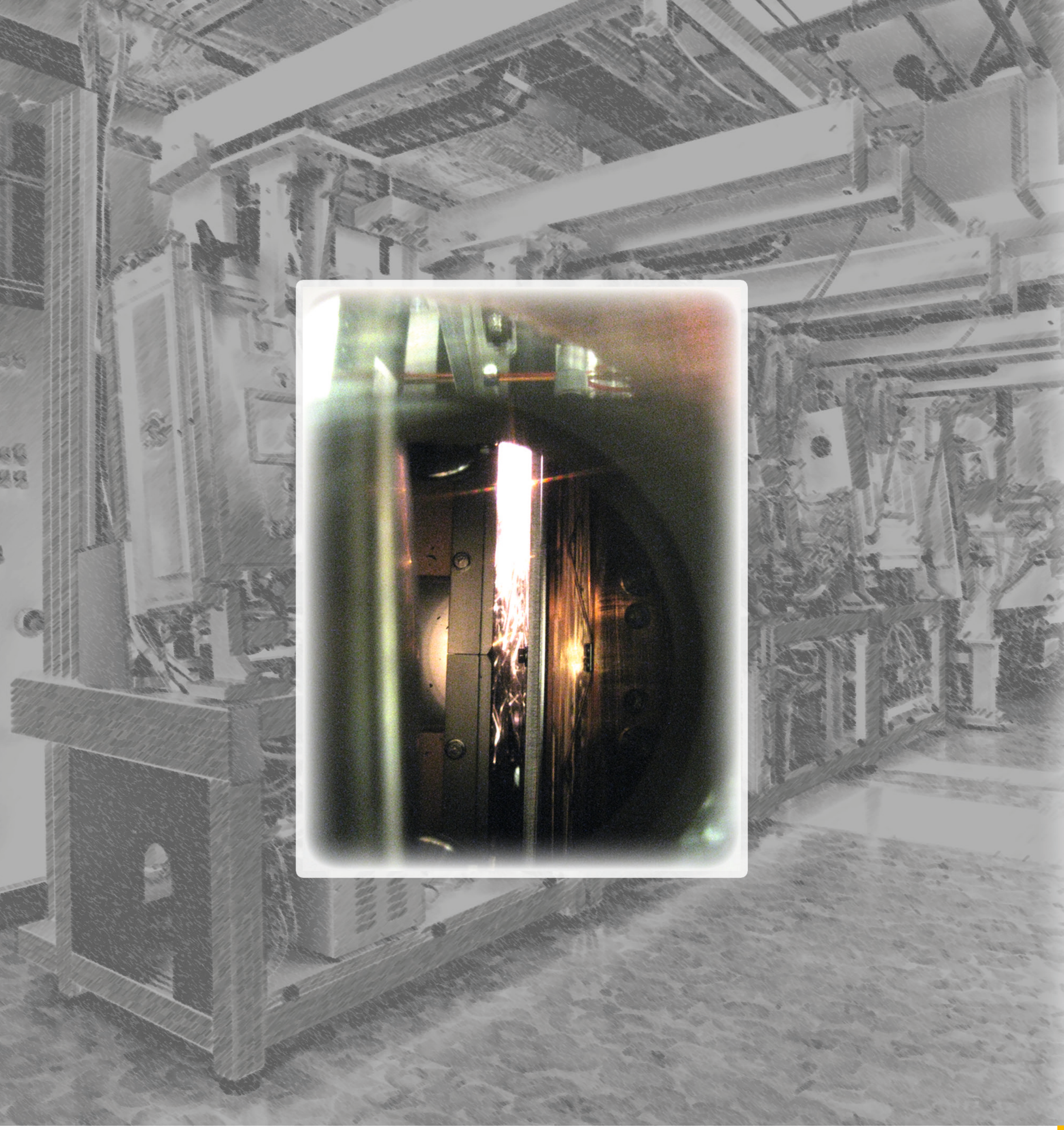

Energie & Umwelt / Energy & Environment
Band / Volume 183
ISBN 978-3-89336-892-1